Studies on Beam Dynamics in Single and Coupled Parity-Time Symmetric Systems with Kerr and Nonlocal Nonlinearity

Thesis submitted to the University of Calicut
in partial fulfillment of the requirements
for the award of the degree of

Doctor of Philosophy
in
Physics

T. P. Suneera

Department of Physics
University of Calicut
P. O. Calicut University, PIN-673 635
Malappuram Dt., Kerala.

June 2018

CERTIFICATE

Certified that the work presented in this thesis entitled 'Studies on Beam Dynamics in Single and Coupled Parity-Time Symmetric Systems with Kerr and Nonlocal nonlinearity' is a bona fide work done by Mrs. T. P. Suneera under my guidance in the Department of Physics, University of Calicut and that this work has not been included in any other thesis submitted previously for the award of any degree.

Farook College
June 2018

Dr. P. A. Subha
(Supervising Guide)

DECLARATION

I hereby declare that the work presented in this thesis entitled 'Studies on Beam Dynamics in Single and Coupled Parity-Time Symmetric Systems with Kerr and Nonlocal nonlinearity' is based on the original work done by me under the guidance of Dr. P. A. Subha, Department of Physics, Farook College, University of Calicut, and has not been included in any other thesis submitted previously for the award of any degree.

University of Calicut

June 2018 T. P. Suneera

Acknowledgements

I would like to take this opportunity to express my gratitude to several people who helped me to accomplish my lifelong dream, this thesis.

I was introduced to the interesting world of solitons by none other than Dr. P. A. Subha, Department of Physics, Farook college, University of Calicut, whose extensive knowledge and expertise in the subject guided me through this research work. I feel honoured to have worked under her, who is really a mentor for me. Her understanding, guidance, encouragement and personal involvement have helped me a lot to overcome all the hurdles during this period.

I express my sincere gratitude to Prof. P. P. Pradyumnan, Head of the Department of Physics and Prof. M. M. Musthafa, former Head of the Department of Physics, University of Calicut for providing me all the support and essential facilities to carry out the research. I am deeply indebted to Dr. Mohamed Shahin T., who is my co-guide for his kindness and encouragements. I also thank all the faculty members, library and office staff of the department for the help they rendered during the entire course of my research study.

Its my pleasure to acknowledge Dr. E. P. Imbichikoya, the former principal and Dr. K. M. Naseer, the Principal, Farook college for their support to complete my research work. Prof. K. K. Abdullah, the former HOD, Physics department deserves special mentioning for his interests in my research study and suggestions to improve the thesis. I am indebted to all the faculties of Department of Physics, Farook college for their encouragement. I owe greatly to staff in the informatic

center for providing the technical support.

I express my sincere gratitude to Prof. P. Ramakrishnan and Prof. K. Suresh Babu who were in the department of Physics at Government college Madappally during the first stage of my career, for their motivation and interest in my research. Prof. M. Chithralekha, Principal, Prof. P. Ramakrishnan, former Principal, and Prof. E. M. Abdul Jamal, former Principal, Government college, Koyilandi deserve special mention for granting permission to undergo the course under the Faculty Development Programme. I would also like to thank my colleagues in the Department of Physics, Government College, Madappally for their keen interest and encouragement in my research work. I express my gratitude to Dr. G. Harikrishnan, Dr. Nithyaja B. and Mr. M. Hameed for always being there whenever I needed them. I am grateful to Dr. R. K. Sunilkumar and his research scholar Bibeesh for their technical support whenever it was inevitable.

I would like to put on record my special thanks to the UGC, New Delhi, and to the Government of Kerala for granting teacher fellowship and sanctioning deputation without which this work would have been impossible.

I am really thankful to my friend Dr. C. P. Jisha, Post-Doctoral Researcher, UPorto, Portugal, for her valuable suggestions and fruitful discussions. I really enjoyed the company of my fellow researchers Usha K., Musammil N. M., Sreepriya M.K, K. Aysha Muhsina, Remi, and Dr. Sudha Shankar and I express my gratitude for their encouragement and the fruitful discussions. I fondly remember the moments spent with all other research scholars especially Vidya Rajan, Ahammed Rasin Nanakkal, Deepthy Maria Christy, Vishnu Venugopal, Anju, Sravan S, Jamshihas and Shabeer.

I am deeply indebted to Umma, Bappa, Pappa, and Mammy who supported and encouraged me at every moment of my personal and academic life and longed to witness my success. The teachers who taught me at various stages of educa-

tion, deserve special thanks without whom my world would have been in complete darkness. I also express my gratitude to my Ponnus, Thukku and Thechu who managed my absence and for being with me, always. My brothers always had a helping hand in my success and I express special thanks to them. My house-made, deserves special mentioning for her commitment to take care of my kids and doing all house-hold activities during this period.

Above all, I thank almighty who made me what I am and for providing all suitable circumstances for this achievement.

T. P. Suneera

Contents

List of Figures

List of papers published/communicated:

1. T. P. Suneera, P. A. Subha, Single-hump and double-hump solitons in a PT-symmetric complex potential. Waves in Random and Complex Media 2016, 27, 2, 241-254.

2. T.P. Suneera, P.A. Subha, Higher eigenmodes of matter wave solitons in parity-time symmetric complex potential. Perspectives in Science 2016, 8, 482484.

3. T. P. Suneera, P. A. Subha, Higher eigenmodes of nonlocal gap solitons in parity-time symmetric complex potential with a defocusing nonlinearity. Chaos, Solitons, and Fractals 2017, 98, 183-188.

4. T. P. Suneera, P. A. Subha, Parity-time symmetric coupler in transverse periodic and aperiodic potentials. The European Physical Journal Plus 2018, 133, 84.

5. T. P. Suneera, P. A. Subha, Nonlocal gap solitons in parity-time symmetric coupler with transverse real potential. Journal of Optics 2018, 20, 095504.

6. T. P. Suneera, P. A. Subha, Switching dynamics in parity-time symmetric coupler with nonlocal nonlinearity having transverse potentials. (Communicated to Journal of modern optics.)

List of papers presented:

1. Propagation of matter waves in parity-time symmetric synthetic materials, National Conference on modern optics and material science (NCMOMS-2015), Farook College, University of Calicut.

2. Higher eigenmodes of matter wave solitons in parity-time symmetric complex potential, International Conference on Engineering and Material Science (ICEMS-2015), Jaipur, Rajasthan.

3. Optical solitons in aperiodic PT-symmetric complex potential with nonlocal nolinearity, International conference on Nonlinear Physics: Theory and Experiment (NPTE-2016), Farook College, University of Calicut.

4. The stationary states of a nonlinear coupler in a PT symmetric periodic potential, Conference on Nonlinear Systems and Dynamics (CNSD-2016), IISER, Kolkatta.

1.5

Preface

Solitons are localized waves which can propagate through nonlinear media without change of its shape and remain unaffected even after collisions with each other. Mathematically, the word 'soliton' refers to the solutions of the integrable nonlinear partial differential equations. In real physical systems, the nonlinear partial differential equations are non-integrable, but support the self-trapped solutions or the solitary wave solutions. Hence in modern literature, this distinction is no longer used and all self-trapped beams are called as solitons. Solitons have been investigated in various fields such as nonlinear optics, plasmonics, fluid dynamics, Bose-Einstein Condensates, condensed matter physics and astrophysics. Especially, the solitons in optical systems have been studied extensively due to the advent of high intensity lasers and the optical fiber communication system. The worldwide demand for ultra-fast data transmission and more bandwidth promote further research in optical solitons.

Optical solitons are electromagnetic waves that are confined in space or time or both. A pulse/beam spreads as it propagates due to dispersion/diffraction. If the nonlinearity balances the dispersion, temporal solitons are formed and if the nonlinearity counter acts with the diffraction, spatial solitons are obtained. Spatio-temporal solitons or light bullets are obtained, if both the diffraction and dispersion compensate with the nonlinearity.

The propagation of high intense beam modifies the optical properties of the medium due to the contribution of higher order susceptibilities. Third order susceptibility is the source of quadratic electro-optic effect or Kerr effect. This leads to the variation of refractive index with beam intensity. In Kerr effect,

the refractive index depends on the intensity of the beam at the very point (i.e., local nonlinearity). Very often the transport phenomena or interactions in the system result in variation of the refractive index due to the beam intensity at the vicinity of a point. This behaviour is called nonlocal nonlinearity.

Non-Hermitian operators which respect parity-time symmetry ($\mathcal{PT}$), possess real eigenvalues for a set of system parameters. A Hamiltonian with complex potential $V(x)$ is $\mathcal{PT}$ symmetric, if $V(x) = V^*(-x)$ or the real part of the potential is an even function of position and the imaginary part is odd. The complex potential plays the role of refractive index or the dielectric permittivity. This leads to the application of $\mathcal{PT}$ symmetry to diverse fields such as nonlinear optics, Bose-Einstein condensates, metamaterials and photonics. The $\mathcal{PT}$ symmetric optical systems exhibit novel features like loss-induced transparency, unidirectional invisibility, selective mode lasing and coherent perfect laser absorption.

The thesis presents a theoretical study of beam dynamics in single and coupled $\mathcal{PT}$ symmetric systems with Kerr and nonlocal nonlinearity. We have studied the higher eigenmodes of $\mathcal{PT}$ symmetric single systems with Kerr and nonlocal nonlinearity. The studies have been extended to $\mathcal{PT}$ symmetric coupled systems which find applications in all-optical switching. We have studied the switching dynamics of the coupler with Kerr and nonlocal nonlinearity. Variational method has been employed for the semi-analytic analysis and finite difference beam propagation method for the direct simulation. The steady-state equations have been solved using Newton's Conjugate Gradient method and pseudo-spectral methods.

The structure of the thesis is as follows. The first chapter describes a basic introduction to solitons, optical solitons, kerr and nonlocal nonlinearities, $\mathcal{PT}$ symmetric systems and methodology.

Chapter 2 deals with the single-hump and double-hump solitons in a system with $\mathcal{PT}$ symmetric complex potential having Kerr nonlinearity. The $\mathcal{PT}$ symmetric counter part of the parabolic potential has been chosen for analysis. The $\mathcal{PT}$ symmetric phase transition point has been studied by varying the strength

of real part of the potential and the coefficient of the nonlinearity. We have analyzed the stability of the solitons using Bogoliubov - De - Genes equations.

In chapter 3, the higher eigenmodes of the gap solitons in a $\mathcal{PT}$ symmetric periodic potential with a defocusing nonlocal nonlinearity have been described. The double-hump nonlocal gap solitons exist above a threshold value of energy and spread through two neighboring channels in the $\mathcal{PT}$ symmetric region. The power carried by the imaginary component of the double-hump soliton increases with the imaginary part of the complex potential. The total power is invariant with respect to the strength of the imaginary part of the potential and the range of the nonlocality. The double-hump solitons are unstable and the perturbation modes vary exponentially.

Chapter 4 describes the $\mathcal{PT}$ symmetric coupler in transverse real periodic and aperiodic potentials with Kerr nonlinearity for linear and nonlinear regime. The propagation-invariant solutions of the system have been studied and found that the high frequency solitons reside in the minimum value of the periodic and aperiodic potentials.

Beam dynamics in the $\mathcal{PT}$ symmetric coupler with transverse real periodic potential having defocusing nonlocal nonlinearity has been studied in chapter 5. The high-frequency and the low-frequency modes with single-hump, double-hump and triple-hump structures are obtained. The linear stability analysis of the high-frequency and low-frequency modes predict that both modes are stable for weak nonlocality but unstable with oscillatory instability for strong nonlocality.

Chapter 6 deals with the switching dynamics in $\mathcal{PT}$ symmetric coupler with transverse real potentials. Both periodic and aperiodic potentials are analysed with Kerr and nonlocal nonlinearity. The switching from channel with gain to channel with loss is possible for high input power by varying either the range of the nonlocality or the strength of the transverse periodic potential.

Chapter 7 summarizes the findings of the thesis and describes future prospectives of this work.

SUNEERA T. P. “STUDIES ON BEAM DYNAMICS IN SINGLE AND COUPLED PARITY-TIME SYMMETRIC SYSTEMS WITH KERR AND NONLOCAL NONLINEARITY”. THESIS. DEPARTMENT OF PHYSICS, UNIVERSITY OF CALICUT, 2018.

Chapter 1

Basic Concepts and Thesis Outline

1.1 Introduction

Solitons are localized waves which can propagate through nonlinear media without change of its shape and remain unaffected even after collisions with each other [1]. Mathematically, the word 'soliton' refers to the solutions of the integrable nonlinear partial differential equations. In general, the nonlinear models are non-integrable but support self-trapped solutions known as solitary waves.

The discovery of the soliton was quite accidental and it was reported by J.S.Russel, a naval architect, in 1834. He observed a rounded, smooth and well-defined heap of water moving with great velocity through a narrow canal preserving its shape for kilometers. He called it as a 'wave of translation'. Two Dutch physicists, Korteweg and de Vries developed a theory for the wave of translation and the dynamics is modeled by Kortweg de Vries equation (KdV). Later Zabusky and Kruskal numerically studied KdV equation. They found the solitary wave solutions with particle nature and termed it as 'solitons'. Solitons find applications in many fields such as nonlinear optics [2, 3, 4], Bose-Einstein Condensates [5], and hydrodynamics [6].

Optical solitons are electromagnetic waves that are confined in space or time or both. The advent of lasers and the optical fibers revolutionized the communication industry. The world is in need of ultra-fast as well as high bandwidth communication system. Optical solitons find potential applications in optical communication systems, all-optical switching, and optical computing where they act as information carrying bits.

1.2 Optical solitons

The propagation of electromagnetic pulse or beam though a medium leads to the broadening due to chromatic dispersion or diffraction. These phenomena adversely affect the technological applications of light. The information carrying capacity get reduced due to the broadening of the pulse. However the nonlinearity of the medium counteracts in the case of high intense pulse/beam and exactly balances the broadening. These self-trapped light beams are called optical solitons. There are temporal and spatial optical solitons depending on the confinement either in time or in space.

1.2.1 Linear effects

When an electromagnetic pulse or beam propagates through a medium, it broadens due to dispersion or diffraction. In the case of low intensity beam, these are the effects even in nonlinear media.

Dispersion

When the speed of a wave depends only on the physical properties of the medium, it is independent of the frequency. The wave travels through the medium maintaining its shape and the medium is called non-dispersive.

In dispersive media, the wave speed varies with the frequency of the wave due to various reasons. In the case of electromagnetic wave, this is due to the absorption of characteristic resonance frequencies by the bound electrons of the

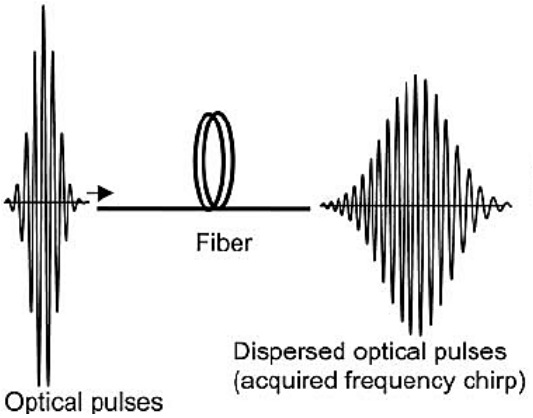

(a)

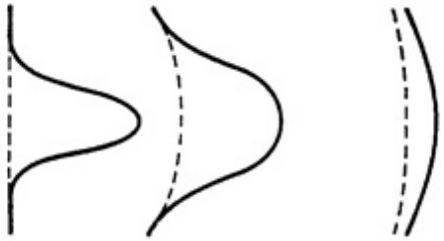

(b)

Figure 1.1: The broadening of a Gaussian input pulse as it propagates. (a) Dispersion [7] and (b) diffraction [8].

media. This causes distortion of the wave as it propagates. A wavepacket has many Fourier components. Each component propagates with different speed and the wavepacket distorts. This is known as dispersion. When the high frequency components of the wavepacket move slower than the low frequency components, it is called the normal dispersion. The high frequency components travel faster than the low frequency components in the anomalous dispersion regime. Hence the pulse disperses and is known as group velocity dispersion (GVD). The dispersion of the Gaussian pulse as it propagates through an optical fiber is shown in Figure 1.1(a) [7].

Diffraction

When a light beam encounters an obstacle/aperture, the beam bends around it. This is known as diffraction. When the size of the obstacle is comparable

with the wavelength of the beam, the diffraction effects are more pronounced. A beam which propagates through a medium with varying refractive index, also exhibit diffraction effects. A collimated light beam with the diameter d and the wavelength λ, spreads through an angle λ/d due to diffraction. Figure 1.1(b) shows the diffraction broadening of the pulse [8].

1.2.2 Kerr nonlinearity

When an optical pulse passes through a dielectric medium, the anharmonic motion of bound electrons produce nonlinear response [2]. The induced polarisation $\mathbf{P}$ in the medium is related with the electric field $\mathbf{E}$ as given below:

$$\mathbf{P} = \epsilon_{\mathbf{0}}(\chi^{(\mathbf{1})}.\mathbf{E} + \chi^{(\mathbf{2})} : \mathbf{EE} : + \chi^{(\mathbf{3})} : \mathbf{EEE} : + ..., \tag{1.1}$$

where ϵ_0 is the permittivity of vacuum, $\chi^{(1)}$ is the linear part of the susceptibility and $\chi^{(2)}$, $\chi^{(3)}, ...$ are the nonlinear parts of the susceptibilities of second, third and higher orders. In general, $\chi^{(j)}$ is a tensor of rank $j+1$ where $j = 1, 2, ...$ The nonlinear effects due to each $\chi^{(j)}$ are different. Only the first order susceptibility $\chi^{(1)}$ contributes for low intense beam which is linear. As the intensity increases, higher order susceptibility plays major role leading to nonlinear behaviour. Second order susceptibility $\chi^{(2)}$ vanishes for molecules with center of symmetry like silica.

The nonlinear effects due to third order susceptibility $\chi^{(3)}$ are important for centrosymmetric and non-centrosymmetric molecules. It is responsible for different nonlinear phenomena such as intensity-dependent refractive index, third harmonic generation and four-wave mixing. The intensity-dependent refractive index is also known as quadratic electro-optic effect or Kerr effect. The refractive index obeys the relation:

$$n(I) = n_0 + n_2 I, \tag{1.2}$$

n_0 and n_2 being the linear and nonlinear terms respectively. In Kerr effect, the

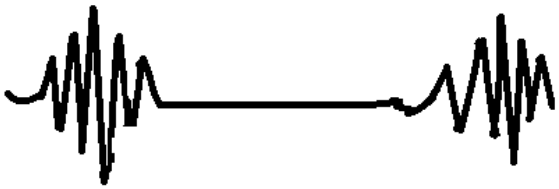

(a)

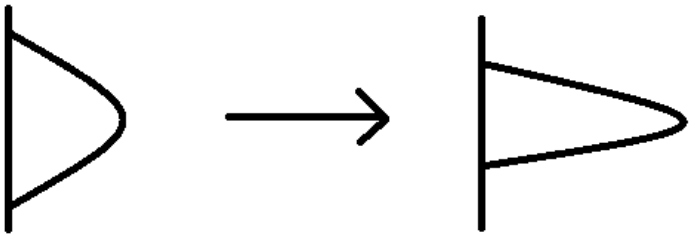

(b)

Figure 1.2: (a) The self phase modulation (SPM) of a wave packet and (b) the self focusing of a pulse.

refractive index depends on the intensity of the beam at the very point (i.e., local nonlinearity). The nonlinear refractive index is responsible for several effects in the wave propagation which includes the self phase modulation (SPM) and the self-focusing.

Self phase modulation (SPM)

When an optical pulse propagates through a fiber, high intense portions have high refractive index whereas low intense portions have low refractive index. A refractive index gradient develops within a single pulse of light such that positive gradient for leading edge while negative gradient for trailing edge. The variation in refractive index causes variation in phase change and thereby produces frequency-chirping [9, 10]. This phenomenon is known as Self Phase Modulation. The frequency spectrum of the pulse broadens due to SPM. The SPM of a wave packet is shown in Figure 1.2(a).

Self-focusing

When a beam with high intensity propagates through a medium, a transverse refractive index gradient develops in the medium. This acts like a focusing lens for the beam. The refractive index is large at the regions where the beam intensity high, generally at the center of the beam. This causes focusing of the beam and the beam shrinks. As the beam shrinks, the refractive index gradient across the transverse profile increases further. The peak intensity region in the medium keeps increasing until any other effect (i.e, de-focusing) interrupt the process. Kerr-induced self-focusing was first predicted by Kelley [11]. The self focusing of a beam is depicted in Figure 1.2(b).

1.3 Nonlinear Schrödinger Equation (NLSE) for optical field

An electromagnetic wave propagating through a nonlinear medium obeys Maxwell's equation:

$$\nabla^2 E - \frac{1}{c^2}\frac{\partial^2 E}{\partial t^2} = \frac{1}{\epsilon_0 c^2}\frac{\partial^2 P}{\partial t^2}, \tag{1.3}$$

where E is the electric field, c is the speed of light in free space, and ϵ_0 is the dielectric permittivity of the free space. The induced polarisation P includes linear and nonlinear contributions:

$$\begin{aligned} &P(r,t) = P_L(r,t) + P_{NL}(r,t), \qquad (1.4)\\ &P_L(r,t) = \epsilon_0 \int \chi^{(1)}(t-t')E(r,t')dt',\\ &P_{NL}(r,t) = \epsilon_0 \int\int\int \chi^{(3)}(t-t_1)(t-t_2)(t-t_3)E(r,t_1)E(r,t_2)E(r,t_3)dt_1dt_2dt_3. \end{aligned}$$

Here $\chi^(1)$ and $\chi^(3)$ are the susceptibility tensors of order 1 and 3 respectively.

The time-dependent nature of the envelop of the pulse is written as:

$$E(r,t) = A(Z,t)F(x,y)e^{i\beta_0 Z}, \tag{1.5}$$

in which β_0 is the propagation constant and $F(x,y)$ is the transverse field distribution of the fundamental mode in a single-mode fiber. $A(Z,t)$ is the time-dependent amplitude which implies that each spectral component of the pulse moves with different speed inside the fiber owing to the chromatic dispersion. Hence the refractive index varies with the frequency ω which is expressed as:

$$\tilde{n} = n(\omega) + n_2|E|^2. \tag{1.6}$$

The analysis is carried out in Fourier domain to incorporate the chromatic dispersion. The nonlinearity is treated as a perturbation. The Fourier transform of $A(Z,t)$ is represented by $\tilde{A}(Z,t)$ which obeys the equation:

$$\frac{\partial \tilde{A}(Z,t)}{\partial Z} = i[\beta(\omega) + \Delta\beta - \beta_0]\tilde{A}(Z,t). \tag{1.7}$$

Here $\beta(\omega) = k_0 n(\omega)$. The nonlinear part $\Delta\beta$ satisfies the relation:

$$\Delta\beta = k_0 n_2 |A|^2 \frac{\int_{-\infty}^{\infty}\int_{-\infty}^{\infty}|F(x,y)|^4 dxdy}{\int_{-\infty}^{\infty}\int_{-\infty}^{\infty}|F(x,y)|^2 dxdy}. \tag{1.8}$$

The Taylor expansion of $\beta(\omega)$ around ω_0 is written as:

$$\beta(\omega) = \beta_0 + (\omega - \omega_0)\beta_1 + (\omega - \omega_0)^2\beta_2 + ..., \tag{1.9}$$

where $\beta_j = \frac{d^j\beta}{d\omega^j}$. Taking inverse Fourier transform of equation 1.7 after substituting for $\beta(\omega)$, $A(Z,t)$ is obtained as:

$$\frac{\partial A}{\partial Z} + \beta_1\frac{\partial A}{\partial t} + i\beta_2\frac{\partial^2 A}{\partial t^2} = i\gamma|A|^2 A, \tag{1.10}$$

where $(\omega - \omega_0) \simeq \frac{\partial}{\partial t}$ in inverse Fourier transform, β_1 and β_2 are the first order

dispersion effect $\frac{1}{v_g}$ and the group velocity dispersion parameter $\frac{d^2\beta}{d\omega^2}$ respectively. The nonlinear parameter γ is given by $\frac{n_2\omega}{cA_{eff}}$, n_2 being the intensity dependent refractive index with the effective mode area $A_{eff} = \frac{k_0 n_2 |A|^2}{\Delta\beta}$.

Transforming equation 1.10 by introducing new cocordinates to a reference frame moving with the pulse such that $\tau = \frac{(t-\frac{z}{v_g})}{T_0}$, $z = \frac{Z}{L_D}$, and $u = \sqrt{\gamma L_D A}$, the NLS equation for the optical field is obtained as:

$$i\frac{\partial u}{\partial z} + \frac{\beta_2}{2}\frac{\partial^2 u}{\partial t^2} + \beta|u|^2 u = 0. \tag{1.11}$$

1.3.1 Temporal soliton

As we already seen, an optical pulse has an innate tendency to spread as it propagates due to dispersion. The broadening of the pulse due to dispersion exactly compensates with nonlinearity for high intensity. Then the pulse travels without distortion and it is known as temporal soliton. If SPM balances the GVD, the temporal solitons are formed [3, 4]. The dynamics of these solitons are modeled by the Nonlinear Schrödinger Equation (NLSE):

$$i\frac{\partial \Psi}{\partial z} + \frac{\beta_2}{2}\frac{\partial^2 \Psi}{\partial t^2} + \beta|\Psi|^2\Psi = 0, \tag{1.12}$$

where Ψ denotes the temporal soliton. The sign of GVD parameter β_2 is positive and negative for bright and dark temporal solitons respectively. The dispersion and the nonlinearity exactly balance in the anomalous dispersion regime (i.e., $\beta_2 = +1$) thereby producing temporal solitons. The nonlinear coefficient $\beta = 1$ for self-focusing nonlinearity and $\beta = -1$ for self-defocusing nonlinearity.

1.3.2 Spatial soliton

The propagation of high intense light through nonlinear media result in the diffraction and the self-focusing of the beam. The exact balance between the self-focusing and the diffraction lead to the propagation of beam with constant diameter. This is called the self-trapping of light or spatial soliton.

Diffraction along one of the transverse directions is considered as similar to the anomalous dispersion in temporal solitons. The dynamics of spatial solitons is governed by the NLSE which is given by:

$$i\frac{\partial \Psi}{\partial z} + \frac{\beta_2}{2}\frac{\partial^2 \Psi}{\partial x^2} + \beta|\Psi|^2\Psi = 0, \tag{1.13}$$

where the second derivative is taken with respect to the transverse coordinate to incorporate the diffraction.

1.4 Nonlinearities

The propagation of high intense beam/pulse modifies the optical properties of the medium. There are different underlying mechanisms for the modification of optical properties, depending on the nature of materials/media. Certain nonlinear models which are used to explain these systems, are given below.

1.4.1 Competing nonlinearity

The nonlinear effects of the medium depends on the higher order susceptibility (more than third order) if the beam intensity is too large [12]. Certain materials like PTS, AlGaAs, and CdS exhibit these behaviour. In this case the nonlinearity, n_{nl} is expressed by:

$$n_{nl} = n_2 I + n_4 I^2,$$

in which n_2 and n_4 are the coefficients of second and fourth order nonlinearity respectively and both of them have opposite sign.

1.4.2 Saturable nonlinearity

Several systems including two-level atomic systems and photo-refractive materials, have saturable nonlinearity [12]. When a high intense beam propagates

through these media, the nonlinearity get saturated. The nonlinear part of the refractive index is characterised by the maximum refractive index change n_∞ and the saturation intensity I_{sat} as given below:

$$n_{nl}(I) = n_\infty[\ 1 - \frac{1}{(1 + \frac{I}{I_{sat}})^p}]\ ,$$

where p is a constant.

1.4.3 Transitive nonlinearities

In this model, the nonlinearity transits from one form to another as the intensity varies, as in bistable solitons. The intensity at which the nonlinearity change its form is called the critical intensity I_{cr}. A simple model of the system is given by:

$$\begin{aligned} n_{nl}(I) &= n_{21}I, I < I_{cr}, \\ &\quad n_{22}I, I > I_{cr}, \end{aligned}$$

where n_{21} denotes the nonlinear coefficient in the domain $I < I_{cr}$ and n_{22} represents the nonlinear coefficient in the domain $I > I_{cr}$.

1.4.4 Nonlocal nonlinearity

A nonlinear optical effect is called nonlocal if the response induced by the beam at a point on the medium also depends on the electromagnetic field at the vicinity of the point [13]. Very often the transport phenomena or interactions in the system result the variation of the refractive index with the beam intensity at the surrounding points [14]. The extent of this surrounding is known as the degree of nonlocality. Different materials/media exhibit various nonlocal nonlinearities owing to particular physical mechanisms. Atomic diffusion [15], heat diffusion [16], drift of ions [17], and long-range molecular interactions [18] are certain mechanisms which lead to the nonlocal nonlinearity in physical systems.

When a beam with intensity I propagates through a medium, the variation

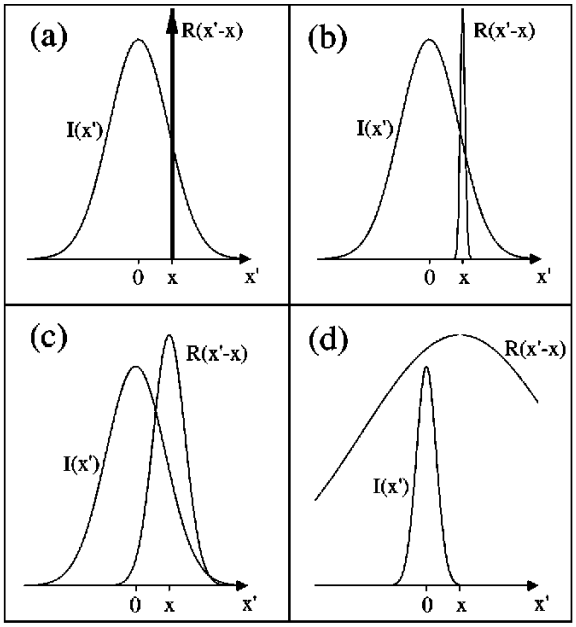

Figure 1.3: Various degrees of nonlocality, as given by the width of the nonlocal response function $R(x)$ and the intensity profile of the beam $I(x)$ [19]. Shown are (a) local, (b) weakly nonlocal,(c) general (nonlocal), and (d) highly nonlocal responses.

in refractive index is modeled by:

$$n(I) = s \int R(\zeta - \mathbf{r}) I(\zeta, z) d\zeta, \tag{1.14}$$

where $\mathbf{r}$ represents the transverse spatial coordinates, $R(\mathbf{r})$ is the response function, $s = 1$ for self-focusing and $s = -1$ for defocusing nonlinearity. The normalisation condition for $R(\mathbf{r})$ is $\int R(\mathbf{r}) d\mathbf{r} = 1$ and $R(\mathbf{r}) = R(r)$ for real localised symmetric response functions. The degree of nonlocality is obtained from the width of the response function.

Figure 1.3 shows various degrees of nonlocality (or the width of the response function) and the intensity of the beam [19, 14]. When the response function is the dirac delta function $R(r) = \delta(r)$, the refractive index change $n(I)$ is a localised function of intensity such that $n(I) = sI$ as depicted in Figure 1.3(a). As the width of $R(\mathbf{r})$ increases, the nonlocal contribution to refractive index change also increases. If the width of the response function is much less than the

width of the beam (Figure 1.3(b)), the intensity can expand as a Taylor series,

$$I(\mathbf{r}) = I_0 + \mathbf{r}.\nabla_\perp I + r^2\nabla_\perp^2 I + ... \tag{1.15}$$

where $\nabla_\perp$ represents the derivative with respect to the transverse coordinates. Substituting the Taylor expansion of I in equation 1.14 and retaining the first significant terms:

$$n(I) = s(I + \gamma\nabla_\perp^2 I), \tag{1.16}$$

where $\gamma = \frac{1}{2D}\int r^2 R(r) d\mathbf{r}$ which is the strength of the nonlocality and $\mathbf{r}$ spans D dimensional coordinate space. This type of nonlinearity appears in the studies of nonlinear effects in plasma [20]. Nonlinear Schrödinger equation with this nonlinearity supports both the bright and the dark solitons [21]. When the width of the response function is much greater than that of the beam, it represents highly nonlocal limit as illustrated in Figure 1.3(d). Then the nonlinearity is expressed as:

$$n(I) = sR(r)P, \tag{1.17}$$

P being the power of the beam. So the propagation equation becomes local and linear. It provides the evolution of a beam having the profile of the response function which trapped inside an effective waveguide. This case was first reported by Snyder and Mitchell [13].

Usually nonlinear response of the medium is nonlocal. However if the width of the beam is very large compared to the width of the response function, the nonlocal behaviour is negligible. Then $\gamma = 0$ and the nonlinearity is Kerr type.

NLSE for different types of nonlinearity can be written by modifying the nonlinear term in equation 1.11 as:

$$i\frac{\partial u}{\partial z} + \frac{\beta_2}{2}\frac{\partial^2 u}{\partial x^2} + F(|u|^2)u = 0, \tag{1.18}$$

in which $F(|u|^2)$ is the nonlinearity functional of refractive index change.

In chapters 3, 5 and 6 we have used nonlocal nonlinearity to study the existence and stability of optical solitons.

1.5 $\mathcal{PT}$ symmetric systems

When the force acting on the system is derivable from a single potential function which depends only on spatial coordinate, the system (force) is said to be conservative [22]. In this case, Hamiltonian represents the total energy which is the sum of the kinetic energy and the potential energy. The state of a system is described in terms of the state vector $\psi(\mathbf{r}, t)$. The dynamics of the state vector $\psi(\mathbf{r}, t)$ is given by the Schrödinger equation:

$$i\hbar\frac{\partial\psi}{\partial t} = H\psi(\mathbf{r}, t), \tag{1.19}$$

where $H = -\frac{\hbar^2}{2m}\nabla^2\psi + V(r)\psi$, Hamiltonian which is Hermitian operator acting on the Hilbert space $L^2(\Re^D)$ with dimension D. The inner product in this space is defined as:

$$\langle\psi, \phi\rangle = \int_{\Re^D} \psi^*(\mathbf{r}, t)\phi(\mathbf{r}, t)d\mathbf{r},$$

in which $*$ denotes complex conjugation. Hermitian conjugation $H^\dagger$ for a linear operator H is defined as $\langle H^\dagger\psi, \phi\rangle = \langle\psi, H\phi\rangle$. Hermitian operators or self-adjoint operators are those which satisfies the relation $H = H^\dagger$. These possess real eigenvalues and the eigenvectors form an orthonormal set. There is a linear Hermitian operator corresponding to every physical observable.

The losses are inevitable in physical systems. When dissipative forces or losses are present in the physical system, the system (force) is called dissipative. The spatial soliton dynamics is modeled by the modified NLSE:

$$i\frac{\partial\phi}{\partial z} + \frac{\partial^2\phi}{\partial x^2} + \frac{\partial^2\phi}{\partial y^2} + F(|u|^2)u - \frac{i}{2}G(z)\phi = 0, \tag{1.20}$$

G being the gain/loss of the system depending on whether $G > 0$ or $G < 0$ respectively.

The $\mathcal{PT}$ symmetric systems pave way to the fruitful utilisation of the losses. A class of the non-Hermitian operators which respect the subsequent action of space inversion (parity operator) and the time reversal, possess real eigenvalues [23]. These are known as $\mathcal{PT}$ symmetric operators. Non-Hermitian Hamiltonian respects the parity-time symmetry if the potential $V(x) = V(-x)^*$ [24]. The $\mathcal{PT}$ symmetric Hamiltonians have real eigenvalues up to a critical value of the gain/loss known as the $\mathcal{PT}$ symmetric phase transition point above which the eigenvalues are complex. The $\mathcal{PT}$ symmetric phase transition point is also known as exceptional point.

Two major discrete symmetries in physics are space inversion and time reversal symmetries. The space inversion operator is also known as parity operator $\mathcal{P}$ which is defined as $\mathcal{P}\psi(r,t) = \psi(-r,t)$ [25]. The time reversal operator is an antilinear operator and is defined as $\mathcal{T}\psi(r,t) = \psi^*(r,-t)$. The antilinear behaviour can be described by the relation $\mathcal{T}(\lambda\psi + \phi) = \lambda^*\mathcal{T}\psi + \mathcal{T}\phi$. $\mathcal{P}^2 = \mathcal{T}^2 = I$, I being the identity operator and $[\mathcal{P}, \mathcal{T}] = 0$. An operator H is $\mathcal{PT}$ symmetric if $[\mathcal{PT}, H] = 0$. $\mathcal{PT}$ symmetry is unbroken if the eigenfunctions of H is simultaneously eigenfunctions of $\mathcal{PT}$. Then $H\psi = E\psi$ implies that $\mathcal{PT}\psi = \lambda\psi$. $\lambda = e^{i\theta}$ represents the pure phase. In the unbroken case, $H\mathcal{PT}\psi = E^*\mathcal{PT}\psi$ is equivalent to $H\psi = E^*\psi$. So the eigenvalues are real. i.e., $\mathcal{PT}$ symmetry is not sufficient for real spectra, but it should be unbroken. Otherwise $\mathcal{PT}$ symmetry is broken and it is associated with the complex eigenvalues.

$\mathcal{PT}$ symmetry does not lead to the completeness of eigenvectors unlike Hermiticity. Though the spectrum is completely real, the eigenvectors do not form complete set due to the presence of exceptional points just like other non-Hermitian operators. The study of $\mathcal{PT}$ symmetric systems are important in various fields such as nonlinear optics, plasma physics, meta-materials, atom lasers and all-optical signal processing.

1.6 $\mathcal{PT}$ symmetric optical systems

The idea of $\mathcal{PT}$ symmetry was first experimentally explored in optics [26]. The mathematical equivalence of Schrödinger equation with paraxial diffraction equation implies that the complex potential behaves just like the complex refractive index. The propagation constants are the eigenvalues of the paraxial equation in stead of energy eigenvalues of the Schrödinger equation. Nowadays novel artificial structures and materials are explored by designing both the real and the complex parts of the refractive index profile.

1.7 Methodology

Beam dynamics in a nonlinear media is modeled by nonlinear partial differential equations. The challenge in the study of the nonlinear systems is that the nonlinear partial differential equations are not exactly solvable. Hence semi-analytic, numerical and perturbation methods are used for solving these equations. We have employed the variational method and finite difference beam propagation method for studying these systems. Spectral methods and iterative methods are employed for solving the ordinary differential equations.

1.7.1 Variational method

The variational method was first proposed by Whitham [27]. This is a semi-analytical method based on the average Lagrangian density and the trial functions. It yields quite general results, but requires judicious selection of trial functions. The variational method was employed to solve the nonlinear Schrödinger equation at first by Anderson [28]. The results predicted were in good agreement with that of the numerical methods and the inverse scattering method. Since then the variational method has been employed by so many authors [29, 30, 31, 32, 33, 34].

The variational method needs the Lagrangian of the system under study. The

reduced Lagrangian is constructed from a suitable trial function with various unknown parameters. The variation of each unknown parameter with respect to the reduced Lagrangian is evaluated. The resultant evolution equations are called Euler-Lagrange equations. The solutions of the system is obtained from these equations.

Lagrangian formalism

Lagrangian formalism is based on the Hamilton's principle which states that the evolution of the infinite dimensional system is given by the expression [35]:

$$\delta I = \delta \int \int L(\Psi, \Psi^*, \Psi_x, \Psi_x^*, \Psi_z, \Psi_z^*, x, z) dz dx = 0, \tag{1.21}$$

where L is the Lagrangian functional of the system. The resulting Euler equation which is known as Lagrangian equation, is expressed as:

$$\frac{\partial}{\partial z}\frac{\partial L}{\partial \Psi_z} + \frac{\partial}{\partial x}\frac{\partial L}{\partial \Psi_x} - \frac{\partial L}{\partial \Psi} = 0.$$

Lagrangian of the dissipative systems include the conservative L_C and the non-conservative L_{NC} terms [35] such that $L = L_C + L_{NC}$. Then Lagrangian equation is restated as:

$$\frac{\partial}{\partial z}\frac{\partial L_C}{\partial \Psi_z} + \frac{\partial}{\partial x}\frac{\partial L_C}{\partial \Psi_x} - \frac{\partial L_C}{\partial \Psi} = Q, \qquad \text{where}$$
$$Q = \frac{\partial}{\partial z}\frac{\partial L_{NC}}{\partial \Psi_z} + \frac{\partial}{\partial x}\frac{\partial L_{NC}}{\partial \Psi_x} - \frac{\partial L_{NC}}{\partial \Psi},$$

where Q incorporates all dissipative processes.

The Ritz optimization procedure is applied to solve the system. In this method, a set of judiciously chosen trail functions are selected and the variation of the reduced Lagrangian is made to vanish. The reduced Lagrangian of the system is given by:

$$< L >= \int L(\Psi, \Psi^*, \Psi_x, \Psi_x^*, \Psi_z, \Psi_z^*, x, z)) dx.$$

The variational method for dissipative systems are developed by Kontrovitch [36, 37] which is stated as:

$$\frac{\partial}{\partial z}\frac{\partial < L >}{\partial \eta_{iz}} + \frac{\partial}{\partial x}\frac{\partial < L >}{\partial \eta_{ix}} - \frac{\partial L}{\partial \eta_i} = Re \int Q \frac{\partial \Psi^*}{\partial \eta_i} dx,$$

η_i being the variational parameters in the trial solution.

1.7.2 Finite Difference Beam Propagation Method

In this method, the partial differential equations are replaced by the approximations obtained from Taylor expansion nearest to the point of interest. The dynamical equation is descretized by imposing a rectangular grid on the problem.

Consider a function u and its derivative which are finite, single-valued, and continuous functions of x. Taylor expansion of u is obtained as:

$$\begin{aligned} u(x+h) &= u(x) + hu'(x) + \frac{h^2}{2}u''(x) + \frac{h^3}{6}u'''(x) + ..., \\ u(x-h) &= u(x) - hu'(x) + \frac{h^2}{2}u''(x) - \frac{h^3}{6}u'''(x) + ..., \end{aligned} \tag{1.22}$$

where the superscript $'$ represents the derivative with respect to x. Addition and substraction of these equations provide the second derivative and first derivative respectively by neglecting higher powers of h. The corresponding expressions are given by:

$$\begin{aligned} u''(x) &= \frac{\partial^2 u}{\partial x^2} \simeq \frac{1}{h^2}(u(x+h) - 2u(x) + u(x-h)), \\ u'(x) &= \frac{\partial u}{\partial x} \simeq \frac{1}{2h}(u(x+h) - u(x-h)), \end{aligned}$$

having an error of h^2. If u is a function of x and z, a rectangular grid is imposed on the $x - z$ plane such that $x = jh$ and $z = nk$ with j and n are integers. The

derivatives can be written as:

$$(\frac{\partial^2 u}{\partial x^2})_{j,n} = \frac{1}{h^2}(u_{j+1}^n - 2u_j^n + u_{j-1}^n), \tag{1.23}$$

$$\frac{\partial u}{\partial z} = \frac{1}{k}(u_j^{n+1} - u_j^n), \tag{1.24}$$

where the forward difference approximation is used for $\frac{\partial u}{\partial z}$.

Crank-Nicolson implicit method

In this method, the forward difference approximation is used for $\frac{\partial u}{\partial z}$. The central difference approximation for $\frac{\partial^2 u}{\partial x^2}$ is given by:

$$(\frac{\partial^2 u}{\partial x^2})_{j,n} = \frac{1}{2}(\frac{u_{j+1}^{n+1} - 2u_j^{n+1} + u_{j-1}^{n+1}}{h^2} + \frac{u_{j+1}^n - 2u_j^n + u_{j-1}^n}{h^2}). \tag{1.25}$$

For describing the method, consider the NLSE in the form given below:

$$i\frac{\partial u}{\partial z} = \frac{\partial^2 u}{\partial x^2} + |u|^2 u. \tag{1.26}$$

A one dimensional beam propagates through the nonlinear medium. The output field at $z = L$ is obtained from its initial value at $z = 0$. The medium is divided into equally spaced intervals by k along the propagation direction. The finite difference form of the NLSE is expressed as:

$$\frac{i}{k}(u_j^{n+1} - u_j^n) = \frac{1}{2}(\frac{u_{j+1}^{n+1} - 2u_j^{n+1} + u_{j-1}^{n+1}}{h^2} + \frac{u_{j+1}^n - 2u_j^n + u_{j-1}^n}{h^2}) + \frac{1}{2}(|u_j^{n+1}|^2 u_j^{n+1} + |u_j^n|^2 u_j^n). \tag{1.27}$$

Rearranging the equation:

$$C_j u_{j+1}^{n+1} + B_j u_j^{n+1} + A_j u_{j-1}^{n+1} = -C_j u_{j+1}^n + B_j u_j^n - A_j u_{j-1}^n, \tag{1.28}$$

where $A_j = -\frac{k}{2h^2} = C_j$, $B_j = i + \frac{k}{2h^2} - \frac{k}{2}|u_j|^{n+1}$, and $D_j = i - \frac{k}{2h^2} + \frac{k}{2}|u_j|^n$. Equation 1.28 is in the form $AU = D$, where A is tridiagonal matrix which is

expressed as:

$$\begin{pmatrix} B_1 & C_1 & 0 & 0 & 0 & . & . & . \\ A_1 & B_2 & C_2 & 0 & 0 & . & . & . \\ 0 & A_2 & B_3 & C_3 & 0 & . & . & . \\ 0 & 0 & A_3 & B_4 & C_4 & . & . & . \\ . & . & . & & & & & \\ & & & & A_{n-2} & B_{n-1} & C_{n-1} & \\ . & . & . & & & A_{n-1} & B_n & \end{pmatrix} \begin{pmatrix} u_1 \\ u_2 \\ u_3 \\ . \\ . \\ . \\ u_n \end{pmatrix} = \begin{pmatrix} d_1 \\ d_2 \\ d_3 \\ . \\ . \\ . \\ d_n \end{pmatrix} \quad (1.29)$$

The output field U will be obtained as:

$$U = A^{-1}D. \quad (1.30)$$

1.7.3 Pseudo-spectral methods

In pseudo-spectral method, the partial differential equations are solved point wise in physical space (x, t) just like finite difference method [38, 39]. But the space derivatives are evaluated using orthogonal functions. To illustrate the method, consider an ordinary or partial differential equation of the form:

$$\mathcal{L}u = g. \quad (1.31)$$

Here $u(x, t)$ is the solution. The boundary conditions at $x = \pm 1$ depends $\mathcal{L}$ and $g(x, t)$ is the source term. The basic principle is to approximate the solution with a finite sum:

$$u(x, t) \approx u_n(x, t) = \Sigma_{k=1}^{n} v_k(t)\phi_k(x), \quad (1.32)$$

where $\phi_k(x)$ is the set of basis functions and $v_k(t)$ is the coefficient of expansion. A set of orthogonal functions are chosen for basis functions such as Fourier integrals, Chebyshev polynomials e.t.c. The expansion coefficients are calculated

using the residual function $\mathcal{R}$ which is defined as:

$$\mathcal{R}[u_n(x,t)] := [\mathcal{L}u_n - g](x,t). \tag{1.33}$$

$\mathcal{R}$ is evaluated from equation 1.32. The residual norm $\|\mathcal{R}\|$ is a measure of the quality of the approximate solution. $\mathcal{R}$ should be as small as possible across the domain. The spectral coefficients $\{v_k\}_{k=0}^{N}$ are chosen so that they satisfy the boundary conditions. Rest of the spectral coefficients are evaluated such that $\mathcal{R}[u_n(x,t)]$ vanishes as many spatial points as possible.

The solution at the collocation points are exact whereas interpolation provides the solution in between the collocation points. Chebyshev polynomials are used for interpolation. Chebyshev points are defined as $x_j = cos(\frac{j\pi}{N})$ where $j = 0, 1, 2, ..., N$. The pseudo-spectral method works well for smooth functions with geometrical convergence.

1.7.4 Newton's Conjugate Gradient method

Newton's conjugate gradient method is one of the iterative methods mainly used for the computation of solitary waves. Basic principle involves Newton iterations. The resultant linear Newton correction equation is solved using conjugate-gradient iterations [40].

Consider solitary waves in a nonlinear media with arbitrary spatial dimensions of the form:

$$\mathbf{L_0 u}(\mathbf{x}) = \mathbf{0}, \tag{1.34}$$

where $\mathbf{x}$ is a vector and $\mathbf{u}(\mathbf{x})$ is a real-valued solitary wave. $|\mathbf{u}(\mathbf{x})| \rightarrow \mathbf{0}$ for $|\mathbf{x}| \rightarrow \infty$.

For the illustration of the method, let the dynamics of the system is described with the nonlinear Schrödinger equation:

$$i\frac{\partial U}{\partial t} + \frac{\partial^2 U}{\partial x^2} + |U|^2 U = 0. \tag{1.35}$$

The solitary wave satisfies the relation $U(x,t) = u(x)e^{i\mu t}$, where μ is the propagation constant. Substituting in equation 1.35:

$$\frac{d^2u}{dx^2} - \mu u + u^3 = 0. \tag{1.36}$$

In the case of complex-valued solitary waves, the equation can be expressed in the above form with u consisting of real and imaginary parts of the solution.

Iterative methods are employed to solve equation 1.34. Let $u_n(x)$ is an approximate solution. This should be close to the exact solution $u(x)$. Now the exact solution satisfies the relation:

$$\mathbf{u(x) = u_n(x) + e_n(x)}, \tag{1.37}$$

where $e_n(x) << 1$ is the error. Substituting in equation 1.34 and expanding about $u_n(x)$ yields:

$$\mathbf{L_0 u_n + L_{1n} e_n = O(e_n^2)}, \tag{1.38}$$

in which $\mathbf{L_{1n}}$ is the linearization operator evaluated at the approximate solution u_n. Neglecting higher order terms of $\mathbf{e_n}$ on the equation 1.38, the remaining equation is linear inhomogeneous equation for $\mathbf{e_n}$. Hence we can update the solution such that:

$$\mathbf{u_{n+1}(x) = u_n(x) + \Delta u_n(x)}, \tag{1.39}$$

$\Delta\mathbf{u_n}$ being the updated amount. This term can be evaluated from the linear inhomogeneous equation for $\mathbf{e_n}$ which is rewritten as:

$$\mathbf{L_{1n} \Delta u_n = -L_0 u_n}. \tag{1.40}$$

Up to this, the method is equivalent to Newton iterations. Equation 1.40 is solved by using conjugate-gradient iterations. The preconditioned conjugate gradient

method is used for self-adjoint linearization operators and dropping the subscripts n as given below:

$$\begin{aligned}
\Delta\mathbf{u}^{(\mathbf{0})} &= 0, \\
\mathbf{R}^{(\mathbf{0})} &= -\mathbf{L_0 u}, \\
\mathbf{D}^{(\mathbf{0})} &= \mathbf{M^{-1}R}^{(\mathbf{0})}, \\
a^{(i)} &= \frac{\langle \mathbf{R}^{(\mathbf{i})}, \mathbf{M^{-1}R}^{(\mathbf{i})} \rangle}{\langle \mathbf{D}^{(\mathbf{i})}, \mathbf{L_1 D}^{(\mathbf{i})} \rangle}, \\
\Delta\mathbf{u}^{(\mathbf{i+1})} &= \Delta\mathbf{u}^{(\mathbf{i})} + \mathbf{a}^{(\mathbf{i})}\mathbf{D}^{(\mathbf{i})}, \\
\mathbf{R}^{(\mathbf{i+1})} &= \mathbf{R}^{(\mathbf{i})} - \mathbf{a}^{(\mathbf{i})}\mathbf{L_1 D}^{(\mathbf{i})}, \\
b^{(i+1)} &= \frac{\langle \mathbf{R}^{(\mathbf{i+1})}, \mathbf{M^{-1}R}^{(\mathbf{i+1})} \rangle}{\langle \mathbf{R}^{(\mathbf{i})}, \mathbf{M^{-1}R}^{(\mathbf{i})} \rangle}, \\
\mathbf{D}^{(\mathbf{i+1})} &= \mathbf{M^{-1}R}^{(\mathbf{i+1})} + \mathbf{b}^{(\mathbf{i+1})}\mathbf{D}^{(\mathbf{i})},
\end{aligned}$$

where $i = 0, 1, 2, ...$ is the index of conjugate-gradient (CG) iterations. The inner product is defined as:

$$\langle \mathbf{F_1}, \mathbf{F_2} \rangle = \int_{-\infty}^{\infty} \mathbf{F}_\mathbf{1}^\dagger . \mathbf{F_2 dx},$$

in which † denotes the Hermitian of a vector. $\mathbf{M}$ is the pre-conditioning operator for accelerating the convergence of the conjugate-gradient iterations and it should be easily invertible. Generally it is chosen as the linear differential part of $\mathbf{L_0}$.

The CG iterations are terminated depending on certain accuracy of $\Delta\mathbf{u}^{(\mathbf{i})}$. The error of this solution is the residue $\mathbf{R}^{(\mathbf{i})} = -\mathbf{L_0 u_n} - \mathbf{L_{1n}}\boldsymbol{\Delta}\mathbf{u}_\mathbf{n}^{(\mathbf{i})}$ and whose $\mathbf{M^{-1}}$ weighted norm is given by:

$$\|\mathbf{R}^{(\mathbf{i})}\|_\mathbf{M} \equiv \langle \mathbf{R}^{(\mathbf{i})}, \mathbf{M^{-1}R}^{(\mathbf{i})} \rangle^{\frac{1}{2}}. \tag{1.41}$$

The CG iterations are terminated by checking the criterion:

$$\|\mathbf{R}^{(\mathbf{i})}\|_\mathbf{M} < \epsilon_\mathbf{cg} \|\mathbf{R}^{(\mathbf{0})}\|_\mathbf{M}, \tag{1.42}$$

where ϵ_{cg} is the error tolerance parameter which lies between 10^{-1} and 10^{-3}. The accuracy of the solution is set as 10^{-10}. Conjugate-Gradient method is embedded inside the Newton iterations and so the method is called Newton Conjugate-Gradient (NCG) method.

1.8 Outline of the thesis

The thesis presents a theoretical study of beam dynamics in single and coupled $\mathcal{PT}$ symmetric systems focusing on Kerr and nonlocal nonlinearity. The variational and numerical methods are employed for the analysis. Finite difference beam propagation method is used to study the evolution of beam in nonlinear media as it propagates. Newton's Conjugate-Gradient method is applied for steady-state nonlinear equations and pseudo-spectral method for linear stability analysis.

Chapter 2 deals with the single-hump and double-hump solitons in a system with $\mathcal{PT}$ symmetric complex potential having Kerr nonlinearity. The $\mathcal{PT}$ symmetric parabolic potential of the form $\frac{kx^2}{2} - i\epsilon x$, has been chosen for analysis, where k and ϵ represent the strength of the real part of the potential and the strength of the loss term (imaginary part of the potential) respectively. The system undergoes spontaneous $\mathcal{PT}$ symmetric phase transition from the $\mathcal{PT}$ symmetric region to the broken $\mathcal{PT}$ symmetric region depending on the strength of the imaginary part of the potential. The coefficient of the imaginary part of the potential at which the phase transition occurs is known as the threshold value. The $\mathcal{PT}$ symmetric phase transition point has been studied by varying the strength of real part of the potential and the coefficient of the nonlinearity. The linear stability analysis reveals that the stable solitons are formed for low values of the coefficients of imaginary part of the potential and nonlinearity.

In chapter 3, the higher eigenmodes of the gap solitons in a $\mathcal{PT}$ symmetric periodic potential with a defocusing nonlocal nonlinearity have been described. The double-hump nonlocal gap solitons exist above a threshold value of energy

and spread through two neighboring channels in the $\mathcal{PT}$ symmetric region. The power carried by the imaginary component of the double-hump soliton increases with the imaginary part of the complex potential. The total power is invariant with respect to the strength of the imaginary part of the potential and the range of the nonlocality. The power of the soliton increases with the propagation constant or energy. The double-hump soliton exists in the $\mathcal{PT}$ symmetric domain whereas it dies out in the broken $\mathcal{PT}$ symmetric region. The linear stability of the double-hump solitons are studied using Bogoliobov-De-Genes equations. The double-hump solitons are unstable and the perturbation modes vary exponentially.

Chapter 4 describes the $\mathcal{PT}$ symmetric coupler in transverse real periodic and aperiodic potentials with Kerr nonlinearity for linear and nonlinear regime. The propagation-invariant solutions of the system have been studied and found that the high frequency solitons reside in the minimum of the periodic and aperiodic potentials. The high strength of the periodic potential causes the soliton to be more confined in the lattice whereas high depth of the parabolic potential leads to the confinement of the soliton at minimum value of the potential. The linear coupler possesses real eigenvalues when the gain/loss coefficient is less than the coupling coefficient for both periodic and aperiodic potentials. The transverse periodic potential modulates the amplitude of the beam and causes the formation of bands in the unbroken regime. The beam get trapped in the channel with gain in the case of periodic and aperiodic potentials for nonlinear coupler. The linear stability analysis reveals that the high frequency soliton is stable for both periodic and aperiodic potentials.

The $\mathcal{PT}$ symmetric coupler with transverse real periodic potential having defocusing nonlocal nonlinearity has been studied in chapter 5. The high-frequency and the low-frequency modes with single-hump, double-hump and triple-hump structures are obtained. The high-frequency multi-hump modes are observed in the first band gap. The low-frequency single-hump modes lie in the semi-infinite band gap whereas low-frequency double-hump and triple-hump modes

lie in the first band gap. The single-hump modes trap in the minimum of the potential. The double-hump modes spread through the two consecutive lattice while triple-hump modes lie across three consecutive lattices. As the range of the nonlocal nonlinearity varies, the propagation constants corresponding to different modes also change. The linear stability analysis of the high-frequency and low-frequency modes predict that both modes are stable for weak nonlocality but unstable with oscillatory instability for strong nonlocality. The studies on the propagation dynamics predict that when the range of the nonlocality increases, the width increases and the amplitude decreases, resulting in constant power propagation.

Chapter 6 deals with the switching dynamics in $\mathcal{PT}$ symmetric coupler with transverse real potentials. Both periodic and aperiodic potentials are analysed with Kerr and nonlocal nonlinearity. The power oscillates between the channels for low input intensity whereas the power is trapped in the gain channel for high input intensity in the case of weak nonlocality and low strength of the transverse potentials. We get the travelling soliton solution, if the center of the solution lies at the minimum of the transverse potentials. When the center of the solution lies at the maximum of the periodic potential, the soliton get trapped. The power-dependent switching of the $\mathcal{PT}$ symmetric nonlocal coupler has also been studied in this chapter. The critical power increases with the range of the nonlocality and the strength of the transverse potential. The switching from channel with gain to channel with loss is possible for high input power by varying either the range of the nonlocality or the strength of the transverse periodic potential.

Chapter 7 summarizes the findings of the thesis and describes future prospects of this work.

Bibliography

[1] N. N. Akhmediev and A. A. Ankiewicz. Solitons Nonlinear Pulses and Beams. Chapman and Hall, London, 1997.

[2] G. P. Agrawal. Nonlinear Fiber Optics. Academic Press, SaIl Diego, California, 2001.

[3] A. Hasegawa and F. D. Tappert. Transmission of stationary nonlinear optical pulses in dispersive dielectric fibers. I. anomalous dispersion. Appl. Phys. Lett. 1973;23:142.

[4] L. F. Mollenauer, R. H. Stolen, J. P. Gordon, and W. J. Tomlinson. Extreme picosecond pulse narrowing by means of soliton effect in single-mode optical fibers. Opt. Lett. 1983;8:289.

[5] J. E. Bjorkholm and A. A. Ashkin. cw self-focusing and self-trapping of light in sodium vapor. Phys. Rev. Lett., 1974;32 129132.

[6] B. A. Dubrovin and S. P. Novikov. Hydrodynamics of weakly deformed soliton lattices,differential geometry and hamiltonian theory. Phys. Rev. A. 1989;44 35124.

[7] Bishnu Pal, editor. Frontiers in Guided Wave Optics and Optoelectronics. IntechOpen, 2010.

[8] George I. Stegeman and Mordechai Segev. Optical spatial solitons and their interactions: Universality and diversity. Science. 1999;286:5444 15181523.

[9] A. Hasegawa and Y. Kodma. Soliton in Optical Communication. Clarendon Press, Oxford, 1995.

[10] M. Segev and G. I. Stegeman. Selftrapping of optical beams: Spatial solitons. Physics Today. 1998;51:42.

[11] P. L.Kelley. Self-focusing of optical beams. Physical Review Letters. 1965;15:26 10051008.

[12] Y. S. Kivshar and G. P. Agrawal. Optical Solitons - From Fibers to Photonic Crystals. Academic Press, San Diego, California, 2003.

[13] Allan W. Snyder and D. John Mitchell. Accessible solitons. Science. 1997;276:5318 15381541.

[14] W.Krolikowski and O.Bang and N.I.Nikolov and D.Neshev and J.Wyller and J.J.Rasmussen and D.Edmundson. Modulational instability, solitons and beam propagation in spatially nonlocal nonlinear media. J. Opt. B: QuantumSemiclass.Opt. 2004;6 S288-S294.

[15] D.Suter and T.Blasberg. Stabilization of transverse solitary waves by a nonlocal response of the nonlinear medium. Phys. Rev. A. 1993;48:4583.

[16] Cssio E. A. Santos and Mrcio A. R. C. Alencar and Pedro Migowski and Jairton Dupont and Jandir M. Hickmann. Nonlocal nonlinear optical response of ionic liquids under violet excitation. Advances in Materials Science and Engineering. 2013;2013:104914.

[17] S. Skupin and M. Saman and W. Krolikowski. Nonlocal stabilization of nonlinear beams in a self-focusing atomic vapor. Phys. Rev. Lett. 2007;98:263902.

[18] M.Karpierz. Solitary waves in liquid crystalline waveguides. Phys. Rev. E. 2002;66:036603.

[19] O.Bang and W.Krlikowski and J.Wyller and J.Rasmussen. Collapse arrest and soliton stabilization in nonlocal nonlinear media. Phys. Rev. E. 2002;66:046619 11.

[20] T.A.Davydova and A.I.Fishchuk. Stable spatial coherent wave structures in normal and anomalous dispersive regimes in plasmas. Ukr. J. Phys. 1995;40:487.

[21] W.Krolikowski and O.Bang. Solitons in nonlocal nonlinear media: Exact solutions. Phys. Rev. E. 2001;63:016610.

[22] H.Goldstein. Classical mechanics. Narosa Publishing House, 1980.

[23] C.M.Bender and S.Boettcher. Real spectra in non-hermitian hamiltonians having pt symmetry. Phys. Rev. Lett. 1998;80 52435246.

[24] C.M.Bender and D.C.Brody and H.F.Jones. Complex extension of quantum mechanics. Phys. Rev. Lett. 2004;92:119902.

[25] V.V.Konotop and J.Yang and D.A.Zezyulin. Nonlinear waves in PT-symmetric systems. Rev. Mod. Phys. July 2016;88.

[26] R.El-Ganainy and K.G.Makris and D.N.Christodoulides and Z.H.Musslimani. Theory of coupled optical PT-symmetric structures. Opt. Lett. 2007;32:2632.

[27] G.B.Whitham. Linear and Nonlincar Waves. John Wiley and Sons, New York, 1974.

[28] D.Anderson. Variational approach to nonlinear pulse propagation in optical fibers. Phys. Rev. A. 1983;27 31353145.

[29] M.Karlsson and D.AndersoIl and A.Hook and M.Lisak. A variational approach to optical soliton collisions. Phys. Scr. 1994;50 265270.

[30] N.F.Smyth and A.L.Worthy. Dispersive radiation and nonlinear twin-core fibers. J. Opt. Soc. Am. B. 1997;14 26102617.

[31] M.Chen and D.J.Kaup and B.A.Malomed. Three-wave solitons and continuous waves in media with competing quadratic and cubic nonlinearities. Phys. Rev. E. 2004;69:056605.

[32] P.A.Subha and C.P.Jisha and V.C.Kuriakose. Nonlinearity management and diffraction management for the stabilization of two-dimensional spatial solitons. Pramana. 2007;69:229239.

[33] R.K.Lee and G.Assanto and C.P.Jisha and A.Alberucci. Deflection and trapping of spatial solitons in linear photonic potentials. Opt Express. 2013;21:16 1864618660.

[34] P.A.Subha and K.A.Muhsina. Stabilization of two-dimensional spatial solitons in dissipative media. Physica Scripta. 2014;89:7 075205.

[35] G.B.Arfken and H.J.Weber. Mathematical methods for physicists. Elsevier Academic Press, 2005.

[36] S.Chvez Cerda and S.B.Cavalcanti and J.M.Hickmann. A variational approach of nonlinear dissipative pulse propagation. Eur. Phys. J. D. 1998;1 313316.

[37] V.Skarka and N.B.Aleksic. Stability criterion for dissipative soliton solutions of the one, two, and three-dimensional complex cubic-quintic ginzburglandau equations. Phys. Rev. Lett. 2006;96 013903.

[38] Denys Dutykh. A brief introduction to pseudo-spectral methods: application to diffusion problems. arXiv:1606.05432v1, 2016.

[39] Lloyd N.Trefethen. Spectral Methods in Matlab. SIAM, Philadelphia, 2000.

[40] J.Yang. Newton-conjugate-gradient methods for solitary wave computations. J. Comput. Phys. 2009;228 7007-7024.

SUNEERA T. P. “STUDIES ON BEAM DYNAMICS IN SINGLE AND COUPLED PARITY-TIME SYMMETRIC SYSTEMS WITH KERR AND NONLOCAL NONLINEARITY”. THESIS. DEPARTMENT OF PHYSICS, UNIVERSITY OF CALICUT, 2018.

Chapter 2

Beam dynamics in Kerr media having $\mathcal{PT}$ symmetric aperiodic potential

2.1 Introduction

$\mathcal{PT}$ symmetry in nonlinear optics have been extensively studied because of its potential applications in optical fiber communication systems and in photonics. Though the system contains dissipative term, it exhibits many features of conservative systems like the real linear spectra and the stable nonlinear eigenmodes with continuous energy values.

The existence of real spectra of $\mathcal{PT}$ symmetric Hamiltonians has been reported first in parabolic complex potential of the form $(x - i\alpha)^2$, where α is a real parameter [1]. The studies have been reported in $\mathcal{PT}$ symmetric polynomial potentials and the $\mathcal{PT}$ symmetric cubic anharmonic oscillator potentials [2, 3, 4]. Solitons in $\mathcal{PT}$ symmetric optical systems exhibit unique features. Optical solitons in $\mathcal{PT}$ symmetric periodic potential has been studied in Kerr media [5]. A series of studies have been reported in Kerr media with different types of $\mathcal{PT}$ symmetric potentials [6, 7, 8, 9] and in optical lattices [10, 11, 12, 13].

The parabolic potential which is in the fundamental Harmonic oscillator problem, is a simplest model of potentials. Parabolic refractive index in crystals, optical fibers and harmonic trap in Bose-Einstein Condensates are some modern applications of this potential. $\mathcal{PT}$ symmetric counter part of the parabolic potential has been used to model the system.

In this chapter we have studied the single-hump and the double-hump solitons of a system having $\mathcal{PT}$ symmetric complex potential [14]. The variational and the numerical methods have been employed to analyze the system. The ground state of the system has been studied in linear and nonlinear regime. The stability analysis of the fundamental mode has been addressed. We have extended the study to the double-hump structure in linear and nonlinear regime.

2.2 The theoretical model

The solitons in a $\mathcal{PT}$ symmetric complex potential is given by the one dimensional equation:

$$i\frac{\partial\Psi}{\partial t} = -\frac{1}{2}\frac{\partial^2\Psi}{\partial x^2} + (\frac{1}{2}kx^2 - i\epsilon x)\Psi + 2g\left|\Psi\right|^2\Psi, \tag{2.1}$$

where k and ϵ are the strengths of the real and the imaginary part of the potential respectively and g is the coefficient of the nonlinearity. x represents the transverse coordinate whereas t denotes the propagation direction (z for optical systems). The $\mathcal{PT}$ symmetric complex potential of the system is given by:

$$V(x) = V_R(x) - iV_I(x), \tag{2.2}$$

where $V_R(x) = \frac{1}{2}kx^2$ and $V_I(x) = \epsilon x$.

The particle density of the matter wave solitons (intensity in optics) is given by $\rho = \left|\Psi\right|^2$ and hence the particle number of the matter wave solitons P, is

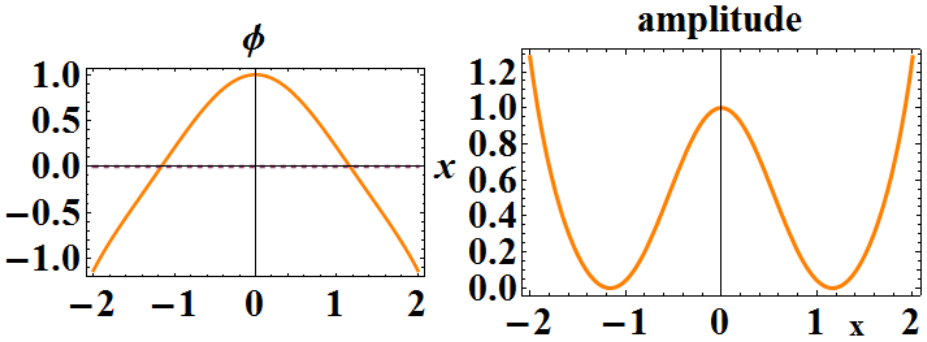

(a) (b)

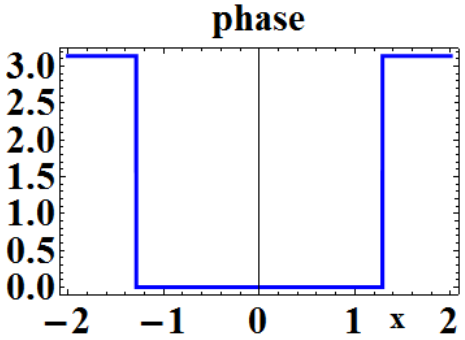

(c)

Figure 2.1: The linear case for real potential ($\epsilon = 0$). (a) The eigenstates, the real by orange and the imaginary by dotted purple, (b) the amplitude (particle density), and (c) the phase profile along the transverse direction.

obtained by [15]:

$$P = \int_{-\infty}^{\infty} |\Psi|^2 \, dx = \int_{-\infty}^{\infty} \rho dx, \tag{2.3}$$

which is analogous to the power in optical systems. The particle conservation for a $\mathcal{PT}$ symmetric system is obtained from the continuity equation which reads:

$$\nabla . j = -\frac{\partial \rho}{\partial t} + 2V_I(x)\rho, \tag{2.4}$$

where j is the particle flux and is given by:

$$j = \frac{1}{2i}(\Psi^* \frac{\partial \Psi}{\partial x} - \Psi \frac{\partial \Psi^*}{\partial x}). \tag{2.5}$$

2.2.1 The Stationary states

The steady state is obtained from the equation 2.1 by substituting for $\Psi(x,t)$:

$$\Psi(x,t) = \phi(x)e^{-i\mu t},$$

which can be written as:

$$-\frac{1}{2}\frac{d^2\Phi}{dx^2} + (\frac{1}{2}kx^2 - i\epsilon x - \mu)\phi + 2g\left|\phi\right|^2\phi = 0, \tag{2.6}$$

where μ is the chemical potential of the system.

Now $\rho = |\phi|^2$ and $j = \frac{1}{2i}(\phi^* \frac{\partial \phi}{\partial x} - \phi \frac{\partial \phi^*}{\partial x})$. Assuming $\phi = \sqrt{\rho}e^{i\xi(x)}$, the flux reads as $j = \rho \frac{\partial \xi}{\partial x}$. For stationary states, $\frac{\partial \rho}{\partial t} = 0$, holds valid. The equation for the particle conservation has been obtained from equation 2.4:

$$\frac{\partial}{\partial x}(\rho \frac{\partial \xi}{\partial x}) = 2V_I(x)\rho. \tag{2.7}$$

The stationary states feature a nonflat phase profile on x. Equation 2.4 represents the motion of particles from the gain to the loss region as required to conserve the overall particle number in the presence of $V_I(x)$ [15]. Equation 2.6 has been studied numerically to get the stationary states of the system.

2.2.2 The Dynamical States

The dynamics of the system have been analyzed both variationally and numerically. The model equation is obtained from the equation 2.1 by substituting

$$\Psi(x,t) = \phi(x,t)e^{-i\mu t}$$

which results in:

$$-\frac{1}{2}\frac{\partial^2\phi}{\partial x^2}+(\frac{1}{2}kx^2-i\epsilon x-\mu)\phi+2g\left|\phi\right|^2\phi=i\frac{\partial\phi}{\partial t}. \tag{2.8}$$

The conservative part of the Lagrangian deals with the real part of the complex $\mathcal{PT}$ symmetric potential while the nonconservative part deals with the imaginary part:

$$L_c=\frac{i}{2}(\phi\phi_t^*-\phi^*\phi_t)+\frac{1}{2}\mid\phi_x\mid^2-\frac{1}{2}kx^2\mid\phi\mid^2+g\mid\phi\mid^4, \tag{2.9}$$

$$L_{nc}=-i\epsilon x\mid\phi\mid^2. \tag{2.10}$$

The reduced Lagrangian of the conservative system from the infinite dimensional Lagrangian density is given by:

$$L_{eff}=\int_0^\infty L_c dx. \tag{2.11}$$

The standard variational approach to the dissipative system leads to the equations:

$$\frac{\partial}{\partial t}\frac{\partial L_{eff}}{\partial\eta_i}-\frac{\partial L_{eff}}{\partial\eta_i}=Re\int Q\frac{\partial\phi^*}{\partial\eta_i}dx, \tag{2.12}$$

where $Q=\frac{\partial L_{NC}}{\partial\phi^*}-\frac{\partial}{\partial x}\frac{\partial L_{NC}}{\partial\phi^*}$. The resulting equations are solved to study the dynamics of the system. Equation 2.8 has been simulated using Finite Difference Beam Propagation Method (FDBPM) as illustrated in section 1.7.2.

2.3 The Single-hump soliton

2.3.1 The Stationary states

Equation 2.6 has been studied numerically in the linear and nonlinear regime and the solutions are analyzed. In the linear case ($g = 0$), when $\epsilon = 0$ the system is Hermitian and the solutions are Hermite polynomials just like the harmonic oscillator problem as shown in Figures 2.1(a), 2.1(b), and 2.1(c). Figures 2.2(a)-2.2(c) elucidate the dependence of complex potential on the eigenstates, the particle density and the phase profiles of the system when $\epsilon > 0$. The phase of the solution exhibits x dependence such that $f(x) = tanh(x^3)$ under $\mathcal{PT}$ symmetric region. Figures 2.1(a) and 2.2(a) show that the real part of the solution is symmetric and the imaginary part is antisymmetric about the origin. When $\epsilon > 2$, the eigenstates exhibit instability indicating $\mathcal{PT}$ symmetric phase transition which is known as broken $\mathcal{PT}$ symmetric regime as shown in Figures 2.3(a)-2.3(c). The critical value of ϵ for which the phase transition occurs is called as threshold value ϵ_{th}.

The eigenstate, the particle density and the phase for real potential in the nonlinear regime are shown in Figures 2.4(a), 2.4(b) and 2.4(c). The system has been studied for the complex potential and the eigenstate, the particle density and the phase are plotted in Figures 2.5(a)-2.5(c). The solitons exist below the $\mathcal{PT}$ threshold as shown in Figure 2.5(a) and corresponding particle density and phase are plotted in Figures 2.5(b) and 2.5(c) respectively. Figure 2.6(a) reveals that the soliton solutions do not exist in the the broken $\mathcal{PT}$ symmetric regime. The eigenstate exhibits instability in the form of oscillatory divergence towards the tail of the broken $\mathcal{PT}$ symmetric regime. The corresponding particle density and phase are plotted in Figures 2.6(b) and 2.6(c) respectively.

2.3.2 The propagation

The dynamical states have been studied variationally using the Gaussian profile as the variational ansatz [15] which has the form:

$$\psi(x,t) = A(t)\, e^{[\frac{-x^2}{2a^2(t)} + \frac{ix^2 b(t)}{2} + if(x)\theta(t)]}, \tag{2.13}$$

where A, a, b and θ represent time depending amplitude, the width, the wavefront curvature and the phase respectively. The particle number of the fundamental soliton is given by,

$$P = \frac{A^2 a\sqrt{\pi}}{4}. \tag{2.14}$$

The particle number depends on the amplitude and the width of the Gaussian profile. The variational analysis leads to four coupled equations:

$$A_t = \frac{Ab}{2} - \epsilon Aa(\frac{9\sqrt{\pi}}{4} - \frac{16}{\sqrt{\pi}}) + \theta Aa(\frac{81\sqrt{\pi}}{8} - \frac{48}{\sqrt{\pi}}), \tag{2.15}$$

$$a_t = -ab + \epsilon a^2(\frac{3\sqrt{\pi}}{2} + \frac{8}{\sqrt{\pi}}) - \theta a^2(\frac{27\sqrt{\pi}}{4} - \frac{24}{\sqrt{\pi}}, \tag{2.16}$$

$$b_t = 3b^2 - k - \frac{5}{a^4} - \frac{24g}{\sqrt{2}a^2} - 27\theta^2 a^2 + \frac{12\mu}{a^2}, \tag{2.17}$$

$$\theta_t = \frac{\sqrt{\pi}}{2a^5} + \frac{g\sqrt{2}}{a^3} + \frac{\mu}{a^3} + \frac{27\theta^2 a}{4} + \frac{3\theta b}{\sqrt{\pi}}. \tag{2.18}$$

Equations 2.15-2.18 have been studied both in linear and nonlinear regime.

Figures 2.7(a), 2.7(c) and 2.7(e) describe the evolution of the amplitude, the width and the particle number for various values of ϵ keeping the strength of real part of the potential unity (i.e., $k = 1$) in the linear regime. For real potential, the amplitude decreases whereas the width increases and the particle number is a constant as shown in Figure 2.7(a). In the case of the complex potential ($\epsilon > 0$), the amplitude decreases and the width increases in the unbroken $\mathcal{PT}$ symmetric regime just like in the real potential. It supports the solutions as plotted in Figure 2.7(c). For $k = 1$, $\epsilon = 0.13$ shows $\mathcal{PT}$ symmetric phase transition and

this value is called ϵ threshold (ϵ_{th}). When ϵ is increased further, the amplitude and the width decrease and spontaneous $\mathcal{PT}$ symmetric break down occurs as plotted in Figure 2.7(e). The amplitude, the width and the particle number increase and the solution collapses in the broken $\mathcal{PT}$ symmetric region.

When the width increases, the amplitude decreases keeping the particle number constant for real potential in the nonlinear regime as shown in Figure 2.7(b). In the unbroken $\mathcal{PT}$ symmetric region, the presence of the complex potential still keeps the particle number same, but amplitude decreases and the width increases as plotted in Figure 2.7(d). Beyond $\mathcal{PT}$ symmetric breaking point the particle number increases and in this regime the solitons collapse as evident from Figure 2.7(f).

We have solved equation 2.1 numerically using the finite difference method to determine the dynamics of the system assuming the variational ansatz as initial solution. Figure 2.8(a) shows the solution for real potential with $g = 0$. In the case of the complex potential with $g = 0$, (i.e, linear case) the solutions exist for the unbroken $\mathcal{PT}$ symmetric regime as shown in Figure 2.8(c). When the strength of the complex part of the potential increases, the system exhibits the $\mathcal{PT}$ symmetric phase transition above which the particle number is not a constant. This regime is known as broken $\mathcal{PT}$ symmetric regime and is plotted in Figure 2.8(e). For the nonlinear case the studies have shown that the system in the $\mathcal{PT}$ symmetric regime supports the solitons as shown in Figures 2.8(b) and 2.8(d). Figure 2.8(f) is plotted for broken $\mathcal{PT}$ symmetric regime in which the soliton collapses. The $\mathcal{PT}$ phase transition point increases linearly with the strength of the nonlinearity as shown in Figure 2.9(a).

Figure 2.9(b) elucidates the variation of the $\mathcal{PT}$ phase transition point (ϵ_{th}) with the strength of real part of potential k. As k increases, the $\mathcal{PT}$ symmetric threshold decreases.

It is found that the results of the variational analysis agree with the results of the direct simulation of equation 2.1. The system supports single-hump soliton in the $\mathcal{PT}$ symmetric regime. As the nonlinearity increases, the ϵ_{th} also increases.

By varying the strength of the nonlinearity we can change the $\mathcal{PT}$ symmetric breaking point of the system.

2.3.3 Linear stability analysis

The stability of the stationary solutions has been discussed using the Bogoliubov-de Genes (BDG) equations which are obtained by considering the effect of small perturbations in the form [15]:

$$\Psi(x,t) = (\phi(x) + p(x)e^{i\Omega t} + q(x)e^{-i\Omega t})e^{i\mu t}. \tag{2.19}$$

This gives the linearized BDG equations as:

$$\Omega \begin{pmatrix} p \\ q^* \end{pmatrix} = \begin{pmatrix} L - iV_i(x) & \phi^2 \\ -(\phi^*)^2 & -L - iV_i(x) \end{pmatrix} \begin{pmatrix} p \\ q^* \end{pmatrix}, \tag{2.20}$$

where $L = -\mu - \frac{1}{2}\frac{\partial^2}{\partial x^2} + \frac{1}{2}kx^2 + 2g|\phi|^2$ and Ω is the perturbation eigenvalue.

The solution is stable if imaginary part of Ω ($imag\Omega$) is equal to zero, holds for all the eigenvalues. Purely imaginary eigenvalues represent the unstable perturbation modes. The existence of complex eigenvalues lead to an oscillatory instability with $imag\Omega > 0$ or $imag\Omega < 0$, former implies exponentially decaying modes and latter corresponds to exponentially growing modes.

We have solved the matrix equation 2.20 using pseudo-spectral technique based on Chebyshev polynomials to compute the operator L. In the case of real potential ($\epsilon = 0$), the stable solitons are obtained (i.e. $|imag\Omega|$ is negligible) for all values of g and μ.

For complex potential (i.e. $\epsilon > 0$), there is an oscillatory instability due to the eigenvalues with nonvanishing real and imaginary parts. The stability of the solutions are analyzed by varying μ, ϵ and g. The real and the imaginary parts of Ω versus μ are plotted with various values of ϵ and g as shown in Figure 2.10. For low ϵ and $g \leq 1$, the growth rate increases with μ. The $real\Omega$ decreases with μ whereas $imag\Omega$ increases with μ. The perturbation growth rate increases with

μ and slightly depends on the imaginary potential. In the case of $0 < g \leq 1$, $imag\Omega > 0$, and the stationary state perturbed solution decays exponentially on propagation along with the oscillatory instability. This is evident from first row of Figure 2.10 which is plotted for $g = 1$. When $g > 1$, $imag\Omega < 0$. So the instability grows exponentially with μ and the growth rate decreases with μ. The plots are shown in second row of Figure 2.10. The growth rate strongly depends on the strength of nonlinearity.

Summarizing the result, the stationary state perturbation modes are exponentially decaying along with the oscillatory instability for the nonlinearity, $0 < g \leq 1$. As g increases, the instability grows exponentially along with the oscillatory instability. The perturbation growth rate varies with g, μ and ϵ.

2.4 The Double-Hump Soliton

2.4.1 The Stationary States

Equation 2.6 has been studied using Newton's Conjugate Gradient method as discussed in section 1.7.4. The initial solution is assumed as Hermite-Gaussian of order 1 as given below:

$$\phi(x,t) = A\, x\, e^{[\frac{-x^2}{2a^2} + \frac{ibx^2}{2} + if(x)\theta]}, \tag{2.21}$$

where the parameters A, a, b and θ are the amplitude, the width, the wave front curvature and the phase respectively.

The stationary states of the double-hump solitons are plotted for various values of the coefficient of the imaginary part of the potential ϵ and the strength of the nonlinearity g as shown in Figures 2.11(a)-2.11(f). We found that the system supports double-hump soliton in the $\mathcal{PT}$ symmetric regime. In the linear case, Figures 2.11(a) and 2.11(c) show that the double hump solutions exist for $\epsilon = 0$ and $\epsilon = 0.1$ respectively. The solution in the broken $\mathcal{PT}$ symmetric regime ($\epsilon = 2$) is plotted in Figure 2.11(e), which shows the collapse of the soliton. For

weak nonlinearity ($g < 1$), the double-hump solitons exist as depicted in Figures 2.11(b) and 2.11(d) for $\epsilon = 0$ and $\epsilon = 0.1$ respectively. These solitons collapse in the broken $\mathcal{PT}$ symmetric regime ($\epsilon = 2$) as shown in Figure 2.11(f).

2.4.2 The Dynamics

We have assumed Hermite-Gaussian of order 1 as ansatz which is:

$$\phi(x,t) = A(t)\, x\, e^{[\frac{-x^2}{2a^2(t)} + \frac{ix^2 b(t)}{2} + if(x)\theta(t)]}, \tag{2.22}$$

where the variational parameters $A(t)$, $a(t)$, $b(t)$ and $\theta(t)$ are the amplitude, the width, the wave front curvature and the phase respectively. The particle number of the higher eigenmode is $P = \frac{A^2 a^3 \sqrt{\pi}}{4}$. The effective Lagrangian of the system is given by the equation:

$$\begin{aligned} L_{eff} = {} & \frac{3\sqrt{\pi}A^2a^5b_t}{16} + \frac{135\sqrt{\pi}a^7\theta^2A^2}{32} + \frac{A^2a\sqrt{\pi}}{4} + \frac{3k\sqrt{\pi}A^2a^5}{16} - \frac{\mu A^2a^3\sqrt{\pi}}{4} \\ & + \frac{3gA^4a^5\sqrt{\pi}}{32\sqrt{2}} + A^2a^6\theta_t + \frac{3b^2a^5A^2\sqrt{\pi}}{16} + 3\theta b a^6 A^2 - \frac{A^2a^2}{2}. \end{aligned} \tag{2.23}$$

The variational analysis provide a set of the coupled equations for the amplitude, the width, the wavefront curvature and the phase as given below:

$$A_t = \epsilon A a(\frac{16}{\sqrt{\pi}} - \frac{75\sqrt{\pi}}{16}) - 3Ab + \theta a A(\frac{48}{\sqrt{\pi}} - \frac{675\sqrt{\pi}}{32}), \tag{2.24}$$

$$a_t = -a^2\theta(\frac{16}{\sqrt{\pi}} - \frac{135\sqrt{\pi}}{16}) - \epsilon a^2(\frac{16}{3\sqrt{\pi}} - \frac{15\sqrt{\pi}}{8}) + ba, \tag{2.25}$$

$$b_t = -b^2 - k - \frac{20}{3a^4} - \frac{7gA^2\sqrt{\pi}}{2\sqrt{2}} + \frac{4\mu}{3a^2} + \frac{32}{3\sqrt{\pi}a^3} + \frac{135a^2\theta^2}{6}, \tag{2.26}$$

$$\theta_t = \frac{\sqrt{\pi}}{a^5} - \frac{3}{2a^4} + \frac{15gA^2\sqrt{\pi}}{32\sqrt{2}a} - \frac{135a\theta^2}{16} - 3\theta b - \frac{\mu\sqrt{\pi}}{2a^3}. \tag{2.27}$$

Equations 2.24-2.27 have been studied numerically in the linear and the nonlinear regime.

These studies reveal that the system undergoes spontaneous $\mathcal{PT}$ symmetric phase transition depending on the value of the strength of loss term (ϵ) in the

linear regime. For real potential, the particle number remains constant but the amplitude decreases and the width of the beam increases as the system evolves as shown in Figure 2.12(a). Figure 2.12(c) is plotted for low values of ϵ and the system behaves as in the case of real potential. This regime is known as unbroken $\mathcal{PT}$ symmetric regime. As ϵ increases the system undergoes spontaneous phase transition from unbroken to broken $\mathcal{PT}$ symmetric region. The particle number increases along with the amplitude and the width of the profile in the broken $\mathcal{PT}$ symmetric regime as plotted in Figure 2.12(e).

The system has been studied by varying the nonlinear coefficient, g. For the weak nonlinearity and low loss, the soliton evolution is stable. Figure 2.12(b) is plotted for the real potential $\epsilon = 0$ and $g = 0.1$. It is evident from the plot that as the width of the beam increases, the amplitude decreases and hence the particle number remains constant. As shown in Figure 2.12(d) the behavior is same as before in the unbroken $\mathcal{PT}$ symmetric regime. In the case of broken $\mathcal{PT}$ symmetric regime, the particle number, the amplitude and the width increase as shown in Figure 2.12(f). The soliton propagation is stable for low values of g and ϵ.

Equation 2.1 has been studied numerically using the finite difference method. The Hermite-Gaussian of order 1 is taken as the initial solution. The solution is stable in the linear regime for $\epsilon = 0$ as shown in Figure 2.13(a). Figure 2.13(c) is plotted for $\epsilon = 0.01$ and represents the unbroken $\mathcal{PT}$ symmetric regime in which the output profile remains constant. But the particle number is not a constant for broken $\mathcal{PT}$ symmetric regime and so the soliton collapses as shown in Figure 2.13(e) with $\epsilon = 2$. The stable solitons exist for the weak nonlinearity in the case of the real potential and low value of ϵ as shown in Figures 2.13(b) and 2.13(d) respectively. Figure 2.13(f) is plotted for the broken $\mathcal{PT}$ symmetric regime in which the soliton collapses as the system evolves. The variational results are in close agreement with the numerical results.

2.5 Conclusion

In this chapter, the single-hump and the double-hump solitons having $\mathcal{PT}$ symmetric complex potential in a medium with cubic nonlinearity have been studied using the numerical and the variational methods. We have studied the stationary states and the dynamical states in the linear and nonlinear regime. It is found that the strength of the complex part of the potential exhibits a threshold value above which the solution is unstable both for the single hump and the double hump solitons. Below the threshold value the system supports the solitons and it is known as $\mathcal{PT}$ symmetric regime. By tuning the nonlinearity and the strength of the real part of the potential it is possible to control the $\mathcal{PT}$ symmetric threshold value. The phase of the stationary states of the system exhibit spatial dependence for the complex potential. The solitons possess real and imaginary parts for conserving particle number in which the imaginary part contributes to gain or loss terms. The linear stability analysis predicts that in the presence of the complex potential, the solitons become oscillatory unstable. We found that the perturbation growth rate changes slightly with the imaginary potential for a given nonlinearity. The instability changes drastically with the strength of nonlinearity. For large values of the nonlinearity, the stationary modes are exponentially unstable. For the weak nonlinearity, the stable solitons exist both for fundamental mode (single-hump soliton) and the first excited state (the double-hump soliton).

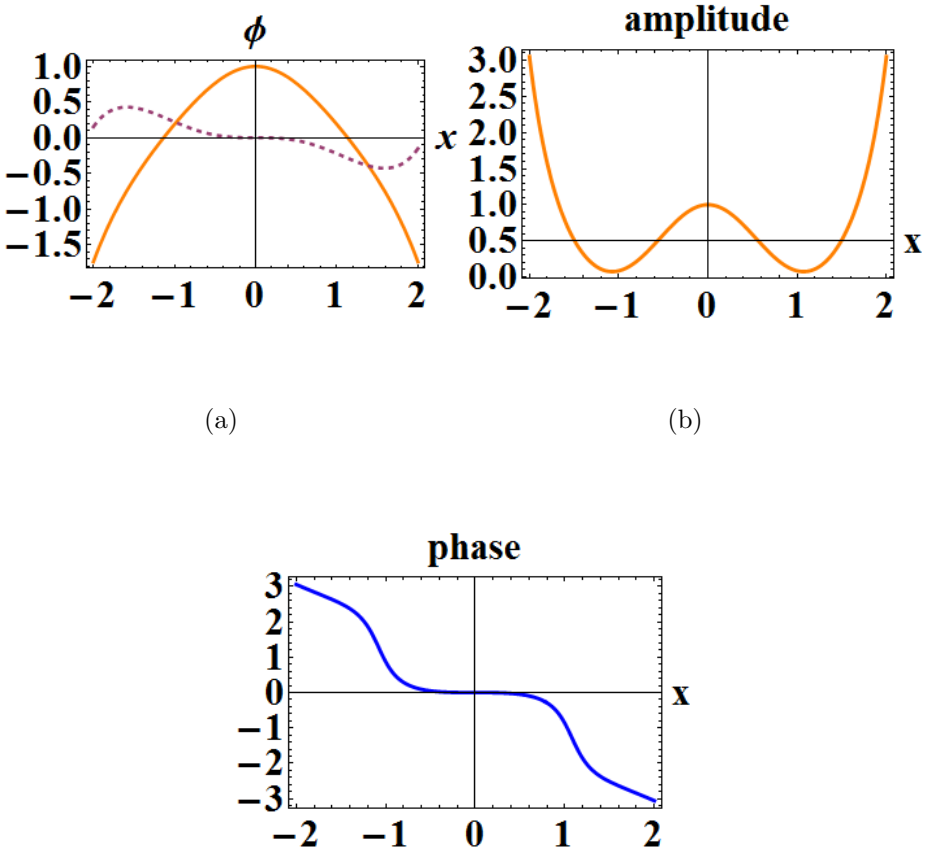

(a) (b)

(c)

Figure 2.2: The linear case. The complex potential in unbroken $\mathcal{PT}$ regime ($\epsilon = 0.01$). (a) The eigenstates, the real by orange and the imaginary by dotted purple, (b) the amplitude (particle density), and (c) the phase profile along the transverse direction.

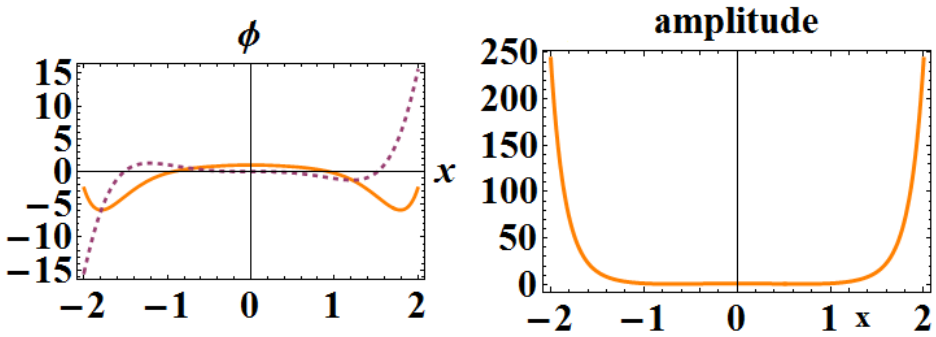

(a) (b)

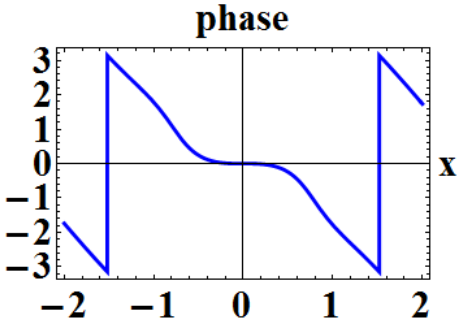

(c)

Figure 2.3: The linear case for broken $\mathcal{PT}$ regime ($\epsilon = 2$). (a) The eigenstates, the real by orange and the imaginary by dotted purple, (b) the amplitude (particle density), and (c) the phase profile along the transverse direction.

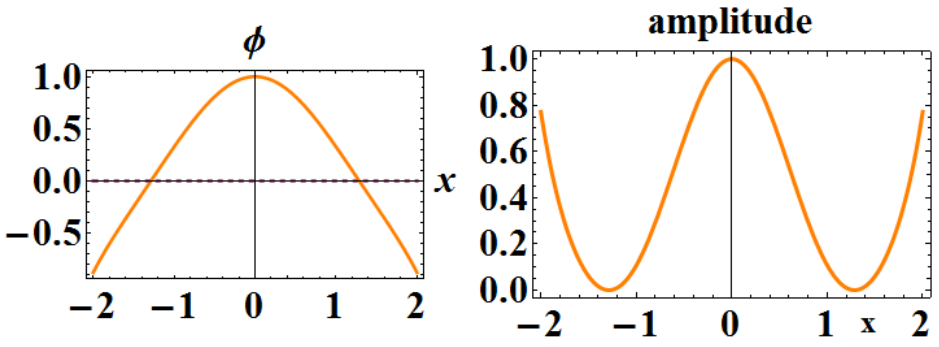

(a) (b)

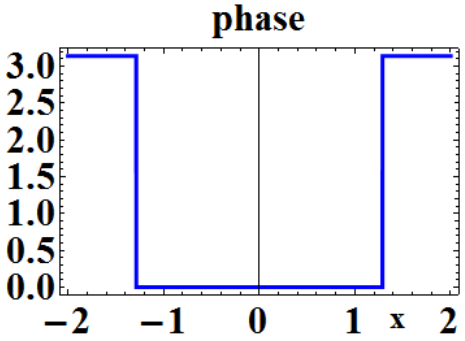

(c)

Figure 2.4: The nonlinear case ($g = 0.1$) for real potential ($\epsilon = 0$). (a) The eigenstates, the real by orange, the imaginary by dotted purple, (b) the amplitude (particle density), and (c) the phase profile along the transverse direction.

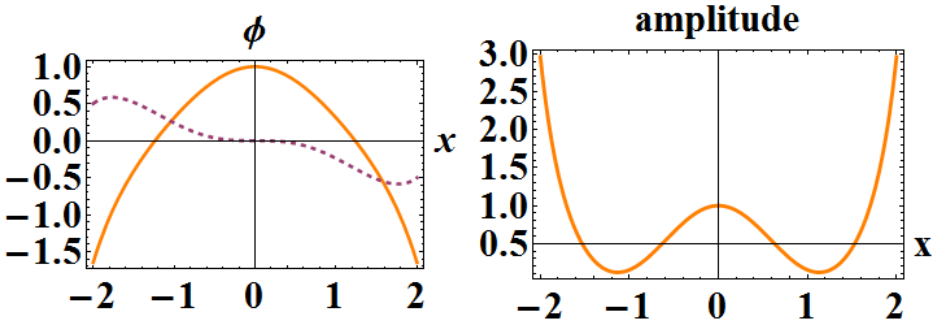

(a)

(b)

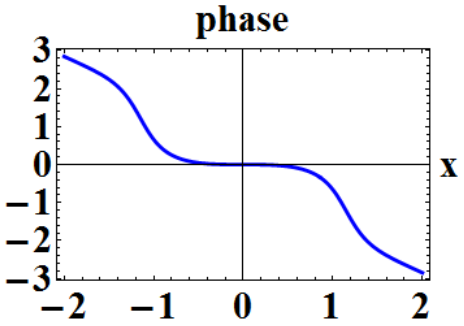

(c)

Figure 2.5: The nonlinear case ($g = 0.1$) for unbroken $\mathcal{PT}$ regime ($\epsilon = 0.01$). (a) The eigenstates, the real by orange and the imaginary by dotted purple versus x, (b) the amplitude (particle density versus x), (c) the phase profile as function of x.

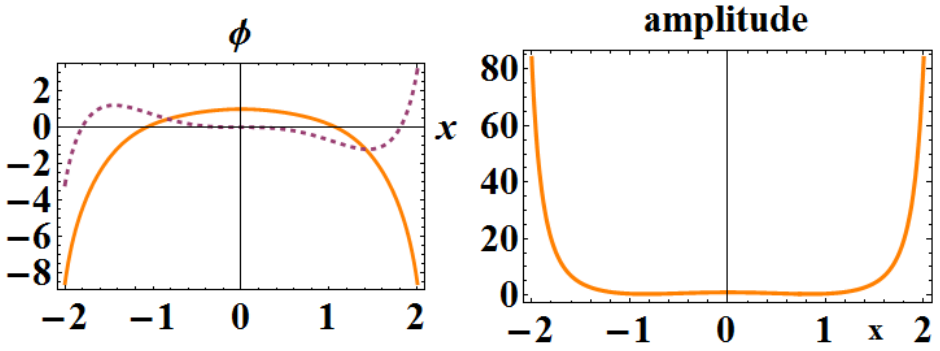

(a) (b)

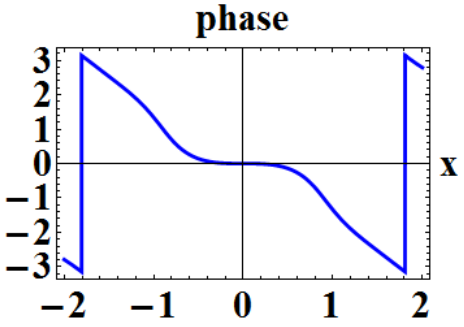

(c)

Figure 2.6: The broken $\mathcal{PT}$ regime ($\epsilon = 2$) (nonlinear case ($g = 0.1$)). (a) The eigenstates, the real by orange and the imaginary by dotted purple, (b) the amplitude (particle density), and (c) the phase profile as functions of x.

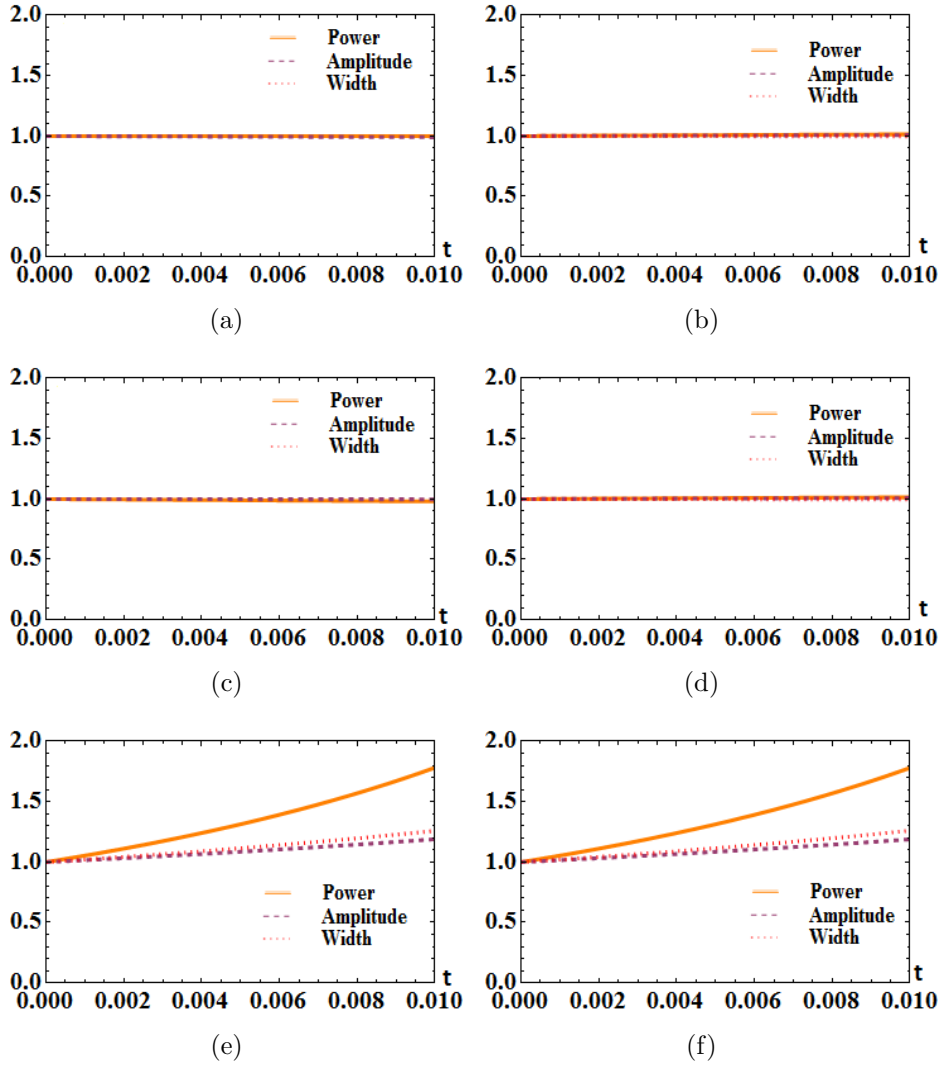

Figure 2.7: Linear (first column) and nonlinear (g = 0.1, second column) for fundamental mode. The amplitude (dashed purple), the width (dotted red) and the particle number or power (solid orange) as functions of z. First, second and third rows for the real potential ($\epsilon = 0$), the $\mathcal{PT}$ symmetric regime ($\epsilon = 0.01$) and the broken $\mathcal{PT}$ symmetric regime ($\epsilon = 2$) respectively.

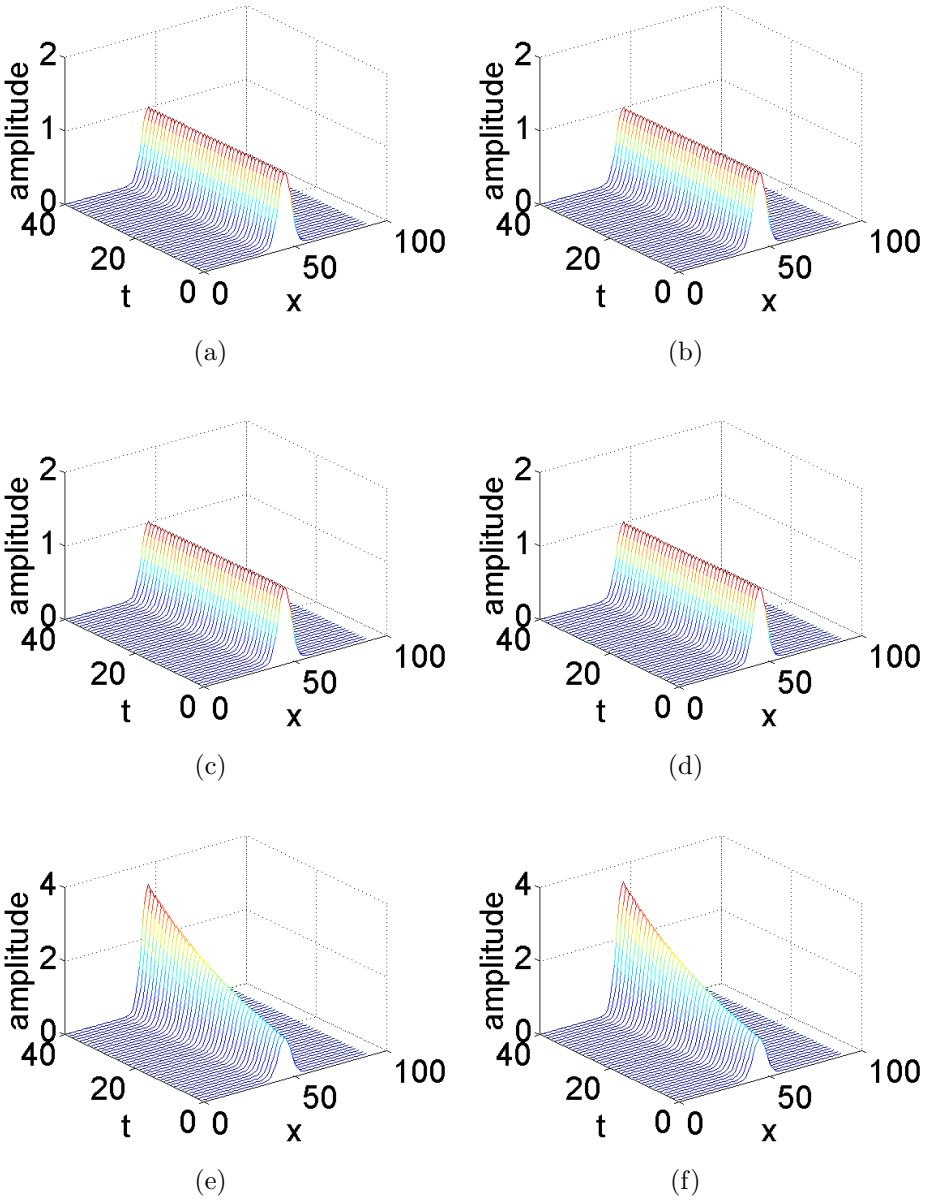

Figure 2.8: The Simulations for the dynamical states. Linear regime (first column) and nonlinear regime (second column with $g = 0.1$). First row for real potential ($\epsilon = 0$), second row for the $\mathcal{PT}$ symmetric regime ($\epsilon = 0.01$) and third row for broken $\mathcal{PT}$ symmetric regime ($\epsilon = 2$).

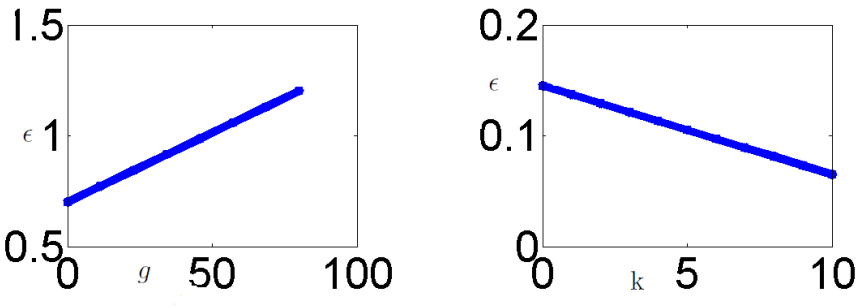

(a) (b)

Figure 2.9: The variation of the phase transition point ϵ_{th}. (a) ϵ_{th} versus g and (b) ϵ_{th} versus k.

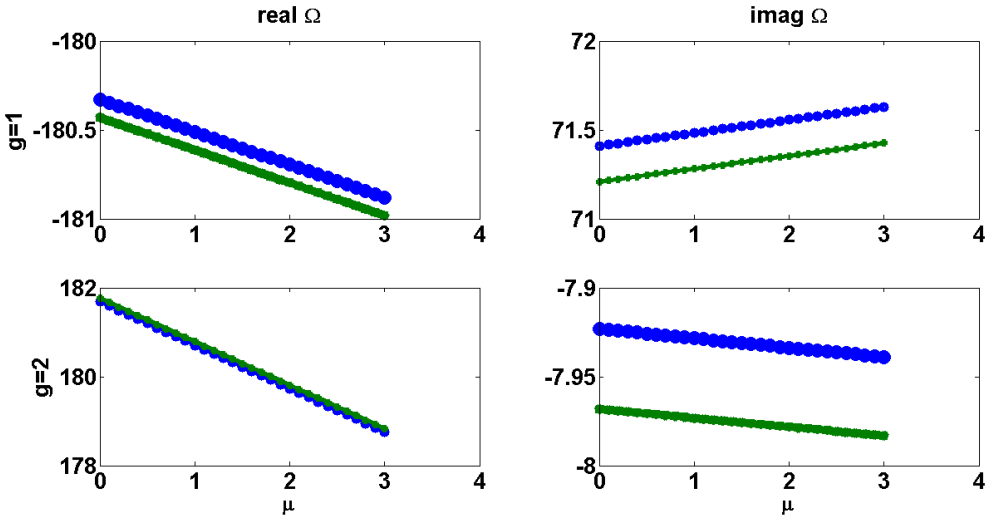

Figure 2.10: Real and imaginary parts of Ω vs μ in first and second column respectively, for $g = 1$ (first row) and $g = 2$ (second row). The imaginary potential ϵ is 0.1 (Blue o) and 2 (green *), respectively.

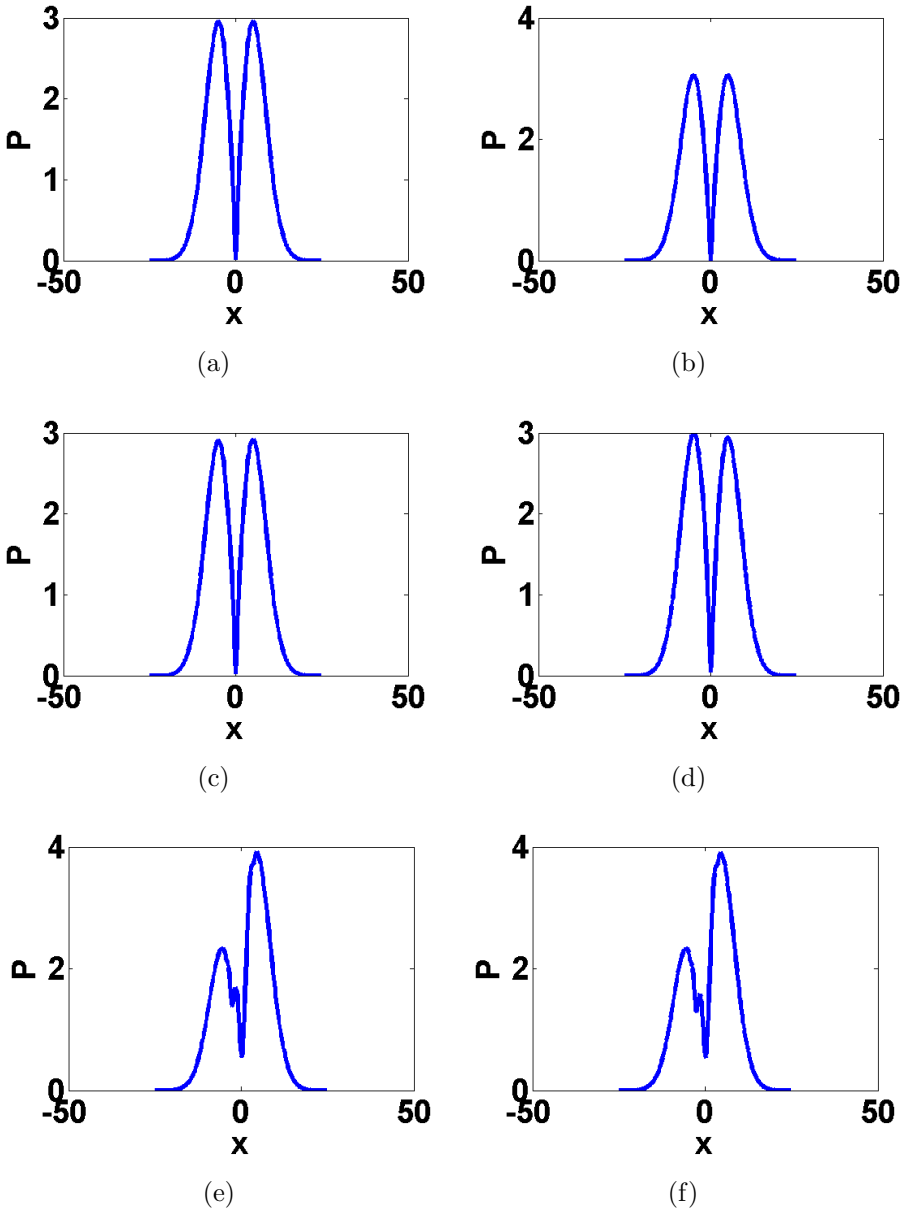

Figure 2.11: Linear (first column) and nonlinear ($g = 0.1$, second column) stationary states of higher eigenmode for $A = 1.02$, $a = 5$, $b = 1$, $\theta = 0.314$, $\mu = 1$ and $k = 1$. First row for the real potential ($\epsilon = 0$), second row for the unbroken $\mathcal{PT}$ symmetric regime ($\epsilon = 0.01$), and third row for the broken $\mathcal{PT}$ symmetric regime ($\epsilon = 2$).

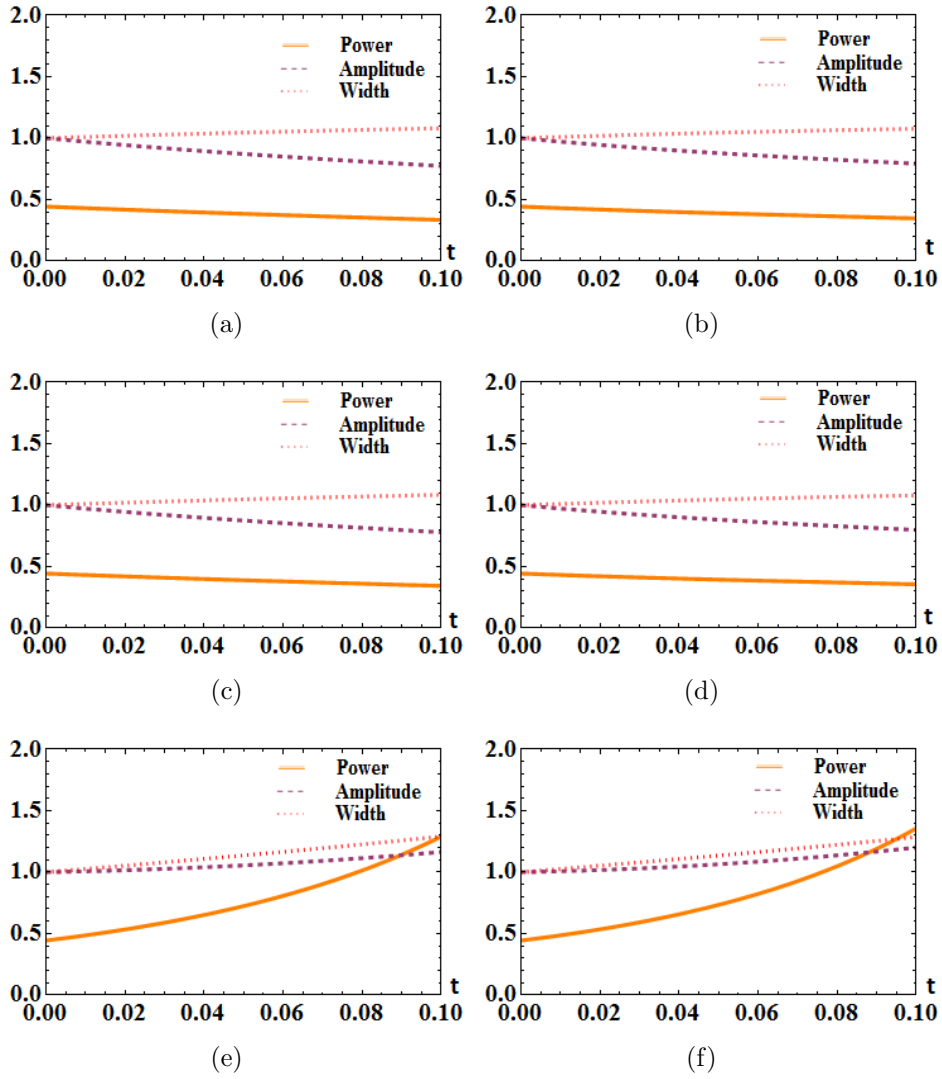

Figure 2.12: Linear (first column) and nonlinear ($g = 0.1$, second column). The particle number or power (solid orange), the amplitude (dashed purple) and the width (dotted red) as function of t. First, second, and third rows for the real potential ($\epsilon = 0$), the unbroken $\mathcal{PT}$ symmetric regime ($\epsilon = 0.01$), and the broken $\mathcal{PT}$ symmetric regime ($\epsilon = 2$) respectively.

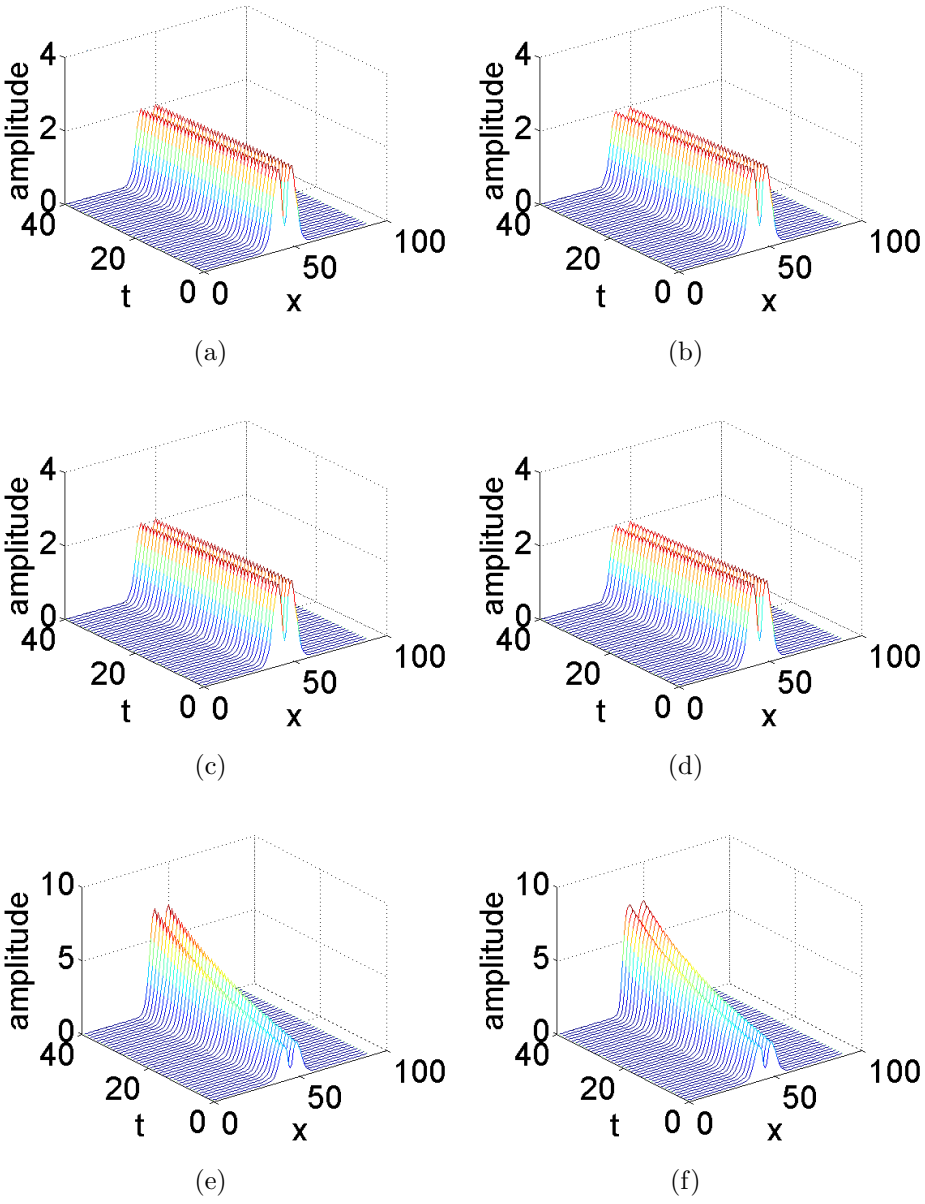

Figure 2.13: The evolution of the first exited state. First and second columns for linear and nonlinear regimes. First row for real potential ($\epsilon = 0$), second row for the unbroken $\mathcal{PT}$ symmetric regime ($\epsilon = 0.01$), and third row for the broken $\mathcal{PT}$ symmetric regime ($\epsilon = 2$).

Bibliography

[1] C.M.Bender and S.Boettcher. Real spectra in non-Hermitian Hamiltonians having $\mathcal{PT}$ symmetry. Phys. Rev. Lett. 1998; 80:5243-5246.

[2] M.P.Blencowe and H.Jones and A.P.Korte. Applying the linear δ expansion to the $i\phi^3$ interaction. Phys. Rev. D. 1998;57:5092.

[3] F.Cannata and G.Junker and J.Trost. Schrdinger operators with complex potential but real spectrum. Phys. Lett. A. 1998;246:219.

[4] Ali Mostafazadeh. PT-Symmetric Cubic Anharmonic Oscillator as a Physical Model. J.Phys.A. 2005;38:6557-6570.

[5] Z.H.Musslimani. Optical Solitons in PT Periodic Potentials. Phys. Rev. Lett. 2008;100:030402.

[6] Chao-Qing Dai and Yue-Yue Wang. A bright 2D spatial soliton in inhomogeneous Kerr media with PT-symmetric potentials. Laser Physics. Feb 2014;24(3).

[7] Zhenya Yan and Zichao Wen and Chao Hang. Spatial solitons and stability in self-focusing and defocusing Kerr nonlinear media with generalized PT-symmetric Scarff-II potentials. Phys. Rev. E. 2015;92:022913.

[8] Zhiwei Shi and Xiujuan Jiang and Xing Zhu and Huagang Li. Bright spatial solitons in defocusing Kerr media with PT -symmetric potentials. Phys. Rev. A 2011;84:053855.

[9] Yaroslav V Kartashov, Boris A Malomed, Lluis Torner. Unbreakable $\mathcal{PT}$ symmetry of solitons supported by inhomogeneous defocusing nonlinearity. Optics Letters. 2014; 39:5641-04.

[10] Makris KG, El-Ganainy R, Christodoulides DN. Beam Dynamics in $\mathcal{PT}$ Symmetric Optical Lattices. Phys. Rev. Lett. 2008; 100:103904(1-4).

[11] Yunji Meng,YouwenLiu. Solitons supported by defects of $\mathcal{PT}$-invariant potentials with realpart of dual-frequency lattices. Optics Communications. 2012; 285:4523-4530.

[12] Panayotis G Kevrekidis, Dmitry E Pelinovsky, Dmitry Y Tyugin. Nonlinear Stationary States in $\mathcal{PT}$-Symmetric Lattices. Siam J. Applied Dynamical System. 2013; 12:12101236.

[13] Sean Nixon, Lijuan Ge, Jianke Yang. Stability analysis for solitons in $\mathcal{PT}$ -symmetric optical lattices. Phys. Rev. A. 2012; 85:023822(1-10).

[14] T.P.Suneera and P.A.Subha. Single-hump and double-hump solitons in a $\mathcal{PT}$ symmetric complex potential. Waves in Random and Complex Media. 2016; 27:241-254.

[15] Chandroth P Jisha and Alessandro Alberucci and Valeriy A Brazhnyi and Gaetano Assanto. Nonlocal gap solitons in PT -symmetric periodic potentials with defocusing nonlinearity. Phys. Rev. A. 2014; 89:013812(1-10).

SUNEERA T. P. “STUDIES ON BEAM DYNAMICS IN SINGLE AND COUPLED PARITY-TIME SYMMETRIC SYSTEMS WITH KERR AND NONLOCAL NONLINEARITY”. THESIS. DEPARTMENT OF PHYSICS, UNIVERSITY OF CALICUT, 2018.

Chapter 3

Higher eigenmodes of $\mathcal{PT}$ symmetric nonlocal gap solitons

3.1 Introduction

The nonlocality of the nonlinear medium influences the behaviour of the beam dynamics. The nonlocal nonlinearity is important in optics too [1, 2, 3]. $\mathcal{PT}$ symmetric solitons in nonlocal nonlinear media have been investigated in various systems. Spatio-temporal localizations in (3 + 1)-dimensional $\mathcal{PT}$ symmetric and strongly nonlocal nonlinear media [4] and nonlocal multi-hump solitons in parity-time symmetric periodic potential [5] have been reported earlier.

Gap solitons are the localized solutions in the linear band gap of the system. These solitons exist in small length scales and find applications in all-optical switching and photonic logic gates. The bifurcation and stability of gap solitons have been reported [6]. These solitons has been analyzed in grating super structures [7]. Gap solitons have been investigated in $\mathcal{PT}$ symmetric systems such as in photo-refractive media [8], scattering by defects [9], and in superlattice and dual superlattice [10]. These solitons has been studied in dual-periodic $\mathcal{PT}$ symmetric optical lattices [11]. Gap solitons in linear defects and the nonlocal gap solitons in the defocusing media have been investigated [12, 13].

In this chapter we have discussed the higher eigenmodes of the nonlocal gap solitons having defocusing nonlinearity [14]. Section 3.2 briefly describes the double-hump nonlocal gap solitons in a medium with defocusing nonlinearity. The dynamical states have been studied in section 3.3. Section 3.4 and 3.5 discuss the linear stability analysis and conclusion respectively.

3.2 The first excited state

We consider Ψ as a generic field which represents the electromagnetic field and the distribution of the particle number in the case of light and the matter wave respectively. The medium under consideration is inhomogeneous with a defocusing nonlinearity and a nonlocal response. The complex potential which is experienced by the beam is periodic with a period π and $\mathcal{PT}$ symmetric. The governing equations are given by [13]:

$$i\frac{\partial\Psi}{\partial z} = \frac{-1}{2}\frac{\partial^2\Psi}{\partial x^2} + (V_R(x) - iV_I(x))\Psi + V_{NL}(|\Psi|^2)\Psi, \tag{3.1}$$

$$V_{NL} - \sigma\frac{\partial^2 V_{NL}}{\partial x^2} = |\Psi|^2, \tag{3.2}$$

where V_R, V_I and V_{NL} being the real part, the imaginary part and the nonlinear part of the potential respectively. x and z represent the transverse and the longitudinal coordinates. σ is the range or degree of nonlocality assumed as positive quantity and $\sigma = 0$ represents the Kerr nonlinearity. The complex periodic $\mathcal{PT}$ symmetric potential is given by $V_R(x) - iV_I(x) = V_r sin^2(x) - iV_i sin(2x)$. The power of the beam is obtained as:

$$P = \int_{-\infty}^{\infty} |\Psi|^2 \, dx. \tag{3.3}$$

The particle conservation of the system is expressed by the continuity equation [13]:

$$\nabla.j = -\frac{\partial\rho}{\partial t} + 2v_I(x)\rho, \tag{3.4}$$

in which $\rho = |\Psi|^2$, intensity and j is the particle flux:

$$j = \frac{1}{2i}(\Psi^* \frac{\partial \Psi}{\partial x} - \Psi \frac{\partial \Psi^*}{\partial x}).$$

The stationary state solutions have been studied by assuming:

$$\Psi(x, z) = \Phi(x) exp(-i\mu z), \tag{3.5}$$

μ being the propagation constant for light waves (the chemical potential in the case of the matter waves). Equations 3.1 and 3.2 take the new form:

$$\begin{aligned} \mu\Phi &= \frac{-1}{2}\frac{d^2\Phi}{dx^2} + (V_r Sin^2(x) - iV_i Sin(2x))\Phi + V_{NL}\Phi, \\ V_{NL} &- \sigma\frac{d^2 V_{NL}}{dx^2} = |\Phi|^2. \end{aligned} \tag{3.6}$$

3.2.1 The nonlinear eigenmodes

The first excited state of the steady-state equation 3.6 have been solved using Newton's Conjugate Gradient method (section 1.7.4). The trial solution is chosen as:

$$\Phi(x) = Ax^2 exp[\frac{-x^2}{w_b^2}], \tag{3.7}$$

where A and w_b are the amplitude and the width respectively. Equation 3.6 yields the double-hump eigenmodes for the real and the complex potentials.

The eigenmodes are plotted in Figures 3.1(a)-3.1(f) as functions of x. Figures 3.1(a) and 3.1(b) are plotted for the real potential (i.e. $V_i = 0$). Figure 3.1(a) shows the amplitude along x. From Figure 3.1(b), it is evident that the imaginary part of the solution is zero. The presence of the imaginary part of the potential results in the complex double-hump solutions whose amplitude is plotted in Figure 3.1(c). The real and the imaginary components of the eigenmodes versus x are shown in Figure 3.1(d). The behavior of the solution near the $\mathcal{PT}$ symmetric transition point has been studied. The amplitude with respect to x is

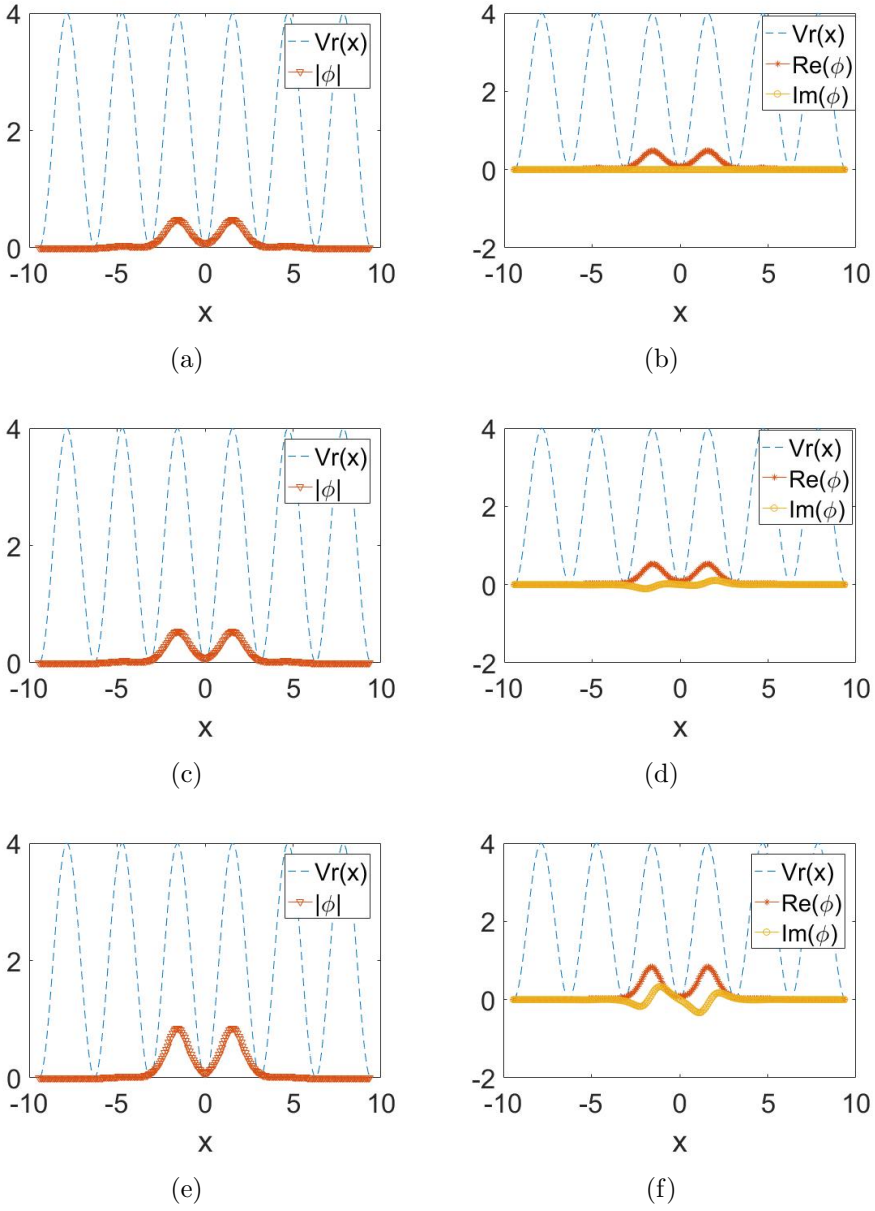

Figure 3.1: The double-hump gap solitons for $\sigma = 0.5$. First, second and third rows for $V_i = 0$, $V_i = 0.5$ and $V_i = 1.5$ respectively. First column for the intensity, second column shows the eigen state, the real part by red '*' and the imaginary part by yellow 'o'.

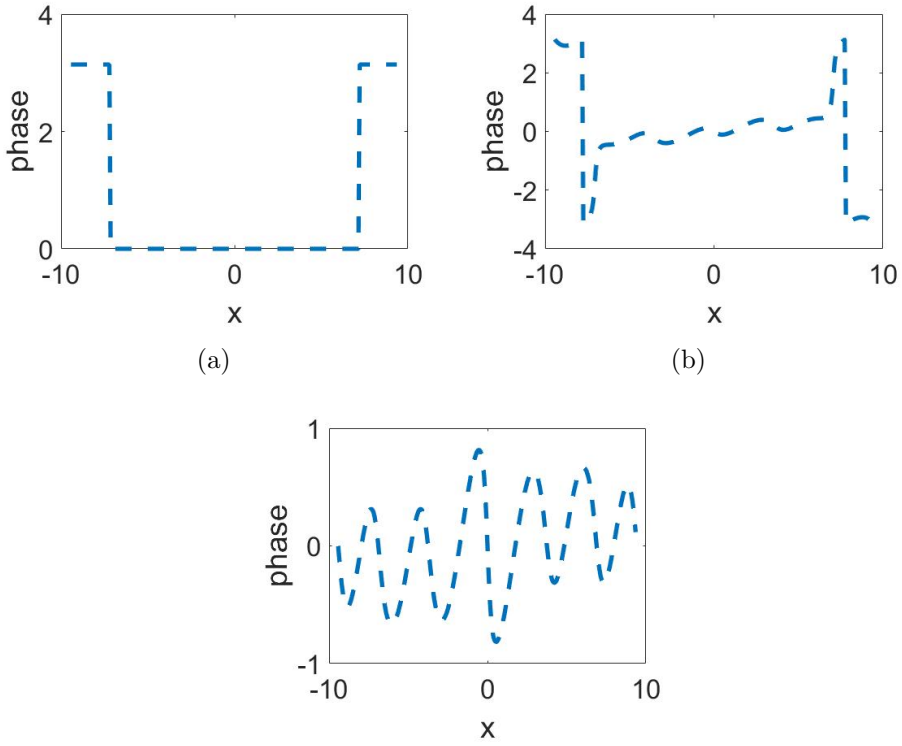

Figure 3.2: The phase profiles of the double-hump gap solitons for $\sigma = 0.5$. (a) $V_i = 0$, (b) $V_i = 0.5$, and (c) $V_i = 1.5$ respectively.

depicted in Figure 3.1(e). The real and the imaginary parts of the solution are shown in Figure 3.1(f). As the strength of the imaginary part of the potential increases, the imaginary component of the soliton also increases. Figure 3.2(a) shows that the phase profile is flat for the real potential. The presence of the imaginary part of the potential results in the spatial dependence of the phase as depicted in Figures 3.2(b) and 3.2(c) for the unbroken regime with far and near the phase transition point respectively.

The power carried by the double-hump soliton has been studied by treating the contributions from the real and the imaginary parts separately in addition to the total power. The total power P, the power carried by the real part P_r, and the imaginary part P_i of the higher eigenmode with the propagation constant μ have been plotted in Figures 3.3(a), 3.3(b), and 3.3(c) for different values of the range of the nonlocality. It is found that P, P_r and P_i increase with μ in the $\mathcal{PT}$

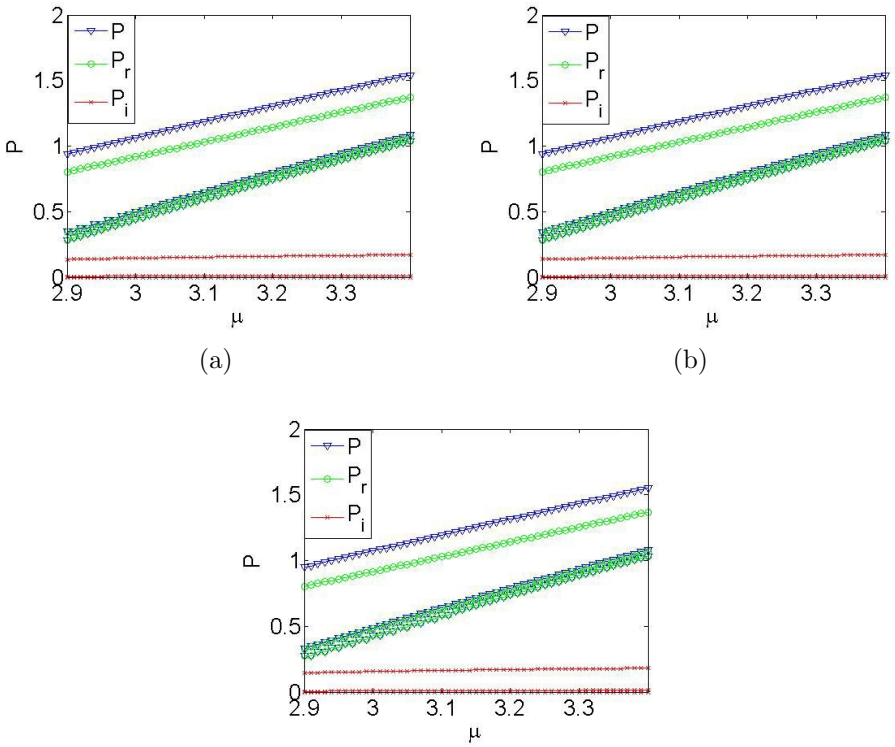

(a) (b)

(c)

Figure 3.3: Power versus propagation constant. (a), (b) and (c) for $\sigma = 0.5$, $\sigma = 1$ and $\sigma = 10$ respectively. In all figures $V_i = 0$, $V_i = 0.5$ and $V_i = 1.7$ from bottom to top.

symmetric regime. The power of the double-hump soliton increases with V_i for a given μ. As the propagation constant increases the power carried by the soliton also increases. Comparing Figures 3.3(a), 3.3(b), and 3.3(c), it is evident that the power of higher eigenmode is independent of the range of the nonlocality. It is found that the double-hump soliton exists only above a particular value of the propagation constant or energy which is 2.8 in this case.

3.3 The Dynamical states

The dynamics of the system has been investigated using the variational and the numerical method. Let $\Psi(x,z) = \Phi(x,z)exp(-i\mu z)$, and equations 3.1 and 3.2

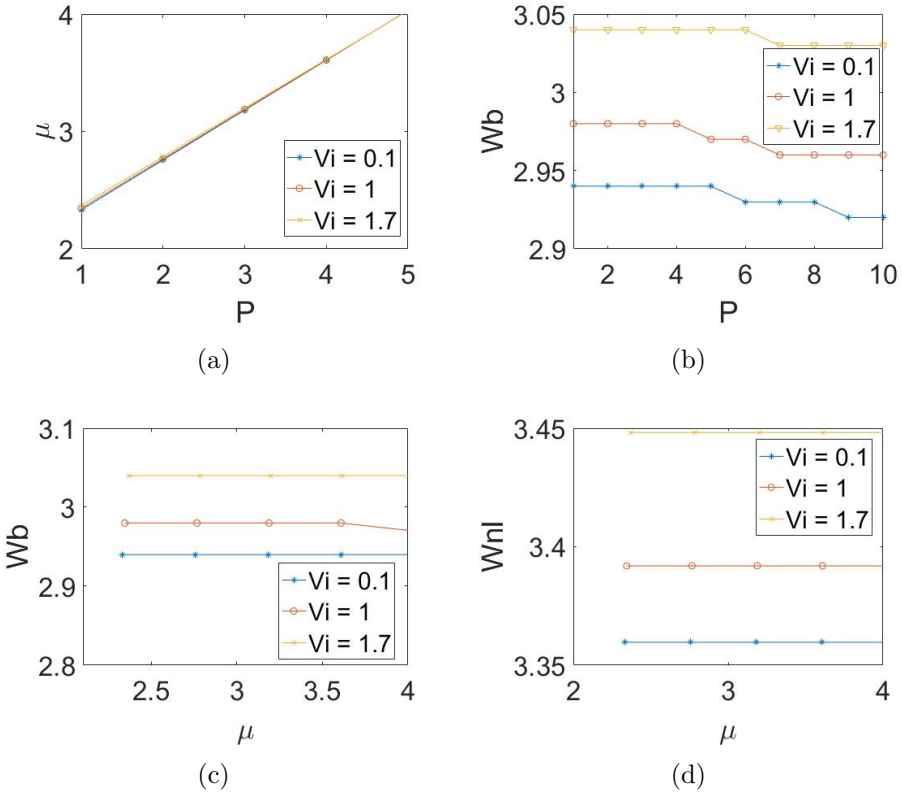

Figure 3.4: The variational results of the double-hump gap solitons for $\sigma = 1.0$ with different values of V_i. (a) P versus μ, (b) P versus Wb, (c) μ versus Wb, and (d) μ versus Wnl.

are rewritten as [13]:

$$\mu\Phi = -i\frac{\partial\Phi}{\partial z} + \frac{-1}{2}\frac{\partial^2\Phi}{\partial x^2} + (V_R(x) - iV_I(x))\Phi + V_{NL}(|\Phi|^2)\Phi,$$
$$V_{NL} - \sigma\frac{\partial^2 V_{NL}}{\partial x^2} = |\Phi|^2. \tag{3.8}$$

The Lagrangian density of the system is described by the following equation:

$$L = \frac{i}{2}(\Phi\Phi_z^* - \Phi^*\Phi_z) + \frac{1}{2} \mid \Phi_x \mid^2 + v(x) \mid \Phi \mid^2 + V_{NL} \mid \Phi \mid^2 - \mu \mid \Phi \mid^2$$
$$+\frac{\sigma}{2}(\frac{\partial V_{NL}}{\partial x})^2 - \frac{V_{NL}^2}{2}. \tag{3.9}$$

The Lagrangian density consists of conservative (L_C) and non-conservative (L_{NC}) components for dissipative systems. The imaginary part of the complex potential contributes in the non-conservative part of the Lagrangian. We have

assumed the ansatz:

$$\phi(x,z) = A(z)x^2 e^{\frac{-x^2}{W_b^2(z)}+if(x)\theta(z)}, \tag{3.10}$$

A(z), $w_b(z)$ and $\theta(z)$ being the amplitude, the width and the phase. The phase profile of the $\mathcal{PT}$ symmetric systems exhibit spatial dependence (f(x)) and here $f(x) = tanh(x)$ [13]. The reduced Lagrangian of the system is expressed as:

$$< L_C >= \int_{-\infty}^{\infty} L_c dx. \tag{3.11}$$

The equations of the standard variational approach to the dissipative systems are given by:

$$\frac{\partial}{\partial z}(\frac{\partial < L_C >}{\partial \eta_i}) - \frac{\partial < L_C >}{\partial \eta_i} = 2Re \int Q \frac{\partial \Phi^*}{\partial \eta_i} dx, \tag{3.12}$$

where $Q = \frac{\partial L_{NC}}{\partial \phi^*} - \frac{\partial}{\partial x}(\frac{\partial L_{NC}}{\partial \phi^*})$.
The effective Lagrangian of the system is obtained as:

$$\begin{aligned} < L_C >= -\mu P + \frac{7P}{6W_b^2} + \frac{V_r P}{2}[1 - \frac{(3 - 6W_b^2 + W_b^4)e^{\frac{-W_b^2}{2}}}{3}] \\ + \frac{10\sqrt{2}PA_{nl}W_{nl}^{11}W_b^2}{[2W_{nl}^2 + W_b^2]^{3.5}} - \frac{7\sqrt{\pi}\sigma A_{nl}^2 W_{nl}^3}{32\sqrt{2}} - \frac{3\sqrt{\pi}\sigma A_{nl}^2 W_{nl}^5}{32\sqrt{2}} \\ + \frac{8\sqrt{2}P}{3\sqrt{\pi}W_b^5}\theta^2 \int_{-\infty}^{\infty} f_x^2 e^{\frac{-2x^2}{W_b^2}} x^4 dx. \end{aligned} \tag{3.13}$$

The variational analysis provides a set of equations which is given by:

$$\theta = -\frac{2V_i \int_{-\infty}^{\infty} sin(2x) f(x) x^4 e^{-\frac{2x^2}{W_b^2}} dx}{\int_{-\infty}^{\infty} f_x^2 x^4 e^{-\frac{2x^2}{W_b^2}} dx}, \tag{3.14}$$

$$A_{nl} = \frac{320 W_{nl}^4 W_b^2 P}{\sqrt{\pi}(2W_{nl}^2 + W_b^2)^{3.5}(7\sigma + 3W_{nl}^2)}, \tag{3.15}$$

$$\begin{aligned} \mu = \frac{7}{6W_b^2} + \frac{8\sqrt{2}\theta^2}{3\sqrt{\pi}W_b^5} \int_{-\infty}^{\infty} f_x^2 x^4 e^{-\frac{2x^2}{w_b^2}} dx + \frac{V_r}{2} - \frac{V_r}{6} e^{-\frac{W_b^2}{2}}[3 - 6W_b^2 + W_b^4] \\ + \frac{6400\sqrt{2}W_{nl}^{11}W_b^4 P}{\sqrt{\pi}(2W_{nl}^2 + W_b^2)^7(7\sigma + 3W_{nl}^2)}, \end{aligned} \tag{3.16}$$

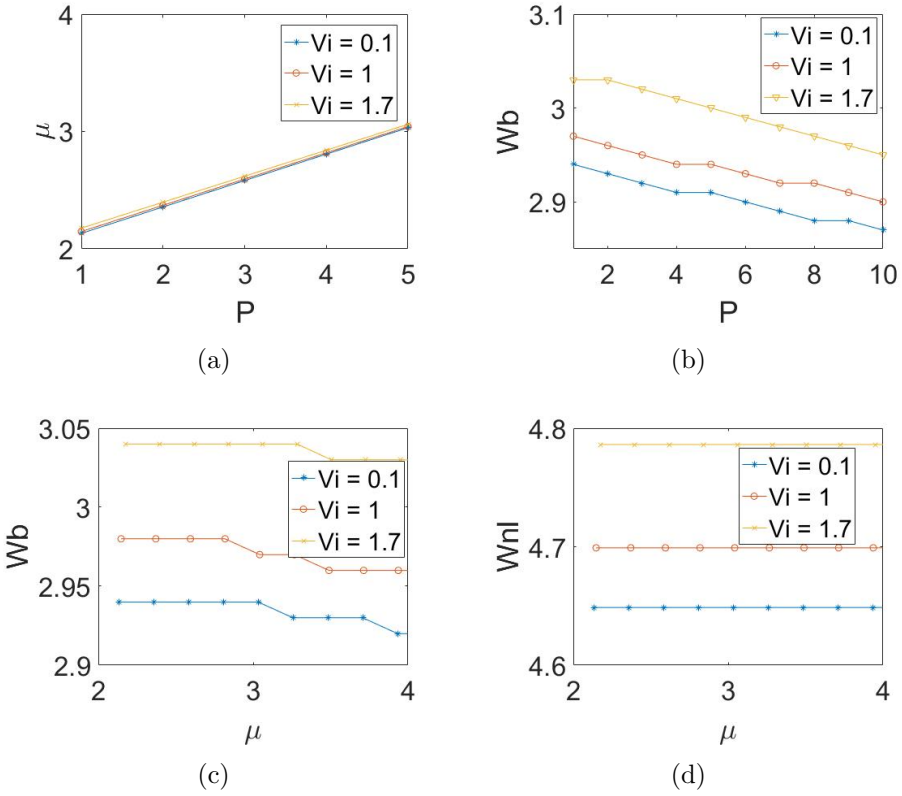

Figure 3.5: The variational results of the double-hump gap solitons for $\sigma = 10.0$ with different values of $V_i = 0.1$. (a) P versus μ, (b) P versus Wb, (c) μ versus Wb, and (d) μ versus Wnl.

$$W_{nl}^2 = \frac{[9W_b^2 - 14\sigma] + \sqrt{[9W_b^2 - 14\sigma + 9W_b^2]^2 + 3080\sigma W_b^2}}{20}, \tag{3.17}$$

$$\frac{7}{3w_b^3} = \frac{8\sqrt{2}\theta^2}{3\sqrt{\pi}}\frac{\partial}{\partial w_b}[\frac{1}{w_b^5}\int_{\infty}^{\infty} f_x^2 x^4 e^{-\frac{2x^2}{W_b^2}} dx] + \frac{V_r}{6}e^{-\frac{W_b^2}{2}}[15 - 10W_b^2 + W_b^4] + \frac{3200\sqrt{2}W_{nl}^{11}W_b^3 P[4W_{nl}^2 - 5W_b^2]}{\sqrt{\pi}(2W_{nl}^2 + W_b^2)^4(7\sigma + 3W_{nl}^2)}. \tag{3.18}$$

The variational equations 3.14-3.18 have been studied by varying V_i and σ. The double-hump gap solitons in the first band gap possess interesting features. These features are shown in the Figures 3.4 and 3.5. The power of the soliton with μ has been analysed and the plots are shown in Figures 3.4(a) and 3.5(a) for the weak and the strong nonlocality respectively. μ increases with P for any value of V_i. But μ corresponding to strong nonlocality is less than that of the weak nonlocality. The width of the soliton W_b versus P is shown in Figures

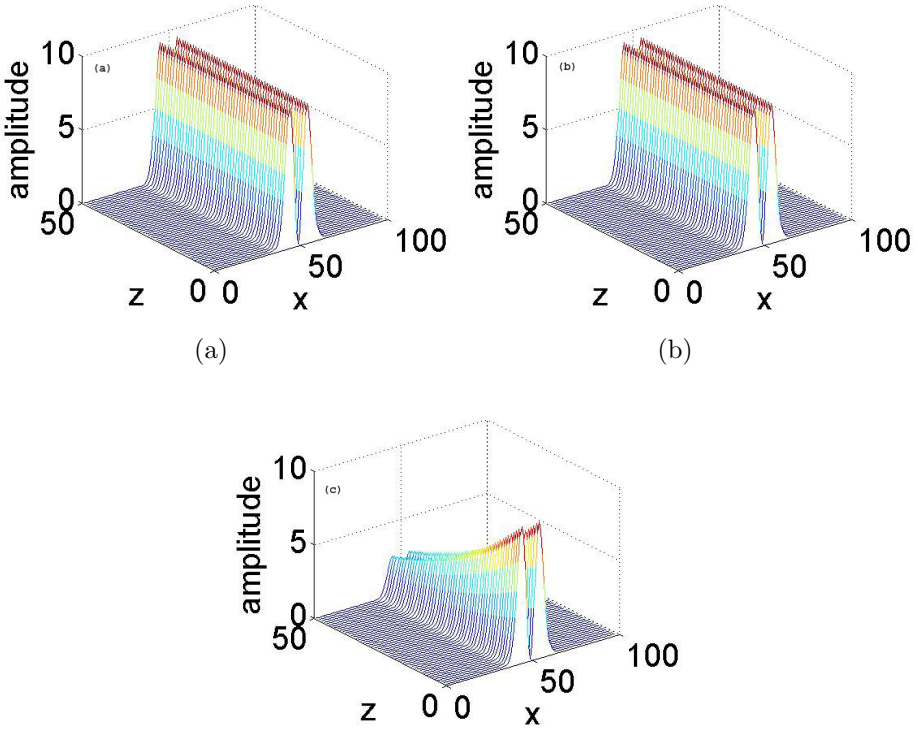

Figure 3.6: The simulation of the double-hump soliton. a) The real potential, b) the unbroken $\mathcal{PT}$ symmetric regime, and c) the broken $\mathcal{PT}$ symmetric regime.

3.4(b) and 3.5(b) for $\sigma = 1$ and $\sigma = 10$ respectively. W_b decreases with P and increases with V_i. The large range of the nonlocality results in decrease in the width of the soliton. W_b versus μ is plotted in Figures 3.4(c) and 3.5(c) for weak and strong nonlocality respectively. W_b is constant for lower values of μ and decreases for the values nearest to the band edge in the case of the weak nonlocality as depicted in Figure 3.4(c). When the range of the nonlocality is high (i.e, $\sigma = 10$), W_b decreases with μ as shown in Figure 3.5(c). From Figures 3.4(c) and 3.5(c), it is very clear that W_b increases with V_i. The width of the nonlocal potential W_{nl} with μ for various V_i are plotted in Figures 3.4(d) and 3.5(d) in the $\mathcal{PT}$ symmetric regime. W_{nl} is invariant with respect to μ for a given V_i. When V_i increases, W_{nl} also increases. From the Figures 3.4(d)-3.5(d), it is obvious that W_{nl} is greater for large σ.

The direct simulation of the system has been done using the finite difference

method. The evolution of the soliton has been plotted in Figure 3.4. The evolution of the soliton is stable for the real potential and the $\mathcal{PT}$ symmetric regime as shown in Figures 3.6(a) and 3.6(b) respectively. But the soliton dies out in the broken $\mathcal{PT}$ symmetric regime as is evident from Figure 3.6(c).

3.4 Linear Stability Analysis

The linear stability analysis has been done using the Bogoliubov-De Genes (BDG) equation. Consider the small perturbations of the form [13]:

$$\Psi(x,z) = (\phi(x) + p(x)e^{i\lambda z} + q(x)e^{-i\lambda^* z})e^{i\mu z}, \tag{3.19}$$

where $p(x)$ and $q(x)$ are the amplitudes of perturbation with eigenvalue λ. Substituting for $\Psi(x,z)$ in equations 3.1 and 3.2, and neglecting higher powers of $p(x)$ and $q(x)$, the linearized BDG equations are obtained as:

$$\begin{aligned}
\lambda_g p &= [L + iV_i(x)]p - \Phi D(\Phi^* p + q^* \Phi), \\
\lambda_g q^* &= [-L + iV_i(x)]q^* + \Phi^* D(\Phi^* p + q^* \Phi),
\end{aligned} \tag{3.20}$$

being $L = \mu + \frac{1}{2}\frac{\partial^2}{\partial x^2} - V_r(x) - V_{NL}^{\mu}(x)$ and $D = (1 - \sigma\frac{\partial^2}{\partial x^2})^{-1}$.

The solution is stable if the imaginary part of the eigenvalue $Im(\lambda)$ is zero. The complex eigenvalues represent unstable solution. The perturbation modes increase exponentially for the negative values of $Im(\lambda)$ and decrease exponentially for the positive values of $Im(\lambda)$.

The pertubation modes decay exponentially along with the oscillatory instability if the nonlocality is weak, as shown in Figure 3.7(a). However the perturbation modes grow exponentially with oscillatory instability in the case of strong nonlocality as depicted in 3.7(b). This is true for the unbroken $\mathcal{PT}$ symmetric regime as depicted in Figures 3.7(c) and 3.7(d) for weak and strong nonlocality respectively. Figures 3.7(e) and 3.7(f) illustrate that the double-hump modes are unstable in the broken regime whether the nonlocality is weak or strong.

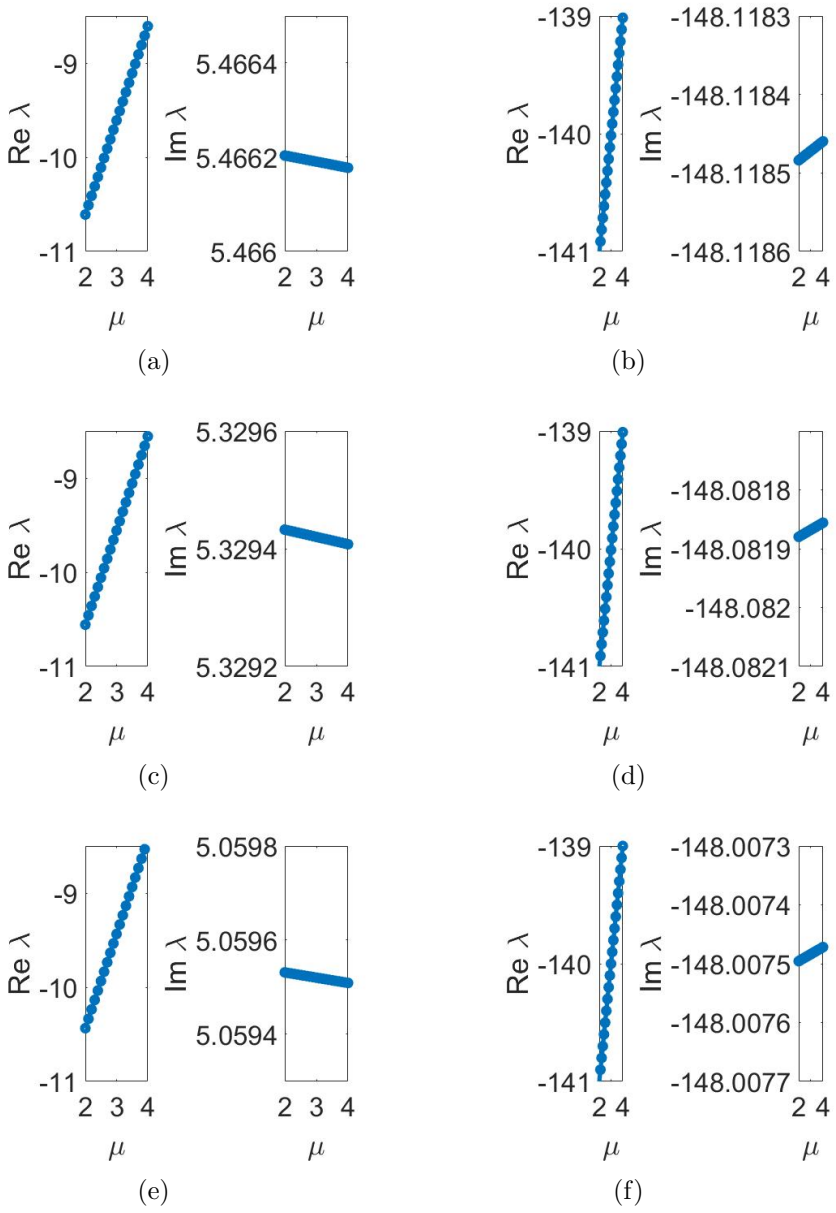

Figure 3.7: The linear stability analysis. First column for $\sigma = 0.5$ and the second column for $\sigma = 8$. First, second and third rows for the real potential, the unbroken $\mathcal{PT}$ symmetric regime, and the broken $\mathcal{PT}$ symmetric regime.

3.5 Conclusion

The beam dynamics of the double-hump gap solitons in a $\mathcal{PT}$ symmetric complex potential in a medium having defocusing nonlocal nonlinearity have been studied. The double-hump solitons have symmetric real part and the antisymmetric imaginary part for the particle conservation. Higher eigenmodes exist above a critical value of the propagation constant and preserve its shape irrespective of the range of the nonlocality. The power of these solitons increase with the propagation constant and it is independent of the range of the nonlocality. The dynamical states have been analyzed. It was found that the power of the soliton increases with the propagation constant and decreases with the range of the nonlocality. The width of the soliton decreases with the propagation constant, the power and the range of the nonlocality. The width of the nonlocal potential remains same with the propagation constant and increases with the range of the nonlocality. The direct simulation of the system reveals the existence of the double-hump solitons in the $\mathcal{PT}$ symmetric regime and it dies out in the broken $\mathcal{PT}$ symmetric regime. The linear stability analysis has been done and found that the double-hump soliton is unstable. The perturbation modes are exponentially decaying for low ranges of the nonlocality and exponentially growing for high ranges of the nonlocality. These studies have been extended to the coupled systems.

Bibliography

[1] D.John Mitchell and Allan W.Snyder. Soliton dynamics in a nonlocal medium. J.Opt.Soc.Am.B. 1999;16:2 236-239.

[2] Yaroslav V. Kartashov and Lluis Torner. Gray spatial solitons in nonlocal nonlinear media. Optics Letters. 2007;32:8 946-948.

[3] A.Alberucci and C.P.Jisha and N.F.Smyth and G.Assanto. Spatial optical solitons in highly nonlocal media. Phys Rev A 2015;91(1):013841.

[4] C.Q.Dai and Y.Y.Wang. Spatiotemporal localizations in (3+1)-dimensional $\mathcal{PT}$-symmetric and strongly nonlocal nonlinear media. Nonlinear Dyn 2016;83:24539.

[5] Xing Zhu and Huagang Li and Hong Wang and Yingji He. Nonlocal multihump solitons in parity-time symmetric periodic potentials. J. Opt. Soc. Am. B. 2013;30(7):198795.

[6] Dmitry E.Pelinovsky and Andrey A.Sukhorukov and Yuri S.Kivshar. Bifurcations and stability of gap solitons in periodic potentials. Phys. Rev. E. 2004;70:036618(1-17).

[7] Thawatchai Mayteevarunyoo and Boris A. Malomed. Gap solitons in grating superstructures. Optics Express 2008;16:11 (7767-7777).

[8] Woo-PyoHong and Young-DaeJung. Gap solitons in photorefractive medium with PT-symmetric optical lattices. Phys. Lett. A. 2015;379:7 (676-679).

[9] F.Kh.Abdullaev and V.A.Brazhnyi and M.Salerno. Scattering of gap solitons by PT-symmetric defects. Phys. Rev. A. 2013; 88:043829.

[10] Zhen Li and Shuang Shi and Xiao-Ping Ren and Hong Wang. Multi-peak gap solitons in PT-symmetric optical lattice in the form of superlattice and dual superlattice. J. Nonlinear Optic. Phys. Mat. 2015;24:1550024.

[11] Huagang Li and Xiujuan Jiang and Xing Zhu and Zhiwei Shi. Nonlocal solitons in dual-periodic $\mathcal{PT}$-symmetric optical lattices. Phys. Rev. A. 2012;86:023840.

[12] Sumei Hu and Daquan Lu and Xuekai Ma and Qi Guo and Wei Hu. Defect solitons supported by nonlocal PT symmetric superlattices. Eur. Phys. Lett. 2012;98:1.

[13] Chandroth P Jisha and Alessandro Alberucci and Valeriy A Brazhnyi and Gaetano Assanto. Nonlocal gap solitons in $\mathcal{PT}$-symmetric periodic potentials with defocusing nonlinearity. Phys. Rev. A. 2014;89:013812 (110).

[14] T.P.Suneera and P.A.Subha. Higher eigenmodes of nonlocal gap solitons in parity-time symmetric complex potential with a defocusing nonlinearity. Chaos, Solitons and Fractals. 2017;98:183-188.

SUNEERA T. P. “STUDIES ON BEAM DYNAMICS IN SINGLE AND COUPLED PARITY-TIME SYMMETRIC SYSTEMS WITH KERR AND NONLOCAL NONLINEARITY”. THESIS. DEPARTMENT OF PHYSICS, UNIVERSITY OF CALICUT, 2018.

Chapter 4

Beam dynamics in $\mathcal{PT}$ symmetric coupled systems with Kerr nonlinearity

4.1 Introduction

The realisation of integrated photonic devices, require basic elements of photonic circuitry such as couplers, diodes, switches, and isolators [1]. Two closely spaced parallel single mode channels with an intensity dependent refractive index is known as the directional coupler [2]. The beam dynamics in coupled systems are described by coupled nonlinear Schrödinger equation (CNLSE) and studied theoretically in 1992 [3]. The nonlinear coupler has been studied as a basic photonic element which permits intensity-dependent energy transport [4, 5].

The presence of the gain/loss in $\mathcal{PT}$ symmetric systems yield complex dynamics and improve its functionality. The coupler with gain of one channel is exactly compensated by the loss of the other channel, constitutes a $\mathcal{PT}$ symmetric coupler [6]. They render unidirectional dynamics suitable for an optical diode. The dynamical properties of these systems are characterised by the relation between the coefficients of the coupling (C) and gain/loss (G) which divides

the system parameters into two domains corresponding to the broken and unbroken regimes. These systems exhibit diverse phenomena including bright solitons [7, 8, 9, 10] and dark solitons [11], breathers [12] and rogue waves [13]. Recently, the phase transition in multimode nonlinear parity-time symmetric waveguide couplers [14], the stable nonlinear super modes and direct transport in asymmetric couplers [15] have been demonstrated. The parity-time symmetry breaking in coupled nano-beam cavities has been reported [16]. It was reported that dual laser cavities having saturable nonlinearity supports solitons and vortices [6, 17]. The $\mathcal{PT}$ symmetry can be achieved in these systems by constructing both the cores with doped lossy material while external pumping of the dopant atoms produce linear gain in the system [18]. The integrability of the $\mathcal{PT}$ symmetric dimer was studied [19] and solitons were predicted in a chain of parity-time invariant dimers [20]. The blow up regimes in the $\mathcal{PT}$ symmetric coupler and the actively coupled dimer was analyzed [21]. An exactly solvable $\mathcal{PT}$ symmetric dimer from a Hamiltonian system of nonlinear oscillators with gain and loss was reported [22].

The periodic nature of refractive index leads to formation of transmission bands and photonic band gaps. These properties are utilised to create high reflectivity, high dispersion and frequency filtering characteristics [23]. One example is index gratings either embedded in optical fibers or in bulk [24, 25, 26]. We can create periodic potentials in Bose-Einstein Condensate (BEC) using optical lattices (OL) and through the transverse modulation of refractive index in Photonic crystals [27].

This chapter discusses the $\mathcal{PT}$ symmetric coupled system with transverse periodic and aperiodic potentials in Kerr media [28]. The model of $\mathcal{PT}$ symmetric coupled system has been introduced. The system has been analyzed in linear regime. The studies are extended to the propagation dynamics and for the linear stability analysis.

4.2 The Model

The electromagnetic fields in the two channels of a coupled system are represented by Ψ_1 and Ψ_2 and they are coupled by the tunnelling of light between the two cores. The $\mathcal{PT}$ symmetric coupled system in a transverse potential with Kerr nonlinearity is modelled by a set of normalized coupled one dimensional Nonlinear Schrödinger Equations [8]:

$$i\frac{\partial\Psi_1}{\partial z} + \frac{\partial^2\Psi_1}{\partial x^2} + V_R(x)\Psi_1 + \beta\left|\Psi_1\right|^2\Psi_1 + iG\Psi_1 + C\Psi_2 = 0, \tag{4.1}$$

$$i\frac{\partial\Psi_2}{\partial z} + \frac{\partial^2\Psi_2}{\partial x^2} + V_R(x)\Psi_2 + \beta\left|\Psi_2\right|^2\Psi_2 - iG\Psi_2 + C\Psi_1 = 0, \tag{4.2}$$

where $V_R(x)$ be the transverse real potential, β be the strength of the nonlinearity, C and G be the coupling and the gain/loss coefficients respectively. z is the scaled propagation distance whereas x is the transverse spatial coordinate. The system is $\mathcal{PT}$ symmetric if the gain of the first channel is compensated by an equal amount of loss of the second channel.

We focus on two types of the potential profiles of the form:

$$V_R(x) = V_r sin^2(x), \tag{4.3}$$

$$V_R(x) = V_0 x^2, \tag{4.4}$$

in which equation 4.3 is the periodic potential with period π of strength V_r and equation 4.4 is the aperiodic potential of strength V_0.

The propagation invariant solutions $U(x)$ of the system has been studied to understand the effect of the transverse potential. The solution $U(x)$ is related with the fields Ψ_1 and Ψ_2 as follows:

$$\Psi_1(x,z) = U(x)e^{-i(\mu z-\theta_1)}, \tag{4.5}$$

$$\Psi_2(x,z) = U(x)e^{-i(\mu z-\theta_2)}, \tag{4.6}$$

where μ be the propagation constant and θ_1 and θ_2 are the phases of the solutions in channel 1 and 2 respectively. Substituting the equations 4.5 and 4.6 in the

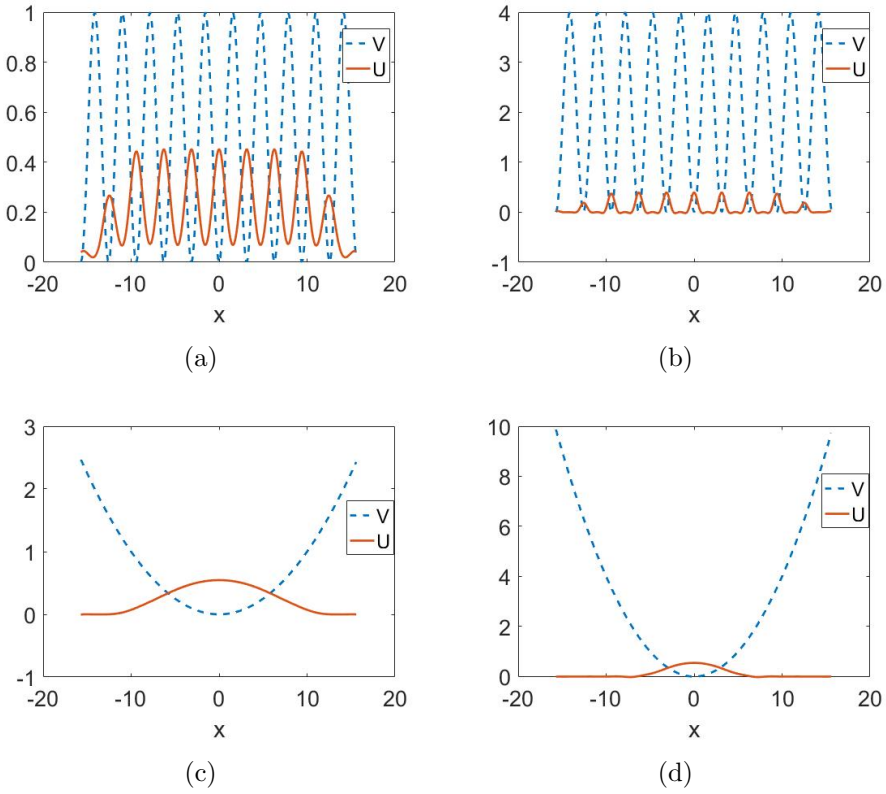

Figure 4.1: High-frequency modes (solid red) of the system for $C = 1$, $\beta = 1$ and $G = 0.5$. First row for periodic potential (dashed blue): (a) $V_r = 1$, and (b) $V_r = 4$. Second row for aperiodic potential (dashed blue): (c) $V_0 = 0.01$, and (d) $V_0 = 0.04$.

model equations 4.1 and 4.2 and after simplification, the governing equations of the system is obtained as:

$$\frac{d^2U}{dx^2} + V_R(x)U + C_{th}U + \beta|U|^2U - \mu U = 0, \tag{4.7}$$

where $C_{th} = Ccos(\delta) = \sqrt{C^2 - G^2}$, and $\delta = \theta_1 - \theta_2$.

Either $cos(\delta) > 0$ which denotes the high-frequency mode, U_+ or $cos(\delta) < 0$ which denotes the low-frequency mode, U_-. Two families persist only for $G < C$. The high-frequency and the low-frequency modes are studied by using Newton Conjugate Gradient (NCG) method.

The high-frequency modes have been studied in the case of transverse periodic potential. The results are shown in Figures 4.1(a) and 4.1(b). The high-frequency

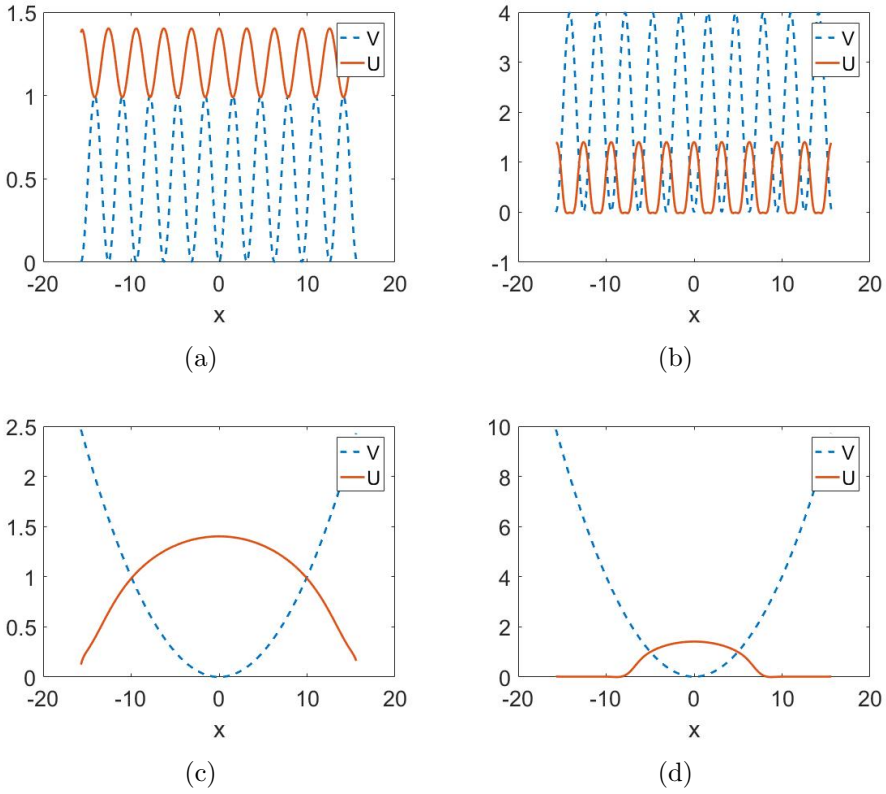

Figure 4.2: Low-frequency modes (solid red) of the system for $C = 1$, $\beta = 1$ and $G = 0.5$. First row for periodic potential (dashed blue): (a) $V_r = 1$, and (b) $V_r = 4$. Second row for aperiodic potential (dashed blue): (c) $V_0 = 0.01$, and (d) $V_0 = 0.04$.

mode resides in each lattice site around the minimum of the potential as shown in Figure 4.1(a). As the strength of the potential V_r increases, the mode is tightly confined in the site as depicted in Figure 4.1(b).

The system is studied with the transverse potential of the form $V_R(x) = V_0 x^2$. The high-frequency modes exists only in the minimum of the potential. From Figure 4.1(c), it is evident that the center of the modes lies at the minimum of the potential. As the depth of the potential increases, these modes confined in the site as is plotted in Figure 4.1(d).

The low-frequency modes are studied and plotted in Figures 4.2(a)-4.2(d). Increasing V_r, more tightly confine the low-frequency modes to the lattice in the case of the periodic potential as depicted in Figures 4.2(a) and 4.2(b). These modes get trapped in the minimum of the aperiodic potential as shown in Figures

4.2(c) and 4.2(d). Figures 4.1 and 4.2 reveal that the amplitudes of the low-frequency modes are slightly greater than that of the high-frequency modes.

4.3 The linear regime

The linearised version of the system is described by equation 4.7 with $\beta = 0$ and is given by:

$$\frac{d^2U}{dx^2} + V_R(x)U + C_{th}U - \mu U = 0, \tag{4.8}$$
$$C_{th} = \sqrt{C^2 - G^2}.$$

Case 1: The periodic potential

Since the potential is periodic, the system supports Bloch waves of the form $U(x) = U_K(x)e^{iKx}$ in equation 4.8, where K represents the Bloch momentum with the periodicity condition $U_K(x + \pi) = U_K(x)$. The Bloch solutions satisfy the equation:

$$\frac{d^2U_K}{dx^2} + 2iK\frac{dU_K}{dx} + (V_R(x) - K^2)U_K + C_{th}U_K = \mu U_K. \tag{4.9}$$

Employing the spectral method based on Chebyshev polynomials, the eigenvalues of the system is calculated and determined the $\mathcal{PT}$ symmetric regime. The eigenvalues are computed for Bloch momentum K for various values of the gain/loss coefficient (G) keeping the strength of the periodic potential and the coupling coefficient, unity.

The first two linear bands, formed by the real part of the eigenvalues ($Re(\mu)$) are shown in Figures 4.3(a) and 4.3(b). Figure 4.3(a) shows the band formation of $Re(\mu)$ for the coupler with $G = 0$. The presence of G lifts certain eigenvalues of the second band as shown in Figure 4.3(b). As far as $G < C$, the $Im(\mu)$ is negligibly small indicating the unbroken $\mathcal{PT}$ symmetric regime. When G exceeds C, all the eigenvalues of the second band shift to low values (bottom of blue band) and the new band appears as illustrated in Figure 4.3(c) and

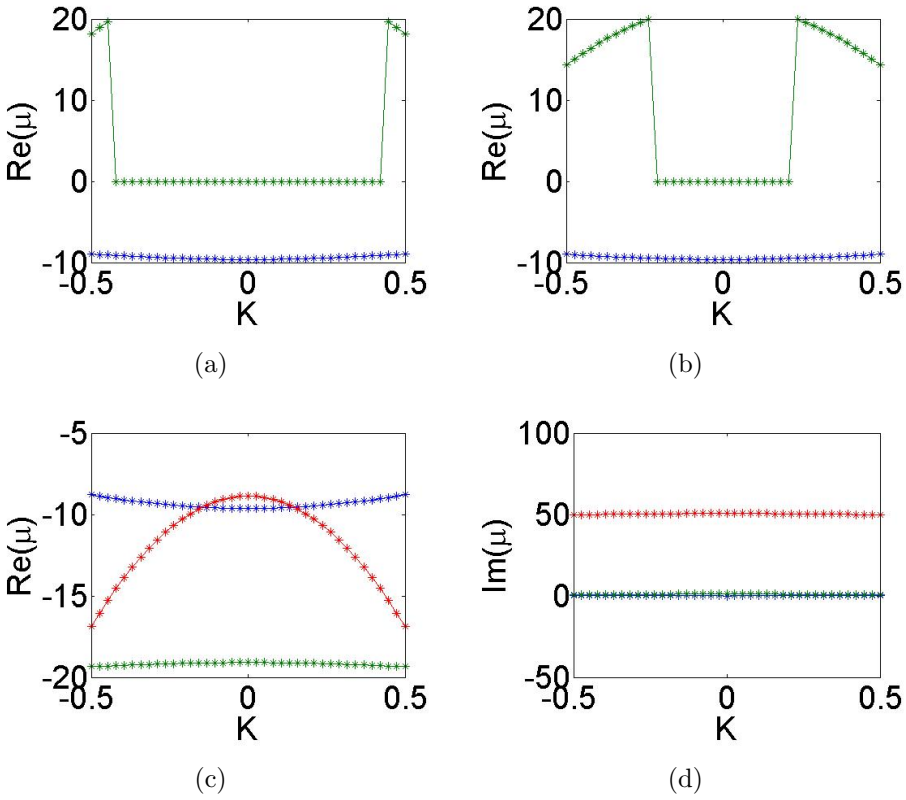

Figure 4.3: The linear coupler ($\beta = 0$) with $C = 1$ and $V_r = 1$. (a) and (b) for real part of the eigenvalues versus the Bloch momentum in which the first band in blue and the second band in green respectively for $G = 0.0$ and $G = 0.5$. (c) and (d) are the real and the imaginary parts of the eigenvalues versus Bloch momentum respectively for $G = 2.0$.

$Im(\mu)$ becomes large as shown in Figure 4.3(d) which is the broken regime. The effect of the transverse periodic potential on the intensity of the beam has been studied numerically. The amplitude of the beam in the absence of the transverse potential is shown in Figure 4.4(a). The presence of the transverse periodic potential modulates the amplitude as depicted in Figures 4.4(b) and 4.4(c).

Case 2: The aperiodic potential

The linear coupler which is governed by equation 4.8 with $V_R(x) = V_0 x^2$, has been studied using spectral method based on Chebyshev polynomials.

The eigenvalues of the coupler in the absence of the gain/loss coefficient are plotted in Figure 4.5(a). The eigenvalues are purely real as expected because

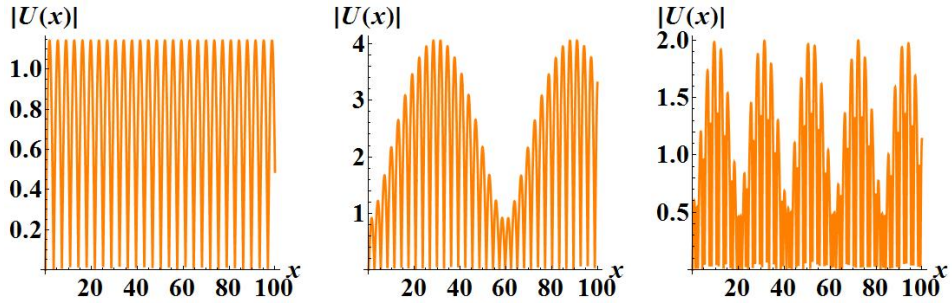

(a) (b) (c)

Figure 4.4: The linear coupler ($\beta = 0$) with $C = 1$ and $V_r = 1$. Intensity profile for various values of V_r in the unbroken $\mathcal{PT}$ regime ($G = 0.5$): (a) $V_r = 0$, (b) $V_r = 1$, and (c) $V_r = 10$.

of the Hermitian nature of the system. The system becomes non-Hermitian due to the presence of the gain/loss term and it is in the unbroken regime up to $G < C$ as depicted in Figure 4.5(b). From Figure 4.5(c) it is evident that the eigenvalues are complex for $G \geq C$ and it represents the broken regime. The influence of the transverse aperiodic potential on the beam intensity has been studied numerically. The intensity profile in the absence of the potential is shown in Figure 4.5(d). The presence of the potential varies the amplitude as illustrated in Figures 4.5(e) and 4.5(f) for low and high strength of the transverse aperiodic potential respectively.

4.4 The propagation dynamics

The nonlinear $\mathcal{PT}$ symmetric coupler is modeled by the equations 4.1 and 4.2. The solutions of the system has been studied in terms of the propagation constant μ:

$$\Psi_1(x, z) = \Phi_1(x, z)e^{-i\mu z}, \tag{4.10}$$

$$\Psi_2(x, z) = \Phi_2(x, z)e^{-i\mu z}. \tag{4.11}$$

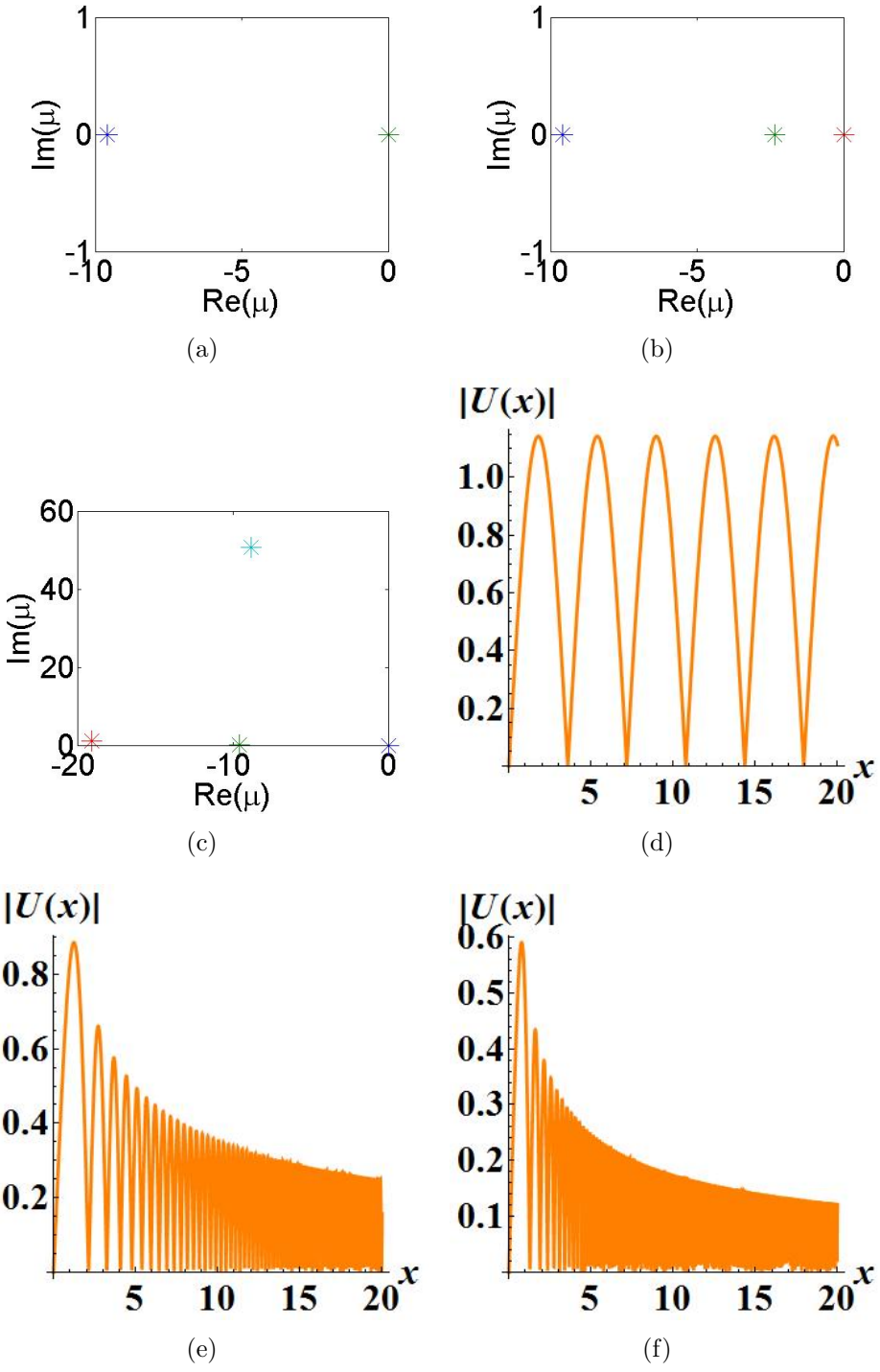

Figure 4.5: The linear $\mathcal{PT}$ symmetric coupler with transverse parabolic potential with $C = 1$ and $V_0 = 1$. (a) $G = 0$, (b) $G = 0.5$ and (c) $G = 2.0$. Intensity distribution for $G = 0.5$ with various values of V_0: (d) $V_0 = 0$, (e) $V_0 = 1$ and (f) $V_0 = 10$.

The substitution of Ψ_1 and Ψ_2 in equations 4.1 and 4.2 give the nonlinear eigenvalue problem:

$$i\frac{\partial \Phi_1}{\partial z} + \frac{\partial^2 \Phi_1}{\partial x^2} + V_R(x)\Phi_1 + \beta \left|\Phi_1\right|^2 \Phi_1 + iG\Phi_1 + C\Phi_2 = \mu\Phi_1, \tag{4.12}$$

$$i\frac{\partial \Phi_2}{\partial z} + \frac{\partial^2 \Phi_2}{\partial x^2} + V_R(x)\Phi_2 + \beta \left|\Phi_2\right|^2 \Phi_2 - iG\Phi_2 + C\Phi_1 = \mu\Phi_2. \tag{4.13}$$

The semi-analytical solutions of the system is obtained from the equations 4.12 and 4.13 using the variational method.

The conservative part of the Lagrangian of a nonlinear $\mathcal{PT}$ symmetric coupler is given by:

$$\begin{aligned} L_C = \frac{i}{2}(\Phi_1\Phi_{1z}^* - \Phi_1^*\Phi_{1z} + \Phi_2\Phi_{2z}^* - \Phi_2^*\Phi_{2z}) + \frac{1}{2}(\mid \Phi_{1x} \mid^2 + \mid \Phi_{2x} \mid^2) \\ -V_R(x) \mid \Phi_1 \mid^2 - V_R(x) \mid \Phi_2 \mid^2 - C(\Phi_2\Phi_1^* + \Phi_1\Phi_2^*) \\ +\mu(\mid \Phi_1 \mid^2 + \mid \Phi_2 \mid^2) - \frac{\beta}{2}(\mid \Phi_1 \mid^4 + \mid \Phi_2 \mid^4), \end{aligned} \tag{4.14}$$

where the subscript z and x represent the derivative with respect to the coordinates z and x respectively. The Euler-Lagrangian equation of the system is expressed as:

$$\frac{\partial}{\partial z}(\frac{\partial L_C}{\partial \Phi_{1z}^*}) - \frac{\partial L_C}{\partial \Phi_1^*} + \frac{\partial}{\partial z}(\frac{\partial L_C}{\partial \Phi_{2z}^*}) - \frac{\partial L_C}{\partial \Phi_2^*} = Q_i, \tag{4.15}$$

where Q_i incorporates all dissipative terms of the system. The dissipative terms are obtained from equations 4.12 and 4.13 as $Q_1 = -iG\Phi_1$ and $Q_2 = iG\Phi_2$. The reduced Lagrangian of the system is given by:

$$< L_C >= \int_{-\infty}^{\infty} L_c dx. \tag{4.16}$$

The trial solution for the variational analysis is chosen as:

$$\Phi_j(x,z) = A_j(z)Exp[\frac{-(x - x_0(z))^2}{2a^2} + iv(z)x + i\theta_j(z)], \tag{4.17}$$

in which the amplitudes $A_j(z)$, the velocity $v(z)$, the center of mass $x_0(z)$ and

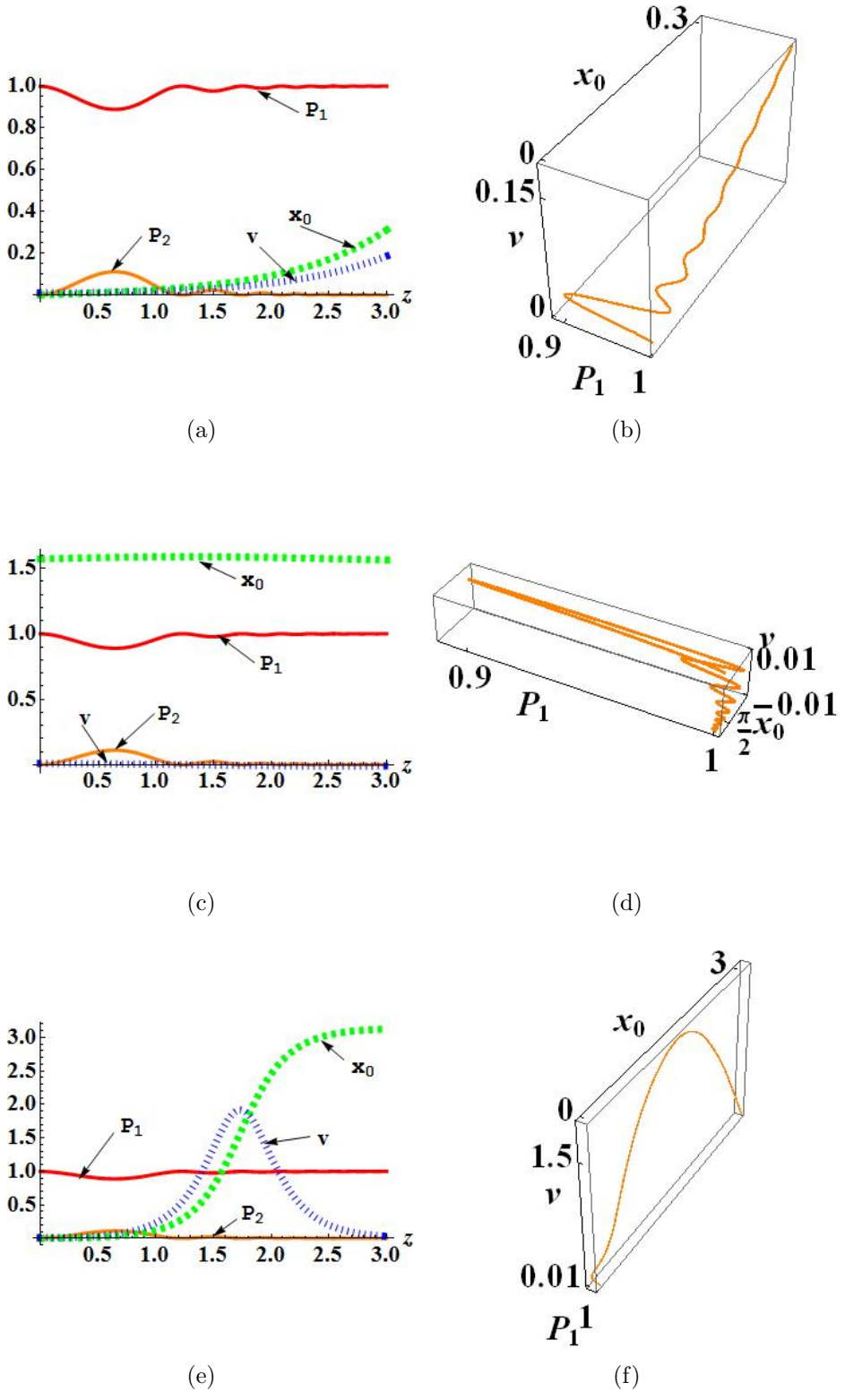

Figure 4.6: The results from variational method for the periodic potential. The variation of P_1, P_2, x_0 and v along z for parameter values $C = 1$, $\beta = 1$ and $\mu = 0.10$ with the initial conditions $v[0] = 0.01$, $\theta_1 = 0.50$ and $\theta_2 = 0.50$. First column for 2D plots, and second column for phase diagram of channel 1. First row: $V_r = 1$, $x_0[0] = 0$, second row: $V_r = 1$, $x_0[0] = \frac{\pi}{2}$ and third row: $V_r = 10$, $x_0[0] = 0$.

the phases $\theta_j(z)$ are the variational parameters with $j = 1, 2$ representing the channels. The width of the soliton a is considered as constant.

The intensity (power) of the channel is defined as:

$$\begin{aligned} p_j &= \int_{-\infty}^{\infty} \Phi_j \Phi_j^* dx, \\ &= \sqrt{\pi} A_j^2 a, \end{aligned} \tag{4.18}$$

where $j = 1$ for channel 1 and $j = 2$ for channel 2. The relative intensity is defined as the ratio of intensity of the channel to the total intensity which is defined as:

$$P_1 = \frac{p_1}{p_1 + p_2}, \qquad P_2 = \frac{p_2}{p_1 + p_2}, \tag{4.19}$$

for channels 1 and 2 respectively.

Case 1: The periodic potential

The reduced lagrangian of the system having the transverse periodic potential of the form in equation 4.3, is obtained as:

$$\begin{aligned} < L_C > = v_z x_0 (p_1 + p_2) + \theta_{1z}(p_1) + \theta_{2z}(p_2) + \frac{(p_1 + p_2)}{2a^2} \\ + v^2 (p_1 + p_2) - \mu (p_1 + p_2) - 0.5 V_r (p_1 + p_2)(1 - e^{-a^2} Cos(2x_0)) \\ - \frac{\beta (p_1^2 + p_2^2)}{2\sqrt{2\pi} a} - 2CCos(\delta)\sqrt{p_1 p_2}. \end{aligned} \tag{4.20}$$

The variational equations of the coupled system is given by:

$$p_{1z} = 2CSin(\delta)\sqrt{p_1 p_2} + 2Gp_1, \tag{4.21}$$

$$p_{2z} = -2CSin(\delta)\sqrt{p_1 p_2} - 2Gp_2, \tag{4.22}$$

$$x_{0z} = 2v, \tag{4.23}$$

$$\begin{aligned} \theta_{1z} = -V_r x_0 e^{-a^2} Sin(2x_0) + 0.5 V_r (1 - e^{-a^2} Cos(2x_0)) + \mu - v^2 \\ - \frac{1}{2a^2} + \frac{\beta p_1}{\sqrt{2\pi} a} + \sqrt{\frac{p_2}{p_1}} CaCos(\delta), \end{aligned} \tag{4.24}$$

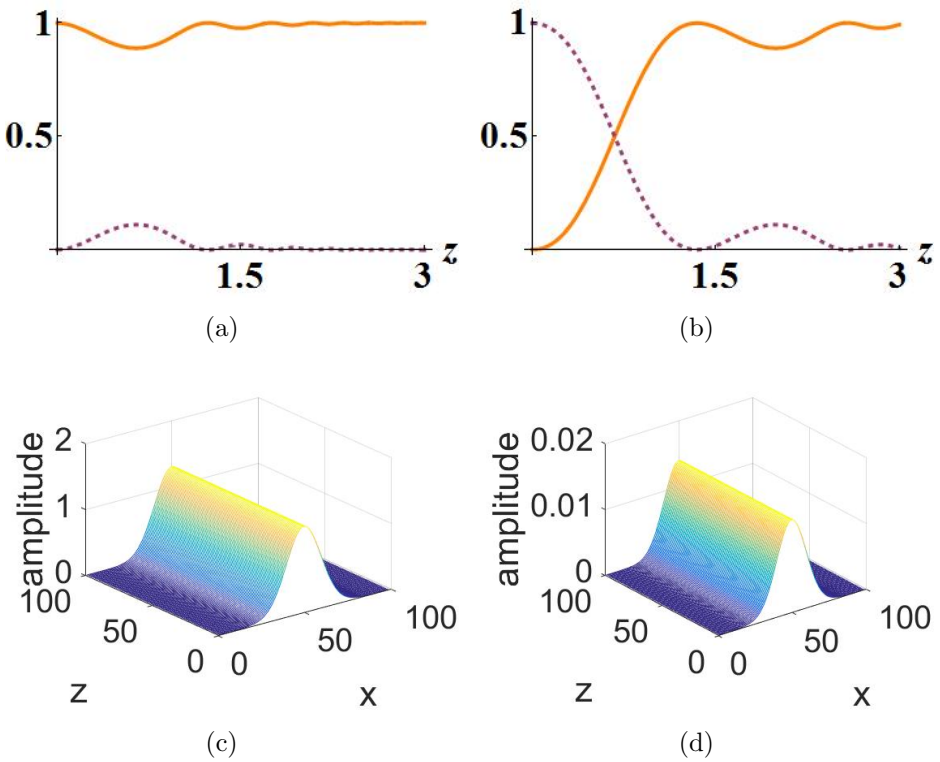

Figure 4.7: The nonlinear $\mathcal{PT}$ symmetric coupler with transverse periodic potential. First row: The results from variational method. The relative intensities in the two channels (Solid for channel 1 and dashed for channel 2) as a funtion of z for parameter values $C = 1$,$V_r = 1$ and $\mu = 0.10$ with the initial conditions $x_0[0] = 0$, $v[0] = 0.01$, $\theta_1 = 0.50$ and $\theta_2 = 0.50$. (a) Input beam to channel 1(gain), (b) Input beam to channel 2 (loss). Second row: The results from direct simulation. The soliton evolution for $V_r = 1$, $\beta = 1$, $x_0[0] = 0$, $v[0] = 0.01$, $\theta_1 = 0.5$ and $\theta_2 = 0.5$. c) channel 1 and d) channel 2.

$$\theta_{2z} = -V_r x_0 e^{-a^2} Sin(2x_0)) + 0.5V_r(1 - e^{-a^2} Cos(2x_0)) + \mu - v^2 - \frac{1}{2a^2} + \frac{\beta p_2}{\sqrt{2\pi}a} + \sqrt{\frac{p_1}{p_2}} CaCos(\delta), \tag{4.25}$$

$$v_z = V_r a sin(2x_0) e^{-a^2}, \tag{4.26}$$

where the subscript z represents the derivative with respect to z. Here the width a is assumed as unity.

The evolution of the solitons in term of x_0, v, and P_i has been studied using a system of six coupled equations 4.21-4.26. Figure 4.6(a) shows that the soliton is trapped in channel 1 with slight oscillation in power and nearly zero power in

channel 2. If initially its center lies at the minimum of the potential, its velocity and centre of mass increase whose phase space is depicted in Figure 4.6(b). If the initial position of the soliton lies at $x_0 = \frac{\pi}{2}$ (i.e., at the maximum of the potential), the power slightly oscillates, the center of mass and the velocity is constant as illustrated in Figure 4.6(c) with nearly zero power in channel 2. The phase diagram of channel 1 is plotted in Figure 4.6(d). When V_r has large value, the power is a constant, the center of mass increases and the velocity completes a cycle as shown in Figure 4.6(e) for channel 1. Figure 4.6(f) shows the corresponding phase diagram of channel 1.

The variation of power along the propagation direction has been plotted in Figures 4.7(a)-4.7(b). The beam get trapped in the channel with gain in the case of the nonlinear $\mathcal{PT}$ symmetric coupler. When the input power is initially in channel 1, it remains there as shown in Figure 4.7(a). Figure 4.7(b) depicts that the power switches from channel 2 (loss) to channel 1 (gain) if input beam is in the channel with loss (i.e, channel 2).

The direct simulation of the system has been done using finite difference method. The beam evolution has been studied with initial power in channel 1. The soliton evolves with constant power as shown in Figure 4.7(c). The intensity in the second channel is negligible as depicted in Figure 4.7(d). The direct simulation is in agreement with the variational results.

Case 2: The aperiodic potential

The reduced lagrangian of the system with the transverse aperiodic potential described by equation 4.4, is expressed as:

$$< L_C >= v_z x_0(p_1+p_2) + \theta_{1z}p_1 + \theta_{2z}p_2 + \frac{p_1+p_2}{2a^2} + v^2(p_1+p_2) - \mu(p_1+p_2) - \frac{\beta(p_1^2+p_2^2)}{2\sqrt{2\pi}a} - 0.5V_0(p_1+p_2)(a^2+2x_0^2) - 2CCos(\delta)\sqrt{p_1p_2}. \quad (4.27)$$

The variational equations of the coupled system is obtained as:

$$p_{1z} = 2CSin(\delta)\sqrt{(p_1 p_2)} + 2Gp_1, \quad (4.28)$$

$$p_{2z} = -2CSin(\delta)\sqrt{(p_1 p_2)} - 2Gp_2, \quad (4.29)$$

$$x_{0z} = 2v, \quad (4.30)$$

$$\theta_{1z} = \mu + 0.5V_0(a^2 + 2x_0^2) - v^2 - \frac{1}{2a^2} + \frac{\beta p_1}{\sqrt{2\pi}a} + \sqrt{\frac{p_2}{p_1}}CaCos(\delta), \quad (4.31)$$

$$\theta_{2z} = \mu + 0.5V_0(a^2 + 2x_0^2) - v^2 - \frac{1}{2a^2} + \frac{\beta p_2}{\sqrt{2\pi}a} + \sqrt{\frac{p_1}{p_2}}CaCos(\delta), \quad (4.32)$$

$$v_z = 2V_0 x_0. \quad (4.33)$$

where V_0 be the depth of the potential. The width, a is assumed as unity.

The beam dynamics in term of x_0, v, and P_i, has been studied numerically by solving the coupled equations 4.28-4.33. The beam get trapped in the channel with gain due to the nonlinearity. Figure 4.8(a) shows that the power slightly oscillates whereas its velocity and center of mass increase representing a travelling soliton with nearly zero power in channel 2. Figure 4.8(b) illustrates corresponding phase diagram for channel 1. The direct simulation of the system has been done using finite difference method. The soliton evolves with constant power in channel 1 in the unbroken regime as depicted in Figure 4.8(c). The power in the second channel is nearly zero, and it evolves as shown in Figure 4.8(d).

4.5 The linear stability analysis

The linear stability of the stationary states of the coupled system has been investigated using Bogoliubov-De Genes (BDG) equations. Consider small perturbations of the stationary states of the system as:

$$\Psi_1(x,z) = (\Phi_1(x) + q_1(x)e^{i\lambda z} + q_2(x)e^{-i\lambda^* z})e^{i\mu z},$$
$$\Psi_2(x,z) = (\Phi_2(x) + q_3(x)e^{i\lambda z} + q_4(x)e^{-i\lambda^* z})e^{i\mu z}. \quad (4.34)$$

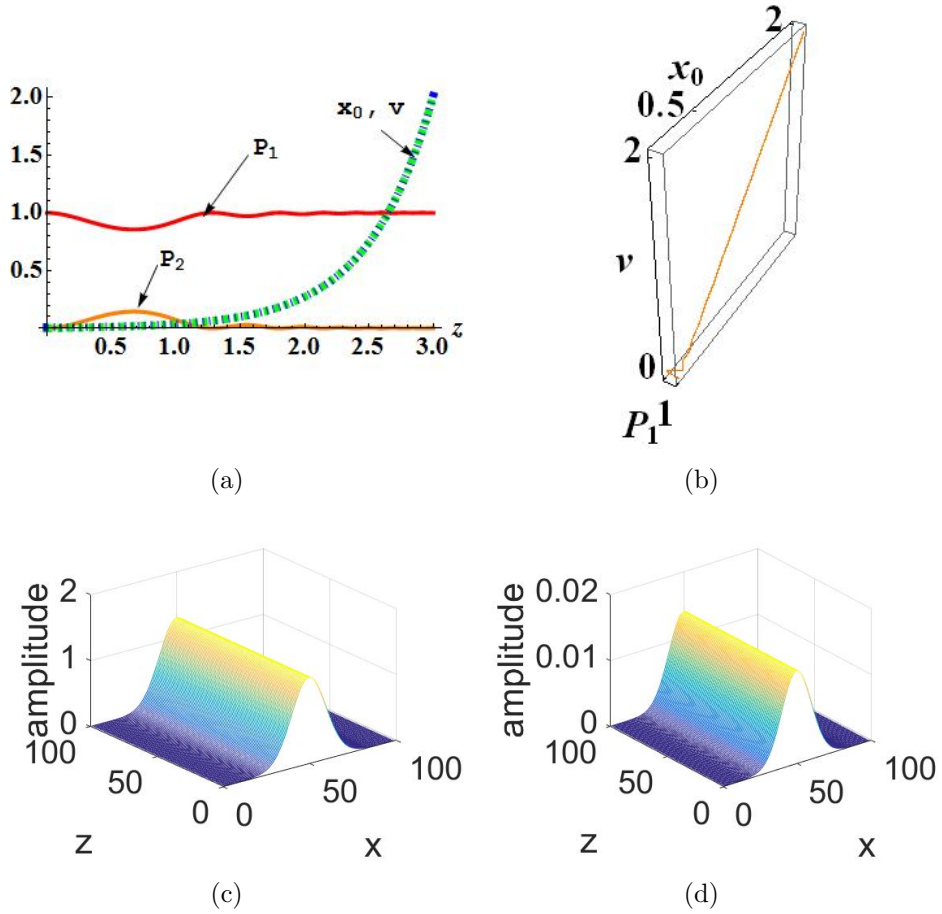

Figure 4.8: The results of $\mathcal{PT}$ symmetric nonlinear coupler with a transverse parabolic potential. First row from variational method for parameter values $C = 1$, $\beta = 1$, $V_0 = 1$ and $\mu = 0.10$ with the initial conditions $v[0] = 0.01$, $x_0[0] = 0$, $\theta_1 = 0.50$ and $\theta_2 = 0.50$. (a) P_1, P_2, x_0 and v along z, and (b) phase diagram of Channel 1. Second row: The power evolution for $V_0 = 1$, $\beta = 1$, $x_0[0] = 0$, $v[0] = 0.01$, $\theta_1 = 0.5$ and $\theta_2 = 0.5$. c) channel 1 and d) channel 2.

The linearizing equations 4.1 and 4.2 due to the small values of q_1, q_2, q_3 and q_4 provide the following matrix A which is given by:

$$\begin{pmatrix} L_1 + iG & \beta\Phi_1^2 & C & 0 \\ -\beta(\Phi_1^*)^2 & -L_1 + iG & 0 & -C \\ C & 0 & L_2 - iG & \beta\Phi_2^2 \\ 0 & -C & -\beta(\Phi_2^*)^2 & -L_2 - iG \end{pmatrix} \tag{4.35}$$

where

$$L_1 = -\mu + \frac{d^2}{dx^2} + V_R + \beta|\Phi_1|^2,$$
$$L_2 = -\mu + \frac{d^2}{dx^2} + V_R + \beta|\Phi_2|^2.$$

When $\Phi_1(x) = \Phi_2(x) = U(x)$, it obeys the equation 4.7. Then the matrix A is rewritten in terms of $Cos\delta$ as:

$$\begin{pmatrix} L & \beta U^2 & Ccos\delta & 0 \\ -\beta(U^*)^2 & -L & 0 & -C \\ Ccos\delta & 0 & L & \beta U^2 \\ 0 & -Ccos\delta & -\beta(U^*)^2 & -L \end{pmatrix} \tag{4.36}$$

where $Cos(\delta) > 0$ for high-frequency modes and $Cos(\delta) < 0$ for low-frequency modes.

We have applied the spectral methods based on Chebyshev polynomials to solve the system. A grid is chosen extending 40 along x to evaluate the potential and the diffraction operators. The eigenvalues of 'A' are λ's. λ's are purely real for stable solutions. If the imaginary part of the eigenvalue $Im(\lambda)$ is negative, then the perturbation mode increases exponentially. The positive $Im(\lambda)$ results in exponentially decreasing perturbation modes.

The stability of the high frequency solutions of the nonlinear $\mathcal{PT}$ symmetric coupler having transverse periodic potential in equation 4.3 has been analyzed and the results are plotted in Figures 4.9(a)-4.9(b). The solutions are stable with purely real eigenvalues. The linear stability analysis of the system with transverse parabolic potential whose profile is given by equation 4.4, has been done. Figures 4.9(c) and 4.9(d) illustrate that the eigenvalues are purely real for high frequency soliton.

The low-frequency modes are unstable for both periodic and the aperiodic potential. Figures 4.10(a) and 4.10(b) show that the perturbation eigenmodes grow exponentially for periodic potential. This is true for aperiodic potential

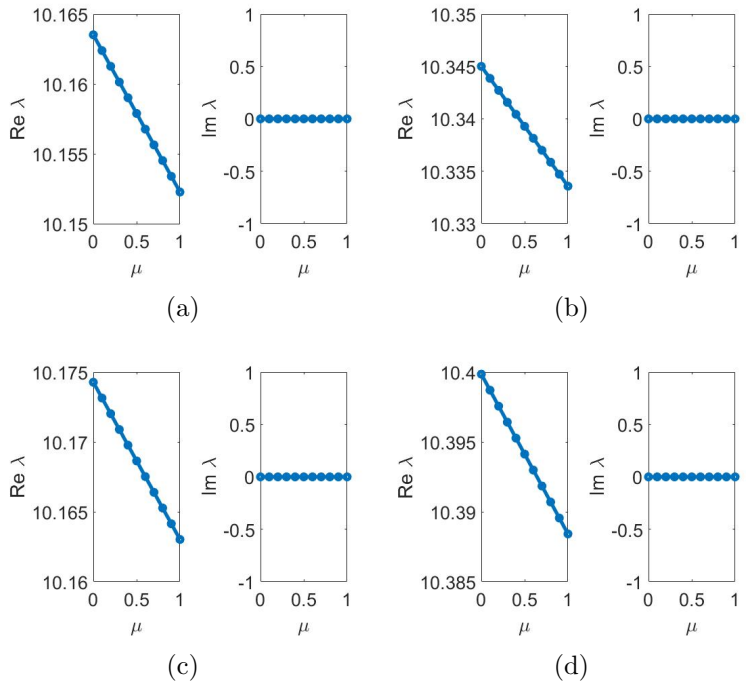

Figure 4.9: The results of linear stability analysis of the system for high frequency modes. The real and imaginary parts of the perturbation eigenvalues (λ) versus the propagation constant μ are shown. First row for periodic potential with $\beta = 1$: (a) $V_r = 1$, and (b) $V_r = 5$. Second row for parabolic potential with $\beta = 1$: (c) $V_0 = 1$, and (d) $V_0 = 5$.

also as depicted in Figures 4.10(c) and 4.10(d).

4.6 Conclusion

The $\mathcal{PT}$ symmetric coupler in a transverse periodic and aperiodic potential has been studied for linear and nonlinear regimes. The propagation-invariant solutions of the system were studied and it has been found that the high-frequency and low-frequency modes reside in the minimum of the potential both for periodic and parabolic potentials. High strength of the periodic potential causes the modes to be more confined in the lattice where as high depth of the parabolic potential leads to the confinement of the mode at the minimum of the potential. The amplitude of the low-frequency modes are slightly greater than that of the high-frequency modes. The $\mathcal{PT}$ symmetric regime of the system has been deter-

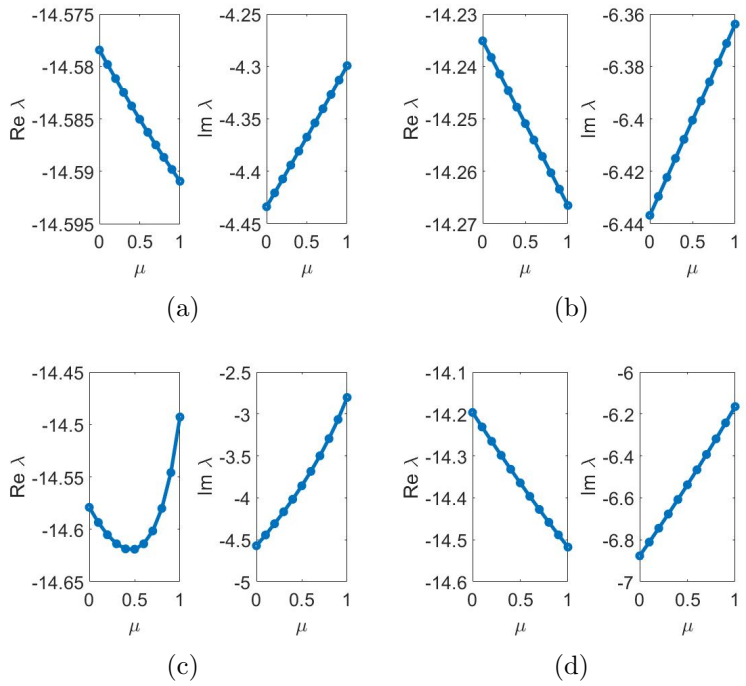

Figure 4.10: The results of linear stability analysis of the system for low-frequency modes. The real and imaginary parts of the perturbation eigenvalues (λ) versus the propagation constant μ are shown. First row for periodic potential with $\beta = 1$: (a) $V_r = 1$, and (b) $V_r = 5$. Second row for parabolic potential with $\beta = 1$: (c) $V_0 = 1$, and (d) $V_0 = 5$.

mined in the linear case and the dynamics of the modes have been investigated for those parameter values. The propagation constants of the system is real in the $\mathcal{PT}$ symmetric regime whereas it is complex in the broken $\mathcal{PT}$ symmetric domain. As far as the gain/loss coefficient is less than the coupling coefficient, the coupler is in unbroken regime irrespective of the type of the transverse potential. The transverse periodic potential creates band gaps and thereby forbidden propagation constants whereas no band gaps appear for parabolic potential. We have analyzed the soliton dynamics in the case of nonlinear coupler with transverse potentials. The beam get trapped in the channel with gain. For low values of the strength of the transverse periodic and aperiodic potentials, velocity and center of mass of the soliton increases. When the center of the soliton coincides with the minimum of the periodic potential, we get the trapped solitons for high strength of the periodic potential. The linear stability analysis reveals that

the high-frequency modes are stable for both periodic and parabolic potentials, and the low-frequency modes are unstable. These results find applications in photonic devices for all-optical switching.

Bibliography

[1] L.Feng and Y.L.Xu and W.S.Fegadolli and M.H.Lu and J.E.B.Oliveira and V.R.Almeida and Y.F.Chen and A.Scherer. Experimental demonstration of a unidirectional reflectionless parity-time metamaterial at optical frequencies. Nat. Mater. 2013;12:108.

[2] Lifante G. Integrated Photonics: Fundamentals (Wiley, 2003).

[3] S.V.Suchkov and A. A.Sukhorukov and J.Huang and S.V.Dmitriev and C.Lee and Y.S.Kivshar. Nonlinear switching and solitons in PT-symmetric photonic systems. Laser and Photonics Reviews, September(2015)

[4] Y.J.Chen and A.W.Snyder and D.N.Payne. Twin core nonlinear couplers with gain and loss. IEEE Journ. Quant. Electron. 1992;28:239245.

[5] S.Jensen. The nonlinear coherent coupler. IEEE J. Quant. Electron. **18** 15801583 (1982).

[6] N.V.Alexeeva and I.V.Barashenkov and Andrey A.Sukhorukov and Yuri S. Kivshar. Optical solitons in PT-symmetric nonlinear couplers with gain and loss. Phys. Rev. A. 2012;85:063837.

[7] B.Daino and G.Gregori and S.Wabnitz. Stability analysis of nonlinear coherent coupling. J. Appl. Phys. 1985;58 45124514.

[8] K.A.Muhsina and P.A.Subha. Soliton beam dynamics in parity-time symmetric nonlinear coupler. Eur. Phys. J. D. 2015;69:7 (17).

[9] R.Driben and B.A.Malomed. Stability of solitons in parity-time-symmetric couplers. Opt. Lett. 2011; 36:4323.

[10] R.Driben and B.A.Malomed. Stabilization of solitons in PT models with supersymmetry by periodic management. Euro. phys. lett. 2011; 96:51001.

[11] Yu.V.Bludov and V.V.Konotop and B.A.Malomed. Stable dark solitons in -symmetric dual-core waveguides. Phys. Rev. A 2013; 87:013816.

[12] I.V.Barashenkov and S.V.Suchkov and A.A.Sukhorukov and S.V.Dmitriev and Y.S.Kivshar. Breathers in PT-symmetric optical couplers. Phys. Rev. A 2012;86:053809.

[13] Yu.V.Bludov and R.Driben and V.V.Konotop and B.A.Malomed. Instabilities, solitons, and rogue waves in PT-coupled nonlinear waveguides. J. Optics. 2013;15:064010.

[14] Wiktor Walasik and Natalia M.Litchinitser. Phase transition in multimode nonlinear parity-time-symmetric waveguide couplers. Scientific reports. February 2016;19826.

[15] Yannis Kominis and Tassos Bountis and Sergej Flach. The Asymmetric Active Coupler: Stable Nonlinear Supermodes and Directed Transport. Scientific reports. September 2015;33699.

[16] Senlin Zhang and Zhengdong Yong and Yuguang Zhang and Sailing He. Parity-Time Symmetry Breaking in Coupled Nanobeam Cavities. Scientific reports. April 2016;24487.

[17] P.V.Paulau and D.Gomila and T.Ackemann and N.A.Loiko and W.J.Firth. Self-localized structures in vertical-cavity surface-emitting lasers with external feedback. Phys. Rev. E. 2008;78:016212.

[18] P.V.Paulau and D.Gomila and P.Colet and N.A.Loiko and N.N.Rosanov and T.Ackemann and W.J.Firth. Vortex solitons in lasers with feedback. Opt. Exp. 2010;18:8859.

[19] Sergey V Suchkov and B.A.Malomed and Sergey V Dmitriev and Y.S.Kivshar. Solitons in a chain of parity-time-invariant dimers. Phys. Rev. E. 2011;84:046609.

[20] Chunfei Li and Guangming Xu and Liansheng Ma and Na Dou and Hong Gu. An erbium-doped fibre nonlinear coupler with coupling ratios controlled by pump power. J. Opt. A: Pure Appl. Opt. 2005;7:540.

[21] I.V.Barashenkov and G.S.Jackson and S.Flach. Blow-up regimes in the -symmetric coupler and the actively coupled dimer. Phys. Rev. A 2013 88:053817.

[22] I.V.Barashenkov and Mariagiovanna Gianfreda. An exactly solvable $\mathcal{PT}$-symmetric dimer from a Hamiltonian system of nonlinear oscillators with gain and loss. J. Phys. A: Math. Theor. 2014;47:282001.

[23] G.Burlak and B.A.Malomed. Stability boundary and collisions of two-dimensional solitons in PT-symmetric couplers with the cubic-quintic nonlinearity. Phys. Rev. E. 2013;88:062904-8.

[24] K.O.Hill and Y.Fujii and D.C.Johnson and B.S.Kawasaki. Photosensitivity in optical fiber waveguides: Application to reflection filter fabrication. Appl. Phys. Lett. 1978;32:647.

[25] T.Erdogan. Fiber Grating Spectra. J.Lightwave.Technol. 1997;15:1277.

[26] P.Yeh. Optical Waves in Layered Media (Wiley, New York, 1988).

[27] B.B.Baizakov and B.A.Malomed and M.Salerno. Multidimensional solitons in periodic potentials. Euro.Phys.Lett. 2003;63:5.

[28] T.P.Suneera and P.A.Subha. Parity-time symmetric coupler in transverse periodic and aperiodic potentials. The European Physical Journal Plus. 2018;133:84.

SUNEERA T. P. “STUDIES ON BEAM DYNAMICS IN SINGLE AND COUPLED PARITY-TIME SYMMETRIC SYSTEMS WITH KERR AND NONLOCAL NONLINEARITY”. THESIS. DEPARTMENT OF PHYSICS, UNIVERSITY OF CALICUT, 2018.

Chapter 5

Nonlocal gap solitons in $\mathcal{PT}$ symmetric coupler

5.1 Introduction

The $\mathcal{PT}$ symmetric couplers have been extensively studied because of its applications in ultra-fast data transfer and all-optical switching devices. The $\mathcal{PT}$ symmetric couplers in nonlinear regime possess novel features depending on the nature of the media and the intensity of the beam. Hence these systems have been investigated in various types of nonlinearity and coupling terms.

The $\mathcal{PT}$ symmetric coupler with third order dispersion in Kerr media has been studied [1]. The existence and the stability of the solitons has been reported in $\mathcal{PT}$ symmetric coupler [2]. The symmetric and the asymmetric solitons have been investigated in dual-core coupler with quadratic and cubic nonlinearity [3]. The $\mathcal{PT}$ symmetric coupler has been studied in the context of competing cubic-quintic nonlinearity [4].

The symmetric and asymmetric solitons have been reported in the nonlocal coupler [5]. The detailed study of the soliton solutions in nonlocal coupler has been done [6]. But the $\mathcal{PT}$ symmetric coupler with nonlocal nonlinearity has not been reported yet. In this context, we have studied the nonlocal gap solitons

in $\mathcal{PT}$ symmetric coupler.

This chapter deals with the $\mathcal{PT}$ symmetric coupler having transverse periodic modulation with nonlocal nonlinearity. The model of the $\mathcal{PT}$ symmetric nonlocal coupler has been defined. The propagation invariant modes and the linear stability analysis have also been discussed. The study has been further extended to the propagation dynamics of the modes.

5.2 The $\mathcal{PT}$ symmetric nonlocal coupler

The beam dynamics of the system has been modeled by modifying the equations of the nonlinear coupler [7] as given below:

$$i\Psi_{1z} + \Psi_{1xx} + (V_R(x) + iG + V_{NL1})\Psi_1 + C\Psi_2 = 0, \tag{5.1}$$

$$V_{NL1} - \sigma\frac{\partial^2 V_{NL1}}{\partial x^2} = |\Psi_1|^2, \tag{5.2}$$

$$i\Psi_{2z} + \Psi_{2xx} + (V_R(x) - iG + V_{NL2})\Psi_2 + C\Psi_1 = 0, \tag{5.3}$$

$$V_{NL2} - \sigma\frac{\partial^2 V_{NL2}}{\partial x^2} = |\Psi_2|^2, \tag{5.4}$$

where Ψ_1 and Ψ_2 are the fields (the electric fields in optics or the particle distribution of matter waves) in the gain and loss channels respectively, V_{NL1} and V_{NL2} are the corresponding nonlocal nonlinearities in the channels, C is the coefficient of coupling and G is the gain/loss coefficient. The range of the nonlocality is σ, $\sigma > 0$ for defocusing, $\sigma < 0$ for self-focusing, and $\sigma = 0$ for Kerr nonlinearities. The real potential $V_R(x) = V_r sin^2(x)$, is along the transverse direction x, with period π and the strength V_r. The subscripts z and xx denote the first derivative with respect to z and the second derivative with respect to x respectively.

The solutions of the system Φ_1 and Φ_2 in terms of the propagation constant μ are obtained from:

$$\Psi_1(x,z) = \Phi_1(x,z)e^{i(-\mu z+\theta_1)}, \tag{5.5}$$

$$\Psi_2(x,z) = \Phi_2(x,z)e^{i(-\mu z+\theta_2)}, \tag{5.6}$$

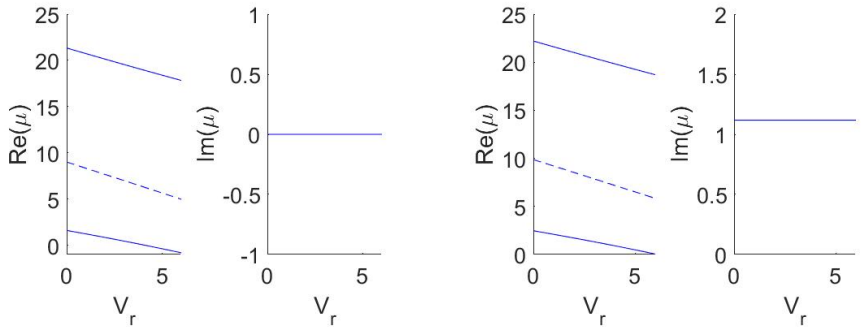

(a) (b)

Figure 5.1: The linear coupler with $C = 1$. The real ($Re(\mu)$) and imaginary ($Im(\mu)$) parts of the eigenvalues are plotted by varying V_r. (a) The unbroken regime for $G = 0.5$ and (d) the broken regime for $G = 1.5$. The bands are named from bottom to top such as first, second and third.

where θ_1 and θ_2 are the phases of the fields. The phase difference between the fields is represented by $\delta = \theta_1 - \theta_2$ and $Sin(\delta) = \frac{G}{C}$.

The solutions satisfy the equations:

$$i\Phi_{1z} + \mu\Phi_1 + \Phi_{1xx} + (V_R(x) + V_{NL1})\Phi_1 + CCos(\delta)\Phi_2 + iG(\Phi_1 - \Phi_2) = 0, \quad (5.7)$$

$$V_{NL1} - \sigma\frac{\partial^2 V_{NL1}}{\partial x^2} = |\Phi_1|^2, \quad (5.8)$$

$$i\Phi_{2z} + \mu\Phi_2 + \Phi_{2xx} + (V_R(x) + V_{NL2})\Phi_2 + CCos(\delta)\Phi_1 + iG(\Phi_1 - \Phi_2) = 0, \quad (5.9)$$

$$V_{NL2} - \sigma\frac{\partial^2 V_{NL2}}{\partial x^2} = |\Phi_2|^2. \quad (5.10)$$

5.3 The propagation invariant modes

When $\Phi_1(x, z) = \Phi_2(x, z) = U(x)$, we get the propagation invariant modes of the system from Equations 5.7-5.10 which has the form:

$$\frac{d^2U}{dx^2} + V_R(x)U + V_{NL}(x)U + C_{th}U + \mu U = 0, \quad (5.11)$$

$$C_{th} = CCos(\delta) = \sqrt{C^2 - G^2},$$

$$V_{NL} - \sigma\frac{d^2 V_{NL}}{dx^2} = |U|^2. \quad (5.12)$$

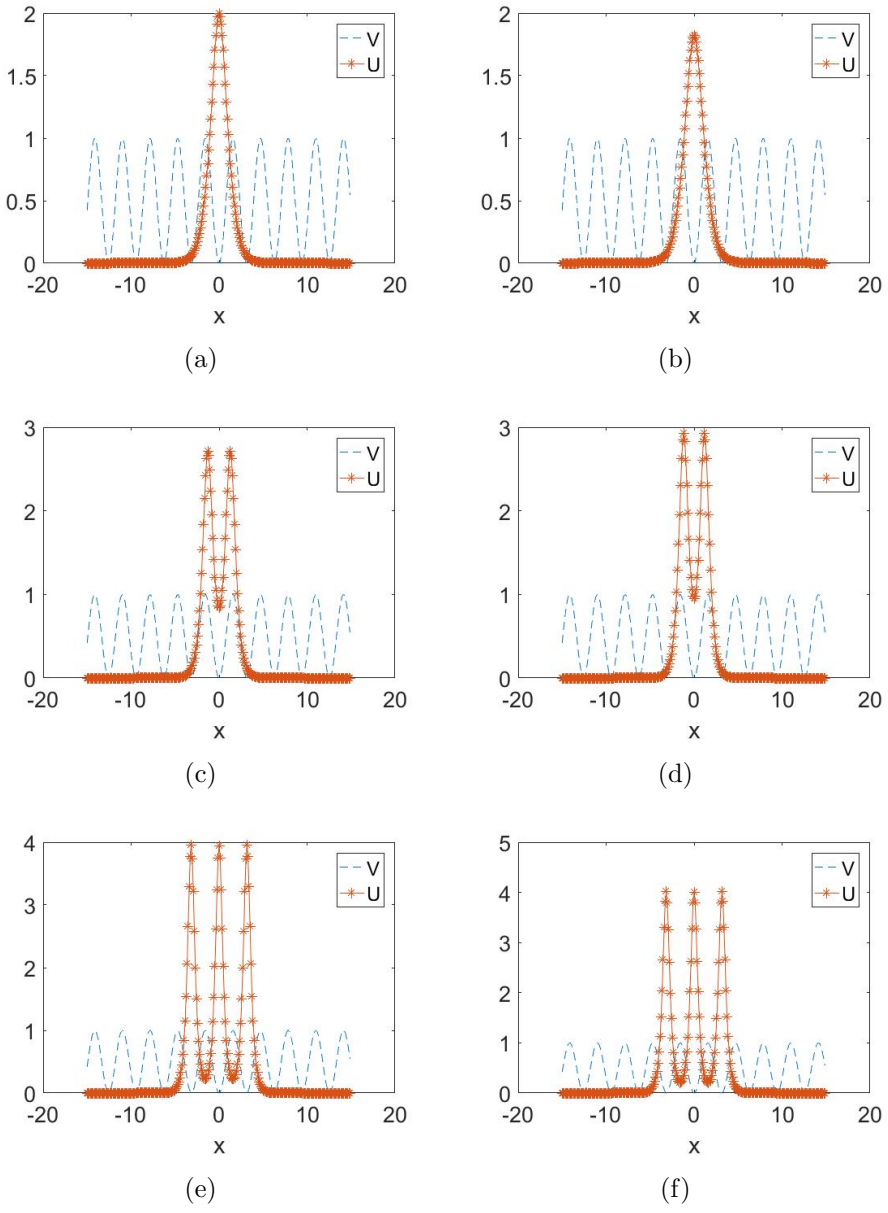

Figure 5.2: The propagation-invariant high-frequency (first column) and low-frequency (second column) modes of the nonlinear coupler for $C = 1$,$G = 0.5$, $\sigma = 1.0$, and $V_r = 1.0$ (dashed blue, periodic potential). First, second and third rows for single-hump, double-hump, and triple-hump modes respectively. (a) $\mu = 3.4$, (b) $\mu = 1.4$, (c) $\mu = 5.5$, (d) $\mu = 4.4$, (e) $\mu = 8.9$, and (f) $\mu = 7.4$.

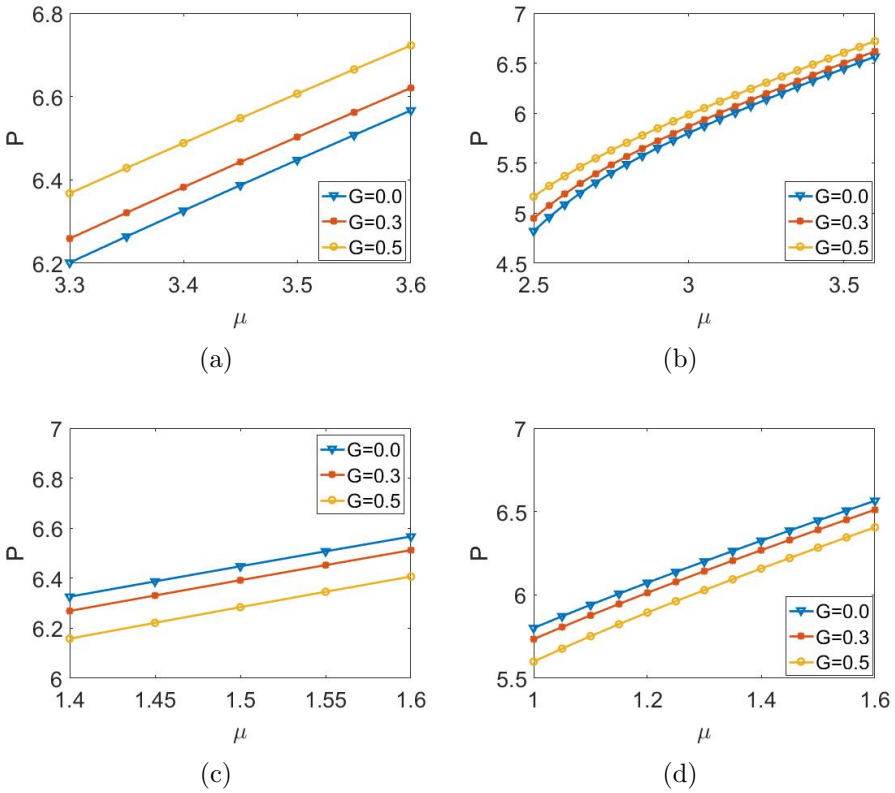

Figure 5.3: The propagation-invariant high-frequency and low-frequency modes of the nonlinear coupler for $C = 1$,$G = 0.5$, $\sigma = 1.0$, and $V_r = 1.0$ (dashed blue, periodic potential). The variation of power P of single-hump mode with μ for various values of G: (a) and (c) $\sigma = 0.5$, and (b) and (d) $\sigma = 1.0$.

5.3.1 Linear eigenmodes

The linearised version of the system is described by equation 5.11 with $V_{NL} = 0$ which is given by:

$$\frac{d^2U}{dx^2} + V_R(x)U + C_{th}U + \mu U = 0. \tag{5.13}$$

Since the potential is periodic, the equation 5.13 yields Bloch waves of the form $U(x) = U_K(x)e^{iKx}$, where K represents the Bloch momentum with the periodicity condition $U_K(x + \pi) = U_K(x)$. The Bloch solutions satisfy the equation:

$$-\frac{d^2U_K}{dx^2} - 2iK\frac{dU_K}{dx} - (V_R(x) - K^2)U_K - C_{th}U_K = \mu U_K. \tag{5.14}$$

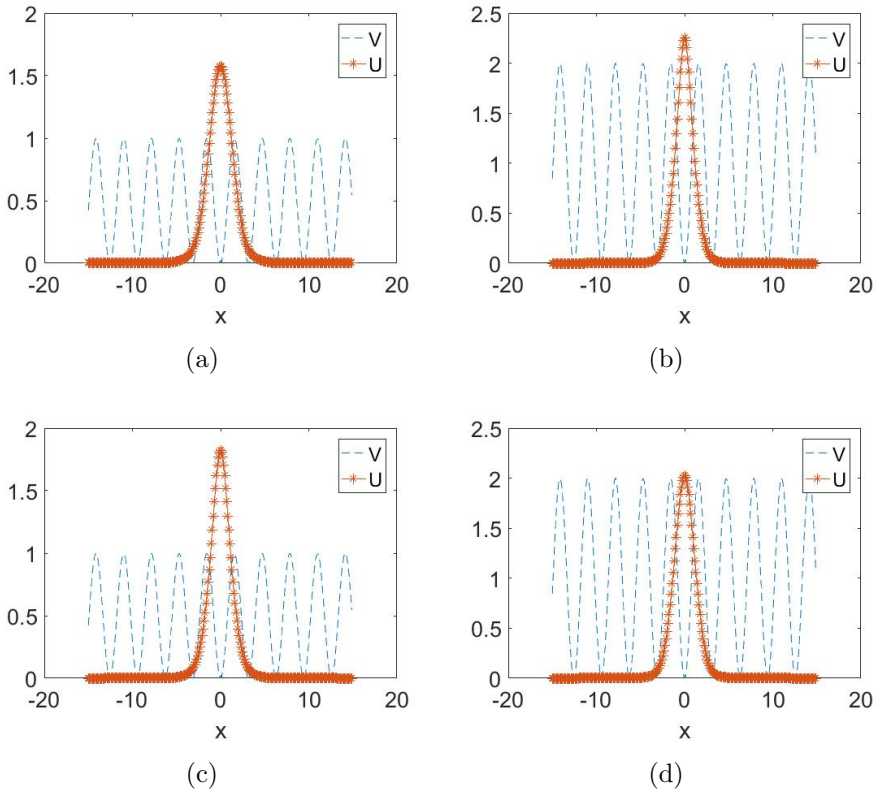

Figure 5.4: The propagation-invariant low-frequency modes of the nonlinear coupler for $C = 1$, $G = 0.5$ and $\sigma = 1.0$ (dashed blue, periodic potential). First row for high-frequency mode (solid red) and second row for low-frequency mode (solid red). (a) $V_r = 1$ and $\mu = 2.8$, (b) $V_r = 2$ and $\mu = 4.4$, (c) $V_r = 1$ and $\mu = 1.4$, and (d) $V_r = 2$ and $\mu = 2.4$.

The eigenvalues of the system is calculated by the spetral method based on Chebychev polynomials [8]. The eigenvalues are plotted by varying V_r as shown in Figures 5.1(a) and 5.1(b). It is found that the system possesses band structure due to the presence of the transverse periodic potential. When the gain/loss coefficient G is less than C, the system possess real eigenvalues as evident from Figure 5.1(a). This is the unbroken $\mathcal{PT}$ symmetric regime. When $G > C$, $Im(\mu)$ is not equal to zero, representing the broken regime as shown in Figure 5.1(b).

5.3.2 Nonlinear eigenmodes

The nonlinear eigenmodes of the system has been obtained from Equations 5.11 and 5.12 by employing Newton's Conjugate Gradient method. When $C_{th} > 0$,

the eigenmodes are termed as high-frequency modes. If $C_{th} < 0$, eigenmodes are known as low-frequency modes. Both modes coexist in the system as far as $G < C$. When $G = C$, high-frequency and low-frequency modes merge together. Both the high-frequency and the low-frequency modes are analysed by varying the range of the nonlocal nonlinearity σ and the strength of the potential V_r. Both modes exist for a set of continuous values of μ which strongly depends on the range of the nonlocality σ.

Figures 5.2(a)-5.2(e) illustrate the high-frequency single-hump, double-hump and triple-hump modes respectively for $\sigma = 1$. The high-frequency modes exist in the first band gap. High-frequency single-hump modes lie in the lower part of the first band gap as depicted in Figure 5.2(a). The mode get trapped in the minimum of the transverse potential. As μ increases further to the middle of the first band gap, the double-hump high-frequency modes are obtained as shown in Figure 5.2(c). The double-hump mode spreads through two consecutive lattices. When μ lies nearest to the second band, the triple-hump high-frequency modes are observed. The triple-hump mode lies across three consecutive lattices. The low-frequency single-hump, double-hump and triple-hump modes are plotted in Figures 5.2(b)-5.2(f). The single-hump mode lie in the semi-infinite band gap as shown in Figure5.2(b). The double-hump and triple-hump modes lie in the first band gap as plotted in Figures 5.2(d)-5.2(f).

The power of single-hump high-frequency modes P versus μ with various values of G for $\sigma = 0.5$ and $\sigma = 1.0$ are shown in Figures 5.3(a) and 5.3(b) respectively. P increases with μ and G. The power of single-hump low-frequency modes P as a function of μ with various values of G for $\sigma = 0.5$ and $\sigma = 1.0$ are depicted in Figures 5.3(c) and 5.3(d) respectively. P increases with μ whereas decreases with G.

As V_r increases, the amplitude of single-hump high-frequency mode increases as shown in Figures 5.4(a) and 5.4(b). Similarly the amplitude of single-hump low-frequency mode increases as plotted in Figures 5.4(c) and 5.4(d). As V_r increases, the propagation constants of both modes increase.

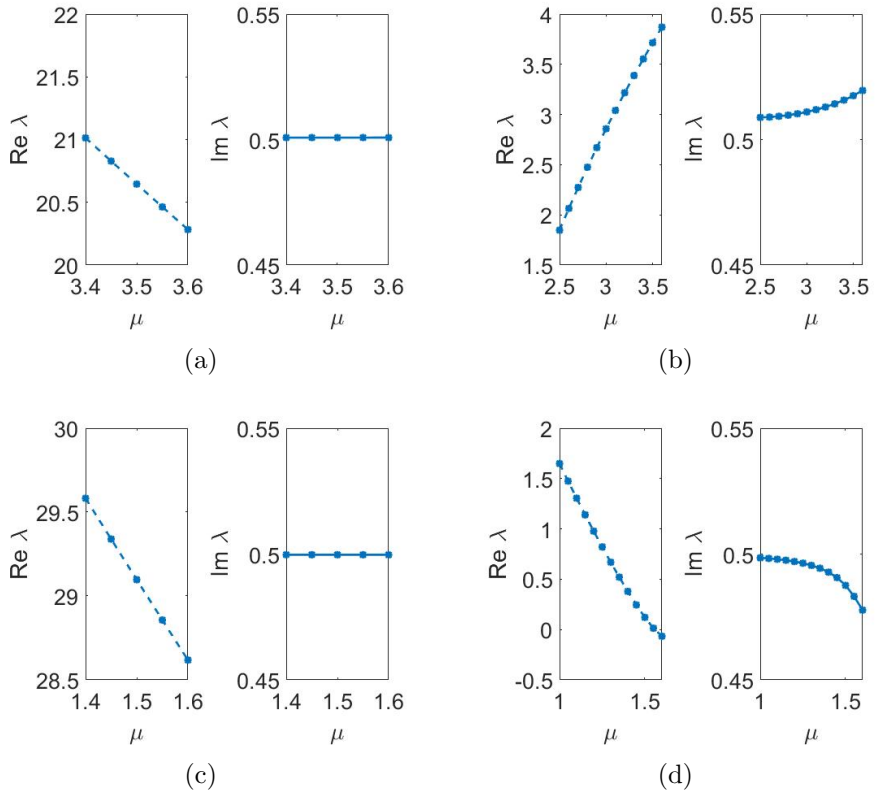

Figure 5.5: The linear stability analysis of the nonlocal coupler for $C = 1$, and $V_r = 1$. The real and the imaginary parts of the perturbation eigenvalues as function of μ. First and second rows for high-frequency and low-frequency modes respectively with $\sigma = 0.5$ (first column) and $\sigma = 1$ (second column).

5.4 The linear stability analysis

The stability of the nonlocal solitons have been analyzed by employing Bogoliobov-De-Genes (BDG) equations. The nonlocal solitons are slightly perturbing such that:

$$\begin{aligned}
\Psi_1 &= (U(x) + r_1(x)e^{i\lambda z} + s_1(x)e^{-i\lambda^* z})e^{-i\mu z}, \\
V_{NL1} &= V^{\mu}_{NL1}(x,z) + \Delta V_{NL1}(x,z), \\
\Psi_2 &= (U(x) + r_2(x)e^{i\lambda z} + s_2(x)e^{-i\lambda^* z})e^{-i\mu z}, \\
V_{NL2} &= V^{\mu}_{NL2}(x,z) + \Delta V_{NL2}(x,z).
\end{aligned} \tag{5.15}$$

The linearizing Equations 5.7-5.10:

$$\lambda r_1 = (L_1 + iG + UDU^*)r_1 + UDUs_1^* + (C_{th} - iG)r_2, \tag{5.16}$$

$$\lambda s_1^* = (-L_1 + iG - U^*DU)s_1^* - U^*DU^*r_1 - (C_{th} + iG)s_2^*, \tag{5.17}$$

$$\lambda r_2 = (L_1 - iG + UDU^*)r_2 - UDUs_2^* + (C_{th} + iG)r_1, \tag{5.18}$$

$$\lambda s_2^* = (-L_1 - iG - U^*DU)s_2^* - U^*DU^*r_2 - (C_{th} - iG)s_1^*, \tag{5.19}$$

being $L_1 = \partial_x^2 + V_r Sin^2(x) + \mu + D|U|^2$ and $D = (1 - \sigma\partial_x^2)^{-1}$. The set of Equations 5.16-5.19 is solved employing pseudo-spectral method. The diffraction and D operators, and the potential V_R are evaluated using Chebyshev polynomials. We have studied the linear stability of high-frequency as well as the low-frequency modes.

The nature of the eigenvalue λ determines the stability of the solution. The solution is stable for real values of λ. The complex values of λ leads to the oscillatory instability of the solution. Purely imaginary positive or negative eigenvalues represent exponentially decaying or growing modes respectively.

We have studied the perturbation eigenvalues as functions of μ. Figure 5.5 shows stability plots of high-frequency and low-frequency modes for various range of nonlocal nonlinearity. Figure 5.5(a) illustrates that imaginary part of the perturbation eigenvalues are negligible comparing with the real part and so the high-frequency modes for weak nonlocality are linearly stable. As σ increases both the real part and the imaginary part are comparable as shown in Figure 5.5(b). The perturbation modes decay exponentially. Hence high-frequency modes are unstable and exhibit oscillatory instability. The low-frequency modes are stable for weak nonlocality whereas unstable for strong nonlocality as evident from Figures 5.5(c) and 5.5(d) respectively.

The linear stability analysis of the single-hump high-frequency and low-frequency modes of nonlocal coupler have been studied for various strength of the transverse potential with strong nonlocal nonlinearity. Figures 5.6(a) and 5.6(b) illustrate that the high-frequency modes are unstable with oscillatory in-

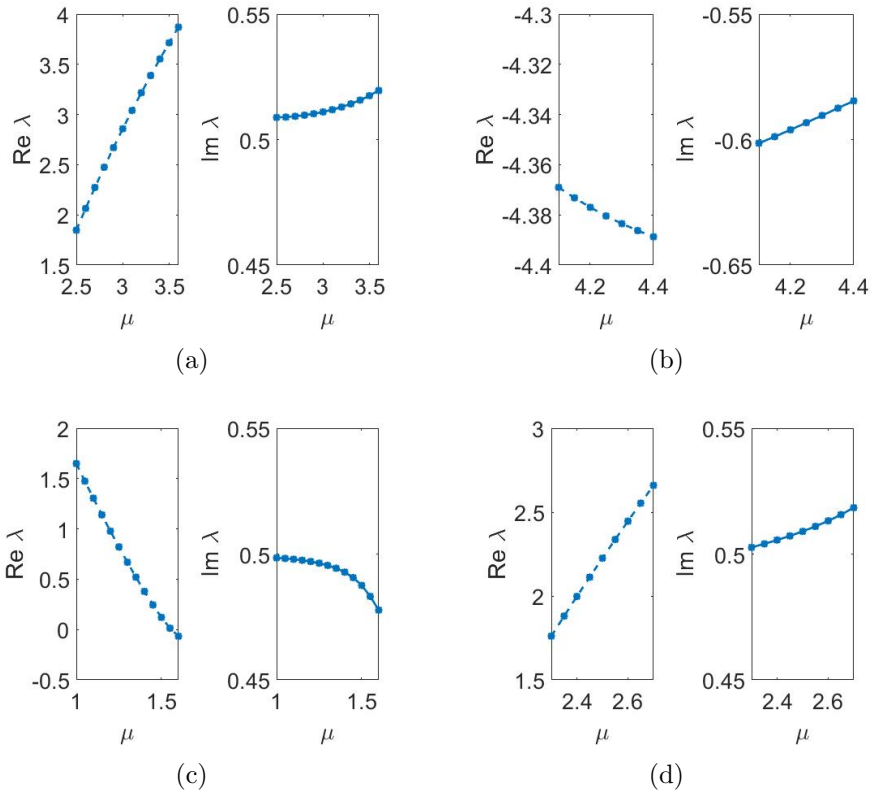

Figure 5.6: The linear stability analysis of single-hump high-frequency (first row) and low-frequency (second row) modes nonlocal coupler for $C = 1$, $G = 0.5$, and $\sigma = 1.0$ with $V_r = 1$ (first column) and $V_r = 2$ (second column).

stability for $V_r = 1$ and $V_r = 2$. The perturbation modes decay exponentially for low strength of the potential whereas grow exponentially for high strength of the potential. However the low-frequency perturbation modes decay exponentially for any strength of the potential as it is evident from Figures 5.6(c) and 5.6(d). The low-frequency modes are unstable. Hence the strength of the potential does not affect the stability of the high-frequency and low-frequency modes.

5.5 The propagation dynamics

We have employed the semi-analytical method to study the propagation of high-frequency and low-frequency modes. When $\Phi_1 = \Phi_2 = \Phi$, equations 5.7-5.10

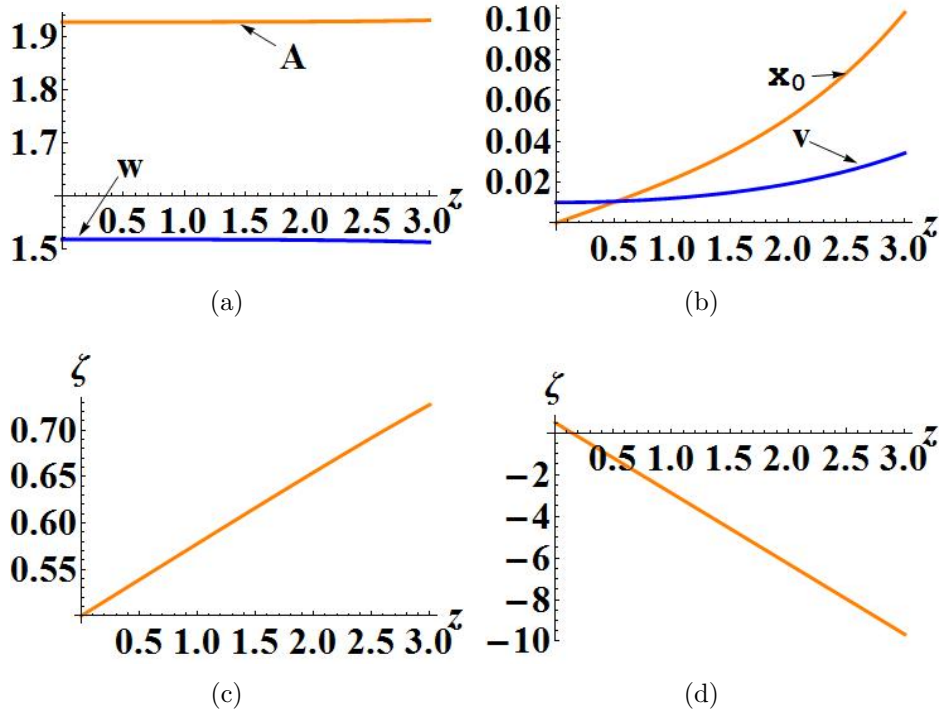

Figure 5.7: The propagation dynamics of high-frequency and low-frequency modes along the propagation direction for $C = 1$, $G = 0.5$, $V_r = 1.0$ and $\sigma = 1.0$. (a) The amplitude (A) and the width (w), (b) the center of mass (x_0) and velocity v, (c) the phase (ζ) of the high-frequency, and (d) the phase (ζ) of the low-frequency.

reduced to the form:

$$i\Phi_z + \mu\Phi + \Phi_{xx} + (V_R(x) + V_{NL})\Phi + C_{th}\Phi = 0, \tag{5.20}$$

$$V_{NL} - \sigma\frac{\partial^2 V_{NL}}{\partial x^2} = |\Phi|^2, \tag{5.21}$$

where C_{th} as defined in Equation 5.12. The Lagrangian density of the system is obtained as:

$$\mathcal{L}_{\mathcal{C}} = \frac{i}{2}(\Phi_z^*\Phi - \Phi^*\Phi_z) + |\Phi_x|^2 - \mu|\Phi|^2 - V_R(x)|\Phi|^2 - CCos(\delta)|\Phi|^2 \\ -V_{NL}(x)|\Phi|^2 + \frac{\sigma}{2}(\frac{\partial V_{NL}}{\partial x})^2 + \frac{V_{NL}^2}{2}. \tag{5.22}$$

The variational ansatz is assumed as:

$$\Phi(x,z) = A(z)e^{[\frac{-(x-x_0(z))^2}{2w(z)^2} + iv(z)x + i\zeta(z)]}, \tag{5.23}$$

where the amplitude $A(z)$, the width $w(z)$, the velocity $v(z)$, the center of mass $x_0(z)$ and the phases $\zeta(z)$ are the variational parameters. The nonlocal nonlinearity is of the form [8]:

$$V_{NL}(x,z) = A_{NL}(z)Exp[\frac{-(x-x_0(z))^2}{2w_{NL}^2(z)}], \tag{5.24}$$

where A_{NL}, and w_{NL} are the amplitude and the width of the nonlocal nonlinearity. In terms of power $p = \sqrt{\pi}A^2w$, the effective Lagrangian is given by:

$$\begin{aligned} < L_C >= v_z x_0 p + \zeta_z p + \frac{p}{2w^2} + v^2 p - \mu p - 0.5V_r p(1 - e^{-w^2}Cos(2x_0)) \\ -\frac{\sqrt{2}w_{NL}A_{NL}p}{\sqrt{2w_{NL}^2 + w^2}} - 2CCos(\delta)\sqrt{p} + \frac{\sqrt{\pi}w_{NL}A_{NL}^2}{2}(1 + \frac{\sigma}{2w_{NL}^2}). \end{aligned} \tag{5.25}$$

The variational equations are obtained as:

$$p_z = 0, \tag{5.26}$$

$$x_{0z} = 2v, \tag{5.27}$$

$$\begin{aligned} \zeta_z = -V_r x_0 e^{-w^2}Sin(2x_0) + \mu - v^2 + 0.5V_r(1 - e^{-w^2}Cos(2x_0)) - \frac{1}{2w^2} \\ +CCos(\delta) - \frac{\sqrt{2}w_{NL}A_{NL}}{\sqrt{2w_{NL}^2 + w^2}}, \end{aligned} \tag{5.28}$$

$$v_z = V_r sin(2x_0)e^{-w^2}, \tag{5.29}$$

$$A_{NL} = \frac{2\sqrt{2}w_{NL}^2 p}{(\sigma + 2w_{NL}^2)\sqrt{\pi 2w_{NL}^2 + w^2}}, \tag{5.30}$$

$$\frac{1}{w^3} + V_r w e^{-w^2}Cos(2x_0) - \frac{\sqrt{2}w_{NL}wA_{NL}}{(2w_{NL}^2 + w^2)^{1.5}} = 0, \tag{5.31}$$

$$w_{NL}^2 = \frac{\sigma + w^2 + \sqrt{(\sigma + w^2)^2 + 12\sigma w^2}}{4}. \tag{5.32}$$

The solutions of equations 5.26-5.32 yield the dynamics of high-frequency ($Cos(\delta) > 0$) and low-frequency ($Cos(\delta) < 0$) modes.

We have studied the variation of center of mass (x_0), velocity (v), width (w), and the amplitude (A) of the modes along the propagation direction. Figure 5.7(a) illustrates that both modes have constant amplitude and width, thereby

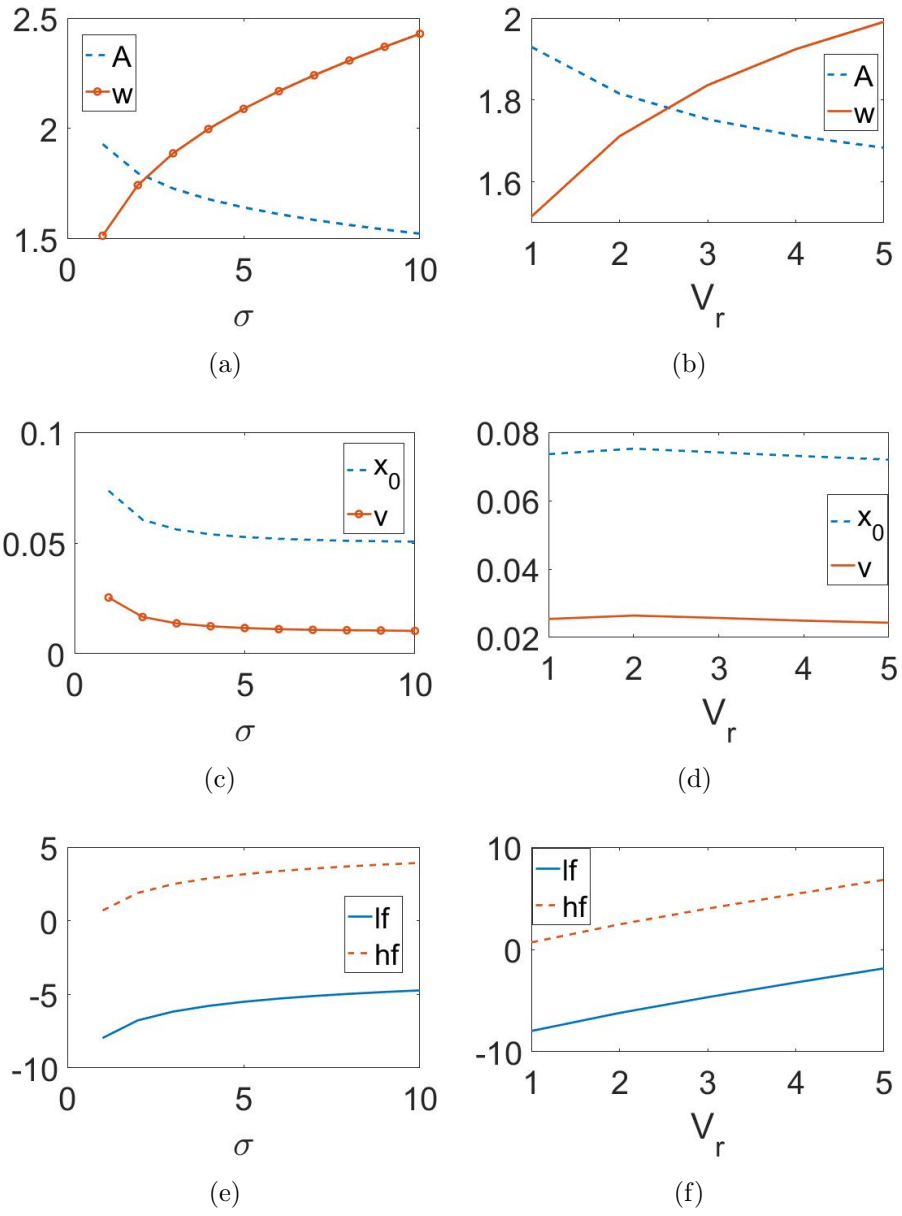

Figure 5.8: The nature of high-frequency and low-frequency modes for varying σ (first column) and V_r (second column) with parameter values $C = 1$, $G = 0.5$, and $V_r = 1$. (a) and (b) The amplitude (A) and width (w), (c) and (d) the center of mass (x_0) and velocity (v), (e) and (f) the phases (ζ) of high-frequency (hf) and low-frequency (lf) modes.

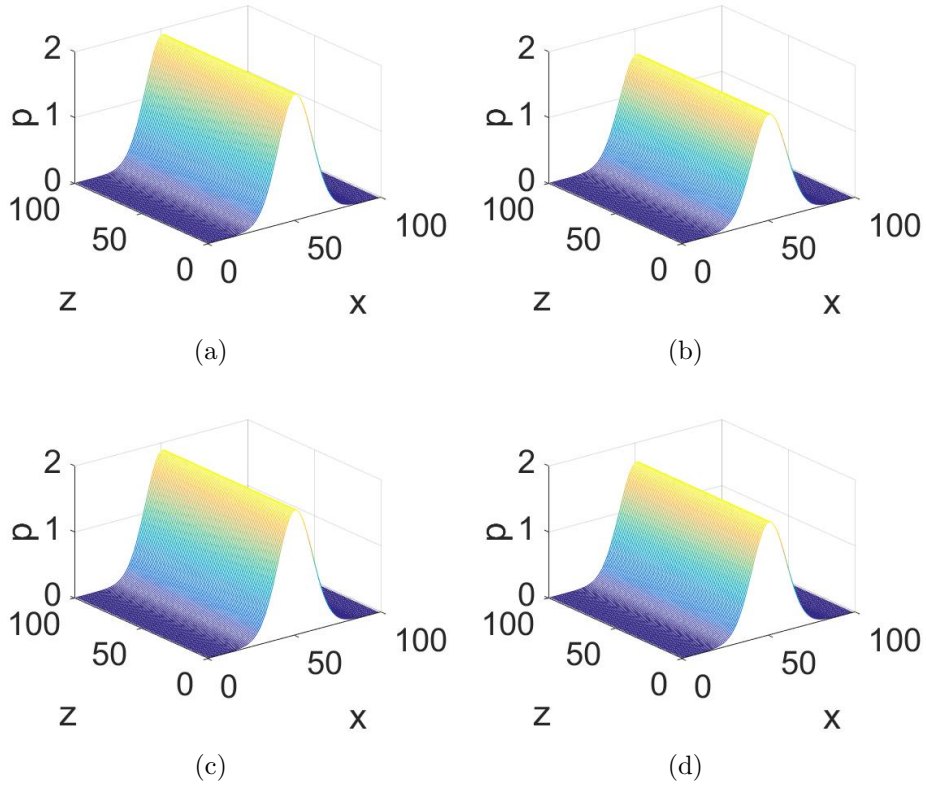

Figure 5.9: The beam propagation for $C = 1$ and $G = 0.5$. First row for $V_r = 1$ by varying σ: (a) $\sigma = 1$ and (b) $\sigma = 5$. Second row for $\sigma = 2$ by varying V_r: (c) $V_r = 1$ and (d) $V_r = 2$.

producing constant power as found from equation 5.26. The center of mass and velocity increase as shown in Figure 5.7(b). The phase of the high-frequency mode increases as it propagates, whereas that of the low-frequency mode decreases as shown in Figures 5.7(c) and 5.7(d) respectively.

The dynamics of both modes have been studied by varying σ and V_r. When σ increases, the widths of both modes increase whereas the amplitudes decrease as shown in Figure 5.8(a). The center of mass and velocity decrease for low values of σ and becomes constant as σ increases as depicted in Figure 5.8(c). Figure 5.8(e) shows that the phases of both modes increase with σ. As V_r increases, the amplitude decreases whereas the width increases as depicted in Figure 5.8(b). The center of mass x_0, and the velocity v slightly oscillate as plotted in Figure 5.8(d). Figure 5.8(f) illustrates that the phases of the high-frequency and the low-frequency modes increase with V_r.

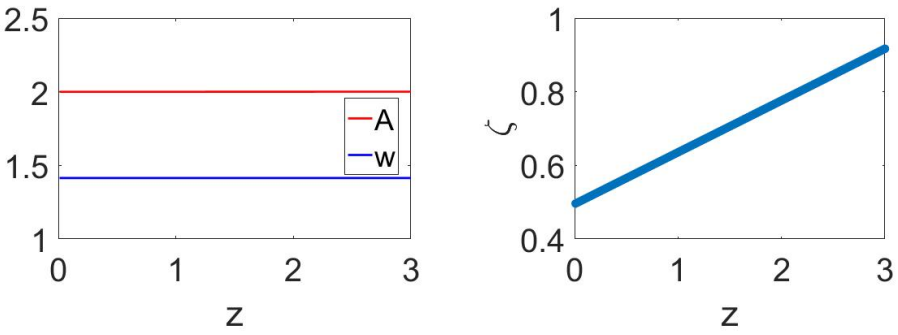

(a) (b)

Figure 5.10: The beam propagation for $C = 1$, $V_r = 1$, $\sigma = 1$ and $G = 0.5$. (a) The amplitude and the width, and (b) the phase of high-frequency mode.

Equations 5.20 and 5.21 have been studied numerically using finite difference method by varying σ and V_r. When σ and V_r change, the beam propagates with constant power as depicted in Figures 5.9(a)-5.9(d).

Figure 5.10(a) shows that the amplitude and the width remain constant along the propagation direction for fixed values of σ and V_r. The corresponding phase of the high-frequency mode is shown in Figure 5.10(b). These results agree with the variational analysis.

5.6 Conclusion

The nonlocal gap solitons of $\mathcal{PT}$ symmetric coupler with transverse real periodic potential having defocusing nonlocal nonlinearity have been investigated. The propagation invariant solutions of the system has been studied and found that high-frequency and low-frequency modes coexist in the system as far as the gain/loss coefficient is less than the coupling coefficient. The high-frequency and the low-frequency modes with single-hump, double-hump and triple-hump structures are obtained. The high-frequency multi-hump modes are observed in the first band gap. The low-frequency single-hump modes lie in the semi-infinite band gap whereas low-frequency double-hump and triple-hump modes lie in the first band gap. The single-hump modes trap in the minimum of the potential.

The double-hump modes spread through the two consecutive lattice while triple-hump modes lie across three consecutive lattices. As the range of the nonlocal nonlinearity varies, the propagation constants corresponding to different modes also change. When the propagation constant increases, the power of the high-frequency and low-frequency single-hump modes increases. However increase in the gain/loss coefficient results increase in the power of high-frequency modes whereas decrease in the power of low-frequency modes. The linear stability analysis of the high-frequency and low-frequency modes predict that both modes are stable for weak nonlocality while unstable with oscillatory instability for strong nonlocality. The studies on the propagation dynamics reveal that when the range of the nonlocality increases, the width increases and the amplitude decreases, resulting constant power propagation. The switching dynamics of the coupler with Kerr and nonlocal nonlinearity has been discussed in chapter 6.

Bibliography

[1] L.Safaei and M.B.Zarndi and M.Hatami. PT-symmetric nonlinear directional fiber couplers with gain and loss for ultrashort optical pulses. J Laser Opt Photonics 2017;4:155.

[2] M.gren and F.Kh.Abdullaev and V.V.Konotop. Solitons in a PT-symmetric (2) coupler. Optics Letters. 2017;42:20 4079-4082.

[3] L.Gubeskys and B.A.Malomed. Symmetric and asymmetric solitons in dual-core couplers with competing quadratic and cubic nonlinearities. J.Opt.Soc.Am.B 2013;30:7 1843-1852.

[4] G.Burlak and S.Garcia-Paredes and B.A.Malomed. PT-symmetric couplers with competing cubic-quintic nonlinearities. Chaos. 2016;26:113103.

[5] X.Shi and B.A.Malomed and F.Ye and X.Chen. Symmetric and asymmetric solitons in a nonlocal nonlinear coupler. Phys. Rev. A. 2012;85:053839.

[6] Y.L.Dang and H.J.Li and J.Lin. Soliton solutions in nonlocal nonlinear coupler. Nonlinear Dynamics. 2016;88:1 1-13.

[7] K.A.Muhsina and P.A.Subha. Soliton beam dynamics in parity-time symmetric nonlinear coupler. Eur.Phys.J.D. 2015;69:7 17.

[8] C.P.Jisha and A.Alberucci and V.A.Brazhnyi and G.Assanto. Nonlocal gap solitons inpt-symmetric periodic potentials with defocusing nonlinearity. Phys Rev A 2014;89:013812.

SUNEERA T. P. “STUDIES ON BEAM DYNAMICS IN SINGLE AND COUPLED PARITY-TIME SYMMETRIC SYSTEMS WITH KERR AND NONLOCAL NONLINEARITY”. THESIS. DEPARTMENT OF PHYSICS, UNIVERSITY OF CALICUT, 2018.

Chapter 6

Switching dynamics of $\mathcal{PT}$ symmetric coupled systems

6.1 Introduction

The inventions of lasers and the optical fibers revolutionize the communication system and the data transfer. The basic building blocks of photonic circuitry needs couplers, switches, isolators and diodes which can replace the role of electrons with photons. Optical transistors has been introduced as the basic elements of photonic logic gates [1]. The bistable switching in optical transistors with photonic crystals has been reported [2]. All-optical switching in optically induced nonlinear waveguide couplers has been experimentally demonstrated by Falko Diebel et.al [3]. Nonlinear switching has been reported on dual-core nonlinear optical fiber couplers with XPM and Raman intra-pulse applied to femto-second pulse propagation [4].

$\mathcal{PT}$ symmetric couplers act as unidirectional valves by trapping the intensity in the gain channel. Ultrafast optical switching has been studied using $\mathcal{PT}$ symmetric Bragg gratings [5]. All-optical transistors and logic gates have been invented using $\mathcal{PT}$ symmetric Y-junctions [6]. Optimal $\mathcal{PT}$ symmetric switch features the exceptional point has been reported [7].

In this chapter, we have described the switching dynamics in $\mathcal{PT}$ symmetric coupler with nonlocal nonlinearity having transverse periodic and aperiodic potentials. The propagation dynamics of a $\mathcal{PT}$ symmetric nonlocal coupler and the nonlinear switching have been addressed.

6.2 The propagation dynamics

We have studied the $\mathcal{PT}$ symmetric coupler having transverse real potential $V(x) = V_R(x)$ with defocusing nonlocal nonlinearity. The system has been modeled by modifying the coupled nonlinear Schrödinger equation (NLSE):

$$i\Psi_{1z} + \Psi_{1xx} + (V_R(x) + iG + V_{NL1})\Psi_1 + C\Psi_2 = 0, \tag{6.1}$$

$$V_{NL1} - \sigma\frac{\partial^2 V_{NL1}}{\partial x^2} = |\Psi_1|^2, \tag{6.2}$$

$$i\Psi_{2z} + \Psi_{2xx} + (V_R(x) - iG + V_{NL2})\Psi_2 + C\Psi_1 = 0, \tag{6.3}$$

$$V_{NL2} - \sigma\frac{\partial^2 V_{NL2}}{\partial x^2} = |\Psi_2|^2, \tag{6.4}$$

where the subscript z represents the first derivative with respect to the propagation direction z (in normalised unit) and subscript xx implies the second derivative with respect to transverse direction x. Ψ_1 and Ψ_2 are the electric fields in the channels with gain and loss respectively. The nonlocal nonlinearity in the gain channel is denoted by V_{NL1} and that of lossy channel by V_{NL2}. The range of the nonlocal nonlinearity is denoted by σ, with $\sigma > 0$ for defocusing and $\sigma < 0$ for self-focusing nonlinearities. $\sigma = 0$ corresponds to the Kerr nonlinearity. C represents the coupling coefficient and G denotes the gain/loss coefficient. When the gain in one channel is compensated by equal loss in other channel, the coupler is in $\mathcal{PT}$ symmetric regime. We have explored the $\mathcal{PT}$ symmetric nonlocal coupler with the periodic and the aperiodic transverse potentials, which have the following form:-

(1) The periodic potential $V_R(x) = V_r sin^2(x)$, of period π and the strength V_r, and

(2) The aperiodic potential $V_R(x) = V_0 x^2$ with the strength V_0.

The solutions of the system Ψ_1 and Ψ_2, satisfy the following equations:

$$\Psi_1(z,x) = \Phi_1(x,z)e^{i\mu z}, \tag{6.5}$$

$$\Psi_2(z,x) = \Phi_2(x,z)e^{i\mu z}, \tag{6.6}$$

μ being the propagation constant. The modeled equations 6.1-6.4 have been rewritten as:

$$i\Phi_{1z} - \mu\Phi_1 + \Phi_{1xx} + (V_R(x) + iG + V_{NL1})\Phi_1 + C\Phi_2 = 0, \tag{6.7}$$

$$V_{NL1} - \sigma\frac{\partial^2 V_{NL1}^2}{\partial x^2} = |\Phi_1|^2, \tag{6.8}$$

$$i\Phi_{2z} - \mu\Phi_2 + \Phi_{2xx} + (V_R(x) - iG + V_{NL2})\Phi_2 + C\Phi_1 = 0, \tag{6.9}$$

$$V_{NL2} - \sigma\frac{\partial^2 V_{NL2}^2}{\partial x^2} = |\Phi_2|^2. \tag{6.10}$$

Equations 6.7-6.10 have been analyzed by employing the variational and numerical methods to study the propagation dynamics and the nonlinear switching of the system.

The Lagrangian density of Equations 6.7-6.10 is expressed as:

$$\begin{aligned}\mathcal{L}_{\mathcal{C}} = {} & \frac{i}{2}(\Phi_{1z}^*\Phi_1 - \Phi_1^*\Phi_{1z}) + \frac{i}{2}(\Phi_{2z}^*\Phi_2 - \Phi_2^*\Phi_{2z}) + |\Phi_{1x}|^2 + |\Phi_{2x}|^2 + \mu|\Phi_1|^2 \\ & + \mu|\Phi_2|^2 - V_R(x)(|\Phi_1|^2 + |\Phi_2|^2) - C(\Phi_1^*\Phi_2 + \Phi_2^*\Phi_1) - V_{NL1}(x)|\Phi_1|^2 \\ & - V_{NL2}(x)|\Phi_2|^2 + \frac{\sigma}{2}[(\frac{\partial V_{NL1}}{\partial x})^2 + (\frac{\partial V_{NL2}}{\partial x})^2] + \frac{V_{NL1}^2 + V_{NL2}^2}{2},\end{aligned} \tag{6.11}$$

$$\mathcal{L}_{\mathcal{NC}} = -iG[|\Phi_1|^2 - |\Phi_2|^2], \tag{6.12}$$

where $\mathcal{L}_{\mathcal{C}}$ and $\mathcal{L}_{\mathcal{NC}}$ being conservative and nonconservative components of the Lagrangian density respectively.

The trial solution has been assumed as:

$$\Phi_j(x,z) = A_j(z)Exp[\frac{-(x - x_0(z))^2}{2w(z)^2} + iv(z)x + i\theta_j(z)], \tag{6.13}$$

where the index $j = 1, 2$ indicates the gain and lossy channels respectively. The amplitudes $A_j(z)$, the width $w(z)$, the velocity $v(z)$, the center of mass $x_0(z)$

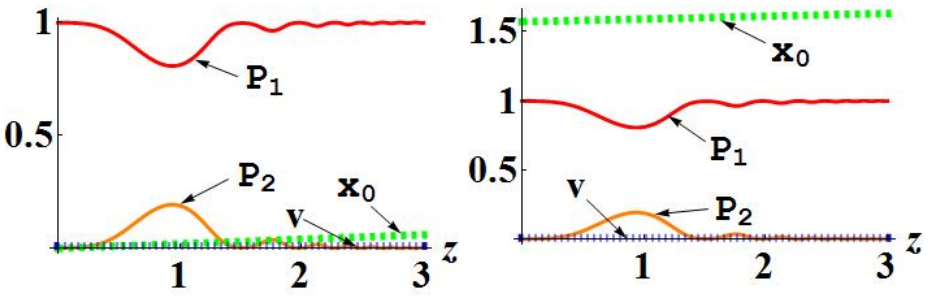

(a)

(b)

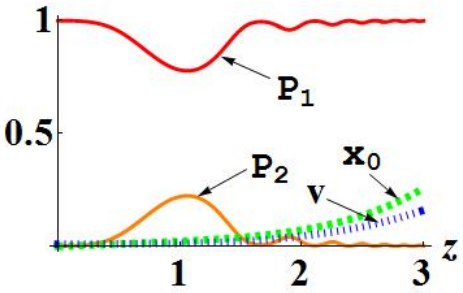

(c)

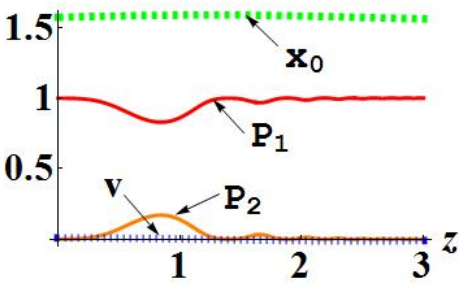

(d)

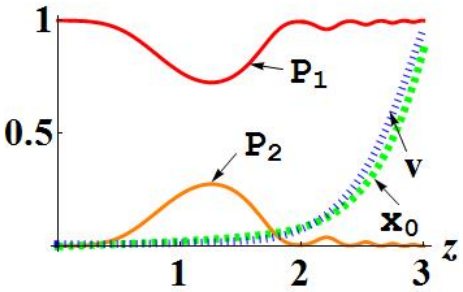

(e)

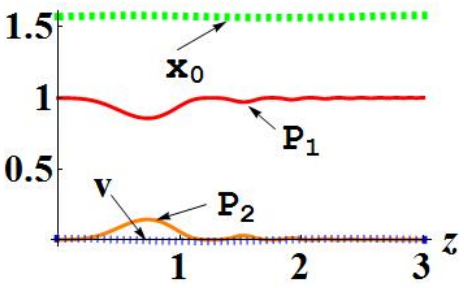

(f)

Figure 6.1: The variational results of the nonlinear coupler with transverse periodic potential for various values of V_r with $C = 1$, $\sigma = 1$ and $G = 0.5$. The initial conditions are $p_1 = 6.0$, $p_2 = 0.01$, $v = 0.01$, $\theta_1 = 0.5$, and $\theta_2 = 0.5$. (a) $V_r = 0$, $x_0 = 0$, (b) $V_r = 0$, $x_0 = \frac{\pi}{2}$, (c) $V_r = 1$, $x_0 = 0$, (d) $V_r = 1$, $x_0 = \frac{\pi}{2}$, (e) $V_r = 4$, $x_0 = 0$ and (f) $V_r = 4$, $x_0 = \frac{\pi}{2}$.

and the phases $\theta_j(z)$ are the variational parameters. The nonlocal nonlinearity has been selected as:

$$V_{NLj}(x,z) = A_{NLj}(z)Exp[\frac{-(x-x_0(z))^2}{2w_{NL}^2(z)}], \tag{6.14}$$

A_{NLj} being the amplitude of the nonlocal nonlinearity and w_{NL} being the common width of the nonlocal nonlinearity.

The input power P is distributed between the channels such that $P = p_1 + p_2$ where $p_1 = \int_{-\infty}^{\infty} |\Phi_1|^2 dx$ and $p_2 = \int_{-\infty}^{\infty} |\Phi_2|^2 dx$. The relative power is defined as the ratio of the power of single channel to the total power $P = p_1 + p_2$ which is expressed as:

$$P_1 = \frac{p_1}{P}, \qquad P_2 = \frac{p_2}{P}. \tag{6.15}$$

for gain and loss channels respectively.

Case:1 The periodic potential

The effective Lagrangian of the nonlocal coupler with the transverse periodic potential $V_r(x) = V_r sin^2(x)$ is given by:

$$\begin{aligned} < L_C > = {} & v_z x_0(p_1+p_2) + \theta_{1z}p_1 + \theta_{2z}p_2 + \frac{p_1+p_2}{2w^2} + v^2(p_1+p_2) + \mu(p_1+p_2) \\ & -0.5V_r(p_1+p_2)(1-e^{-w^2}Cos(2x_0)) - \frac{\sqrt{2}w_{NL}(A_{NL1}p_1 + A_{NL2}p_2)}{\sqrt{2w_{NL}^2+w^2}} \\ & -2CCos(\delta)\sqrt{p_1p_2} + \frac{\sqrt{\pi}w_{NL}(A_{NL1}^2 + A_{NL2}^2)}{2}(1+\frac{\sigma}{2w_{NL}^2}). \end{aligned} \tag{6.16}$$

The variational equations of the coupled system are given by:

$$p_{1z} = 2CSin(\delta)\sqrt{p_1p_2} + 2Gp_1, \tag{6.17}$$

$$p_{2z} = -2CSin(\delta)\sqrt{p_1p_2} - 2Gp_2, \tag{6.18}$$

$$x_{0z} = 2v, \tag{6.19}$$

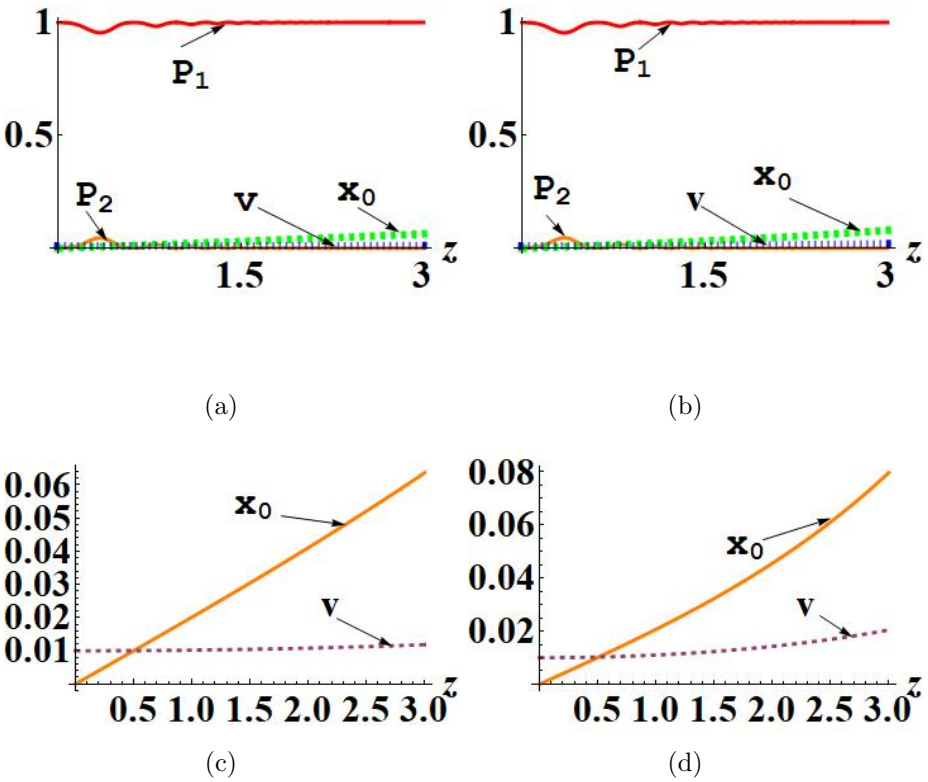

Figure 6.2: The variational results for the nonlocal coupler with transverse aperiodic potential. The variation of x_0, v and P_i along z with $C = 1$, $\sigma = 1.0$ and $G = 0.5$ with the initial conditions $v = 0.01$, $\theta_1 = 0.5$, and $\theta_2 = 0.5$. (a) $V_0 = 0.01$, (b) $V_0 = 0.05$. (c)x_0 and v as functions of z for $V_0 = 0.01$, and (d) x_0 and v versus z for $V_0 = 0.05$.

$$\theta_{1z} = -V_r x_0 e^{-w^2} Sin(2x_0) + 0.5V_r(1 - e^{-w^2} Cos(2x_0)) + \mu - v^2 - \frac{1}{2w^2} + \sqrt{\frac{p_2}{p_1}} CCos(\delta) + \frac{\sqrt{2} w_{NL} A_{NL1}}{\sqrt{2w_{NL}^2 + w^2}}, \tag{6.20}$$

$$\theta_{2z} = -V_r x_0 e^{-w^2} Sin(2x_0) + 0.5V_r(1 - e^{-w^2} Cos(2x_0)) + \mu - v^2 - \frac{1}{2w^2} + \sqrt{\frac{p_1}{p_2}} CCos(\delta) + \frac{\sqrt{2} w_{NL} A_{NL2}}{\sqrt{2w_{NL}^2 + w^2}}, \tag{6.21}$$

$$v_z = V_r sin(2x_0) e^{-w^2}, \tag{6.22}$$

$$A_{NL1} = \frac{2\sqrt{2} w_{NL}^2 p_1}{(\sigma + 2w_{NL}^2)\sqrt{\pi(2w_{NL}^2 + w^2)}}, \tag{6.23}$$

$$A_{NL2} = \frac{2\sqrt{2} w_{NL}^2 p_2}{(\sigma + 2w_{NL}^2)\sqrt{\pi(2w_{NL}^2 + w^2)}}, \tag{6.24}$$

$$\frac{p_1 + p_2}{w^3} + V_r w e^{-w^2} Cos(2x_0)(p_1 + p_2) - \frac{\sqrt{2} w_{NL} w (A_{NL1} p_1 + A_{NL2} p_2)}{(2w_{NL}^2 + w^2)^{1.5}} = 0, \tag{6.25}$$

$$w_{NL}^2 = \frac{\sigma + w^2 + \sqrt{(\sigma + w^2)^2 + 12\sigma w^2}}{4}. \tag{6.26}$$

We have studied equations 6.17-6.26 numerically by exciting the channel with gain (i.e., channel 1) for high input power. The variation of x_0, v, and P_j along the propagation direction are plotted in Figures 6.1(a)-6.1(f) with strong nonlocality (i.e, $\sigma = 1$) by varying the strength of the potential. In the absence of the transverse potential, the soliton moves with constant v and increasing x_0 as depicted in Figures 6.1(a) and 6.1(b) with the relative power nearly one in channel 1 and nearly zero in channel 2. The presence of the potential varies v and x_0. When the strength of the transverse potential is low and x_0 is initially at the minimum of the potential, as the soliton evolves v and x_0 increase linearly with z as shown in Figure 6.1(c). It means that the solution is a travelling soliton. But if x_0 is initially at the maximum of the potential, v and x_0 slightly oscillate representing trapped soliton as plotted in Figure 6.1(d). Figures 6.1(e) and 6.1(f) are plotted for high V_r. From Figure 6.1(e), it is evident that v and x_0 increase nonlinearly with z if initially x_0 lies at the minimum of the potential. The solution is a trapped soliton with slightly oscillating v and x_0, if x_0 lies initially at the maximum of the potential as shown in Figure 6.1(f). Depending on the initial position of the solution, it behaves like the travelling soliton or the trapped soliton.

Case:2 The aperiodic potential

The effective Lagrangian of the system with transverse aperiodic potential $V_R(x) = V_0 x^2$, is obtained as:

$$
\begin{aligned}
&< L_C >= v_z x_0(p_1+p_2) + \theta_{1z}p_1 + \theta_{2z}p_2 + \frac{p_1+p_2}{2w^2} + v^2(p_1+p_2) \\
&- 0.5V_r(p_1+p_2)(w^2+x_0^2) - \frac{\sqrt{2}w_{NL}(A_{NL1}p_1 + A_{NL2}p_2)}{\sqrt{2w_{NL}^2+w^2}} + \mu(p_1+p_2) \\
&- 2CCos(\delta)\sqrt{p_1p_2} + \frac{\sqrt{\pi}w_{NL}(A_{NL1}^2 + A_{NL2}^2)}{2}(1+\frac{\sigma}{2w_{NL}^2}).
\end{aligned} \tag{6.27}
$$

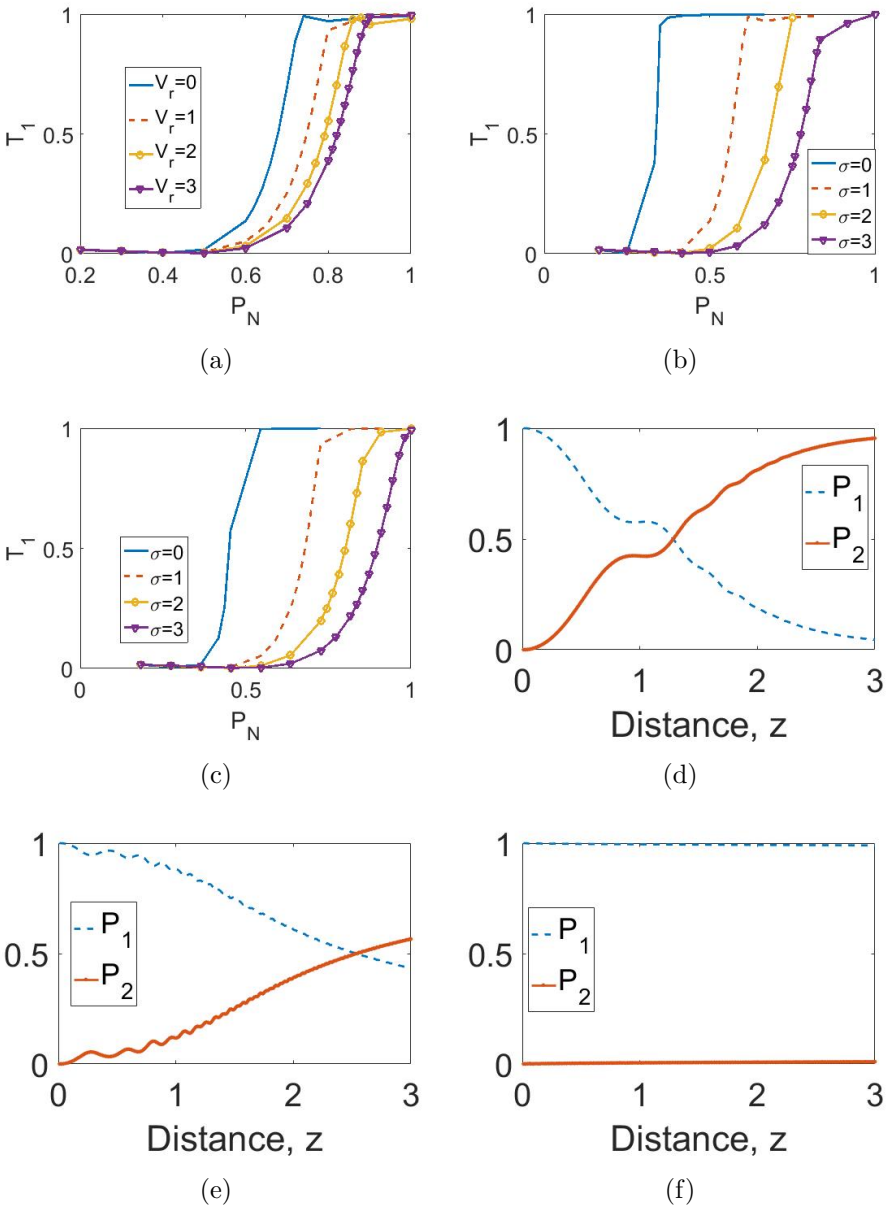

Figure 6.3: The power-dependent switching of the nonlinear coupler with transverse periodic potential for $C = 1$ and $G = 0.5$ with initial conditions $x_0 = 0.1$, $v = 0.01$, $\theta_1 = 0.5$, and $\theta_2 = 0.5$. The transmission coefficient of gain channel versus normalized input power in: (a) $\sigma = 1$, (b) $V_r = 0$, and (c) for $V_r = 1$. The direct simulation, the relative intensity along the propagation direction with $\sigma = 1$ and $V_r = 1$: (d) input power 2, nearly zero P_1 at z=2.5, (e) input power 8, $P_1 = 0.5$ at z=2.5, and (f) input power 120, $P_1 = 1$ at z=2.5.

The variational equations of the system are given by:

$$p_{1z} = 2CSin(\delta)\sqrt{p_1 p_2} + 2Gp_1, \tag{6.28}$$

$$p_{2z} = -2CSin(\delta)\sqrt{p_1 p_2} - 2Gp_2, \tag{6.29}$$

$$x_{0z} = 2v, \tag{6.30}$$

$$\theta_{1z} = 0.5V_0(p_1 + p_2)(w^2 - 2x_0^2) - \mu - v^2 - \frac{1}{2w^2} + \sqrt{\frac{p_2}{p_1}}CCos(\delta) + \frac{\sqrt{2}w_{NL}A_{NL1}}{\sqrt{2w_{NL}^2 + w^2}}, \tag{6.31}$$

$$\theta_{2z} = 0.5V_0(p_1 + p_2)(w^2 - 2x_0^2) - \mu - v^2 - \frac{1}{2w^2} + \sqrt{\frac{p_1}{p_2}}CCos(\delta) + \frac{\sqrt{2}w_{NL}A_{NL2}}{\sqrt{2w_{NL}^2 + w^2}}, \tag{6.32}$$

$$v_z = 2V_0 x_0, \tag{6.33}$$

$$A_{NL1} = \frac{2\sqrt{2}w_{NL}^2 p_1}{(\sigma + 2w_{NL}^2)\sqrt{\pi(2w_{NL}^2 + w^2)}}, \tag{6.34}$$

$$A_{NL2} = \frac{2\sqrt{2}w_{NL}^2 p_2}{(\sigma + 2w_{NL}^2)\sqrt{\pi(2w_{NL}^2 + w^2)}}, \tag{6.35}$$

$$\frac{p_1 + p_2}{w^3} + V_0 w[z](p_1 + p_2) - \frac{\sqrt{2}w_{NL}w(A_{NL1}p_1 + A_{NL2}p_2)}{(2w_{NL}^2 + w^2)^{1.5}} = 0, \tag{6.36}$$

$$w_{NL}^2 = \frac{\sigma + w^2 + \sqrt{(\sigma + w^2)^2 + 12\sigma w^2}}{4}. \tag{6.37}$$

We have solved equations 6.28-6.37 numerically and the solutions are plotted in Figures 6.2(a)-6.2(d). Figures 6.2(a) and 6.2(b) illustrate that when the input power is high, the power get trapped in the gain channel. The variation of x_0 and v along z is depicted in Figures 6.2(c) and 6.2(d). Figure 6.2(c) shows that x_0 increases linearly with z whereas v remains constant for low strength of the potential. Both x_0 and v increase along z for $V_0 = 0.004$ as plotted in Figure 6.2(d). The solution is a travelling soliton for the parabolic potential.

6.3 The nonlinear switching

The switching behaviour has been explored by varying the input power, the range of the nonlocal nonlinearity, and the strength of the transverse potentials.

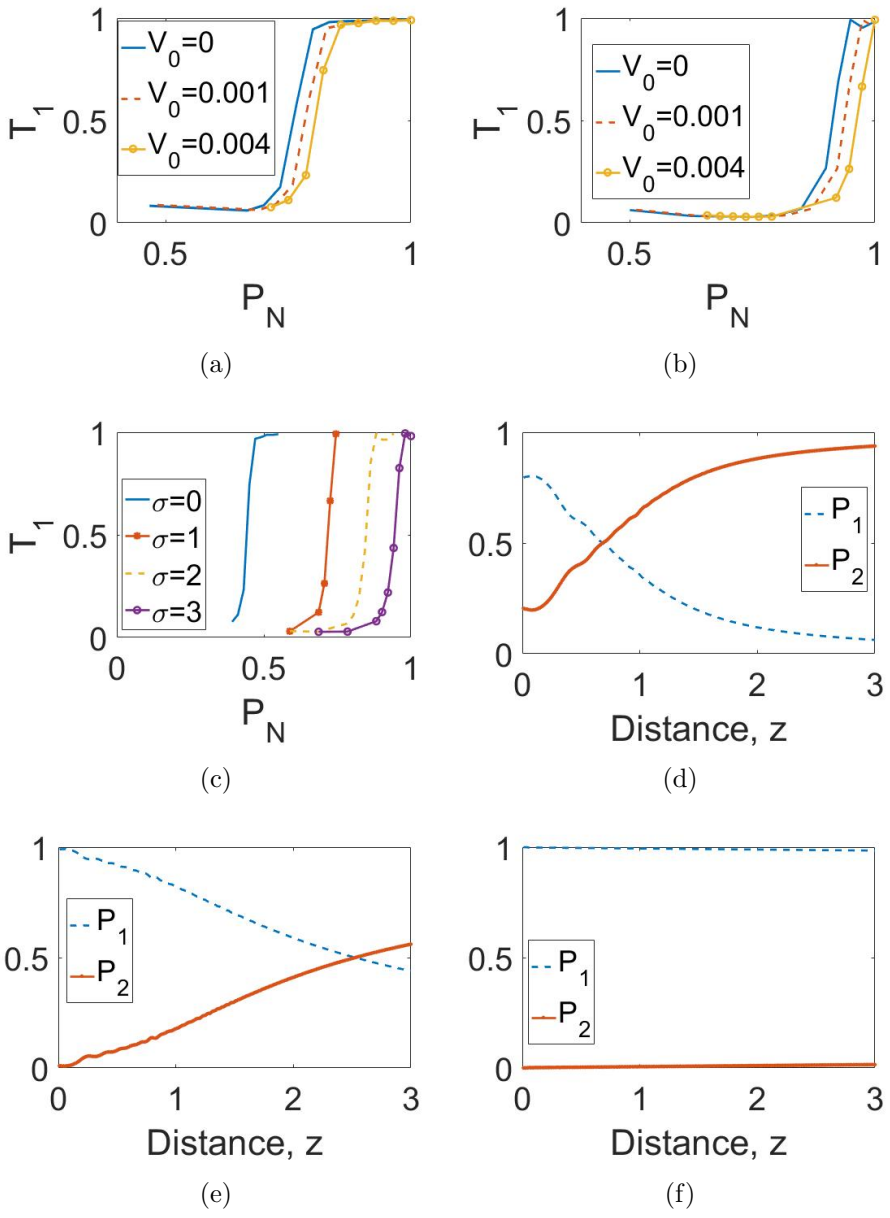

Figure 6.4: The switching behaviour of the nonlinear coupler with transverse aperiodic potential for $C = 1$ and $G = 0.5$ with initial conditions $x_0 = 0.1$, $v = 0.01$, $\theta_1 = 0.5$, $\theta_2 = 0.5$. First row: The transmission coefficient of gain channel versus normalized input power: (a) $\sigma = 0$, (b) $\sigma = 1$, and (c) $V_r = 0.004$. Second row: the direct simulation results for $\sigma = 1$ and $V_r = 0.004$: (d) input power 5, nearly zero P_1 at z=2.5, (e) input power 9, $P_1 = 0.5$ at z=2.5, and (f) input power 80, $P_1 = 1$ at z=2.5.

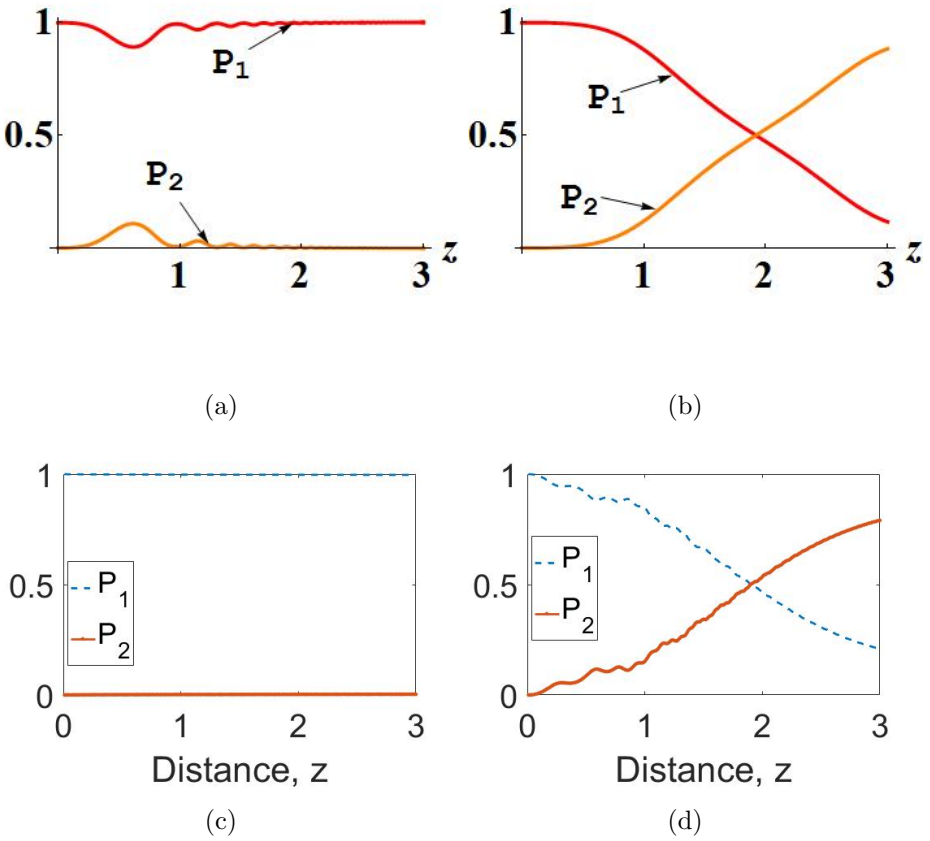

Figure 6.5: The nonlinear switching of coupler with transverse potential by varying σ for $V_r = 1$ with $C = 1$ and $G = 0.5$. The initial conditions are $v = 0.01$, $\theta_1 = 0.5$, and $\theta_2 = 0.5$. (a) $\sigma = 0.05$, and (b) $\sigma = 5$. Corresponding direct simulation results (c) and (d).

6.3.1 Varying input power

The propagation distance at which the entire power switches to the other channel is called the coupling length L_c. When the gain channel is excited, the power switches to the lossy channel at the coupling length for low input power, whereas the power get trapped in the gain channel for high input power. The transmission coefficient of the gain channel T_1 is defined as the ratio of the input power to the total power at the coupling length $z = L_c$. When the transmission coefficient is 0.5, the corresponding power is called the critical power P_r.

Case:1 The periodic potential

The variational equations 6.17-6.26 have been solved numerically and the switching behaviour has been plotted in Figures 6.3(a)-6.3(c) by varying V_r and σ. When V_r increases, P_r also increases for nonlocal coupler as depicted in Figure 6.3(a). It is evident that the presence of the potential results increase in P_r. Figures 6.3(b) and 6.3(c) illustrate that P_r increases with σ. The direct simulation of Equations 6.7-6.10 for the transverse periodic potential has been done using finite difference method. Figures 6.3(d), 6.3(e), and 6.3(f) show the variation of relative intensity as functions of z for different values of input power. For low input power, the input beam switches from gain to loss channel with T_1 nearly zero for coupling length (say, $z = 2.5$) as shown in Figure 6.3(d). Fifty percent of input power is transmitted to loss channel at coupling length for much more input power as depiced in Figure 6.3(e). The input power is completely trapped in the gain channel for high input power with T_1 nearly unity as illustrated in Figure 6.3(f).

Case: 2 Aperiodic potential

The variational equations 6.28-6.37 have been studied numerically and the power-dependent switching has been investigated by varying V_0 and σ. Figures 6.4(a) and 6.4(b) show that P_r increases with V_r for Kerr ($\sigma = 0$) and nonlocal coupler ($\sigma = 1$). Figure 6.4(c) reveals that when σ increases P_r increases. The direct simulation of Equations 6.7-6.10 with transverse aperiodic potential has been done by employing finite difference method. From Figures 6.4(d), 6.4(e) and 6.4(f), it is evident that as the power increases, T_1 increases from zero to unity. The variational results are in agreement with the results of the direct simulation.

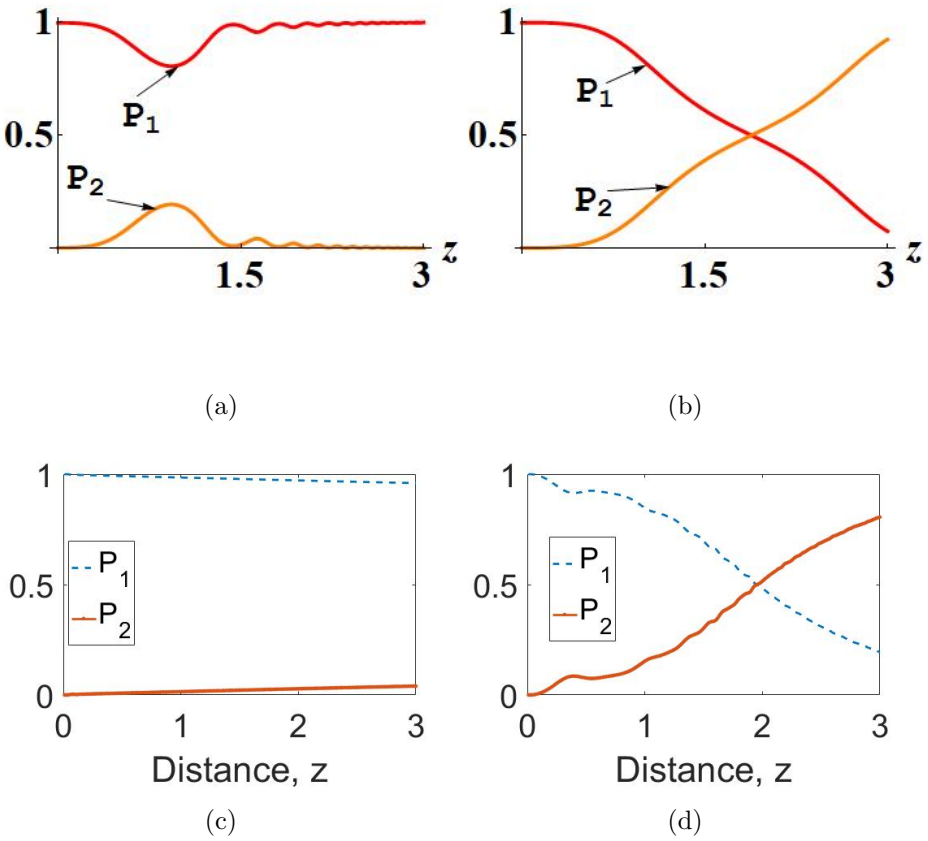

Figure 6.6: The nonlinear switching of coupler with transverse aperiodic potential by varying σ for $V_r = 1$ with $C = 1$ and $G = 0.5$. The initial conditions are $v = 0.01$, $\theta_1 = 0.5$, and $\theta_2 = 0.5$. (a) $\sigma = 0.05$ and (b) $\sigma = 2$. Corresponding direct simulation results are in (c) and (d).

6.3.2 Varying the range of the nonlocality

Case:1 The periodic potential

The nonlinear switching of the system has been studied numerically by solving Equations 6.17-6.26. In the case of $\mathcal{PT}$ symmetric nonlocal coupler, the input power is trapped in the gain channel for low values of V_r and σ with high input power as shown in 6.5(a). As σ increases, the power switches from gain channel to the lossy channel as depicted in 6.5(b). The direct simulation of equations 6.7-6.10 has been done and the results are plotted in Figures 6.5(c)-6.5(d). Both methods predict that it is possible to switch power from gain channel to lossy

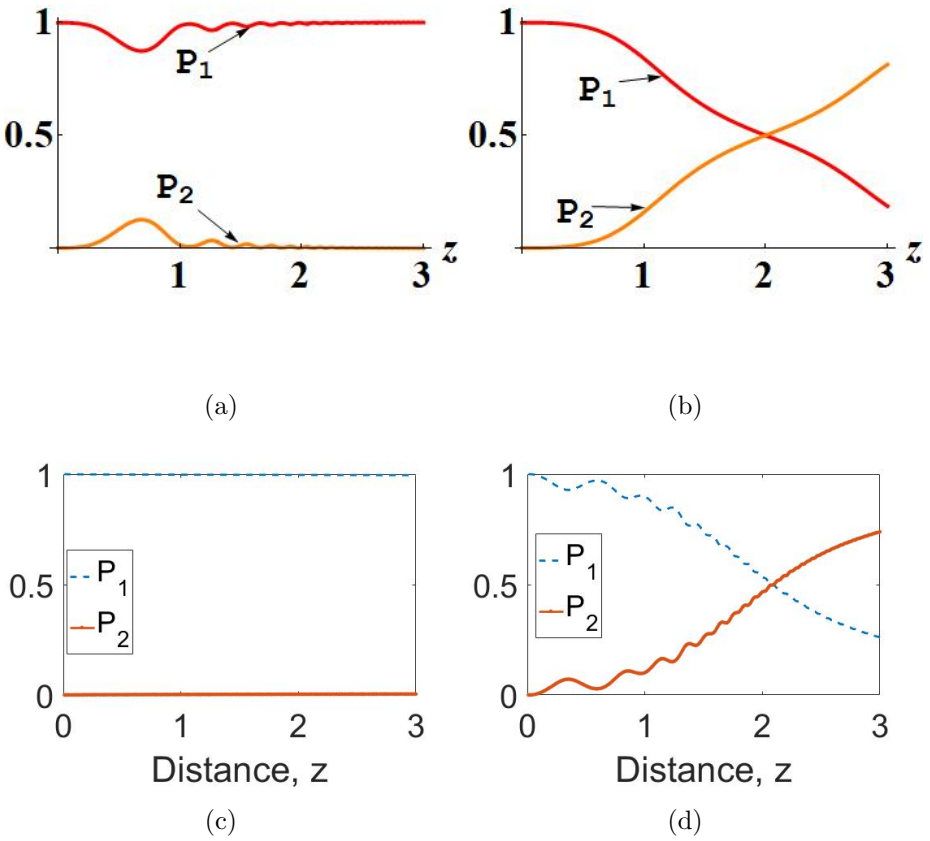

Figure 6.7: The nonlinear switching of the nonlocal coupler with transverse periodic potential varying V_r for $\sigma = 0.10$ and $P_1 = 6$. The variational results in (a) $V_r = 1$ and (b) $V_r = 10$. Corresponding direct simulation results in (c) and (d).

channel even for high input power by varying the range of the nonlocality.

Case:2 The aperiodic potential

The nonlinear switching of the system has been studied numerically by solving Equations 6.28-6.37. The input power is trapped in the gain channel for low values of σ as shown in Figure 6.6(a) with high input power. The power switches from gain channel to other as illustrated in Figure 6.6(b) by varying σ. The direct simulation of Equations 6.7-6.10 with transverse aperiodic potential has been done using finite difference method. Figures 6.6(c) is plotted for weak nonlocality, in which the input power get trapped in the gain channel for high

input power. However the power switches from channel with gain to lossy channel for strong nonlocality even for high input power as depicted in Figure 6.6(d).

6.3.3 Varying the strength of the transverse potential

Figures 6.7(a) and 6.7(b) show that the power switches from gain channel to loss by tuning V_r even for low values of σ and high input power. The direct simulation of the system has been done and the results are plotted in Figures 6.7(c)-6.7(d). The direct simulation results are in agreement with the variational results. But the strength of the aperiodic potential can not induce switching.

6.4 Conclusion

The beam dynamics has been investigated in $\mathcal{PT}$ symmetric coupler with a transverse periodic and aperiodic potential having a defocusing nonlocal nonlinearity. We found that the solution provides travelling soliton if initially its center lies at the minimum of the transverse potentials. When the center of the solution lies at the maximum of the periodic potential initially, the trapped soliton is obtained. The power-dependent switching of the $\mathcal{PT}$ symmetric nonlocal coupler has been studied. The critical power increases with the range of the nonlocality and the strength of the transverse potential. The switching from gain channel to loss channel is possible for high input power by varying either the range of the nonlocality or the strength of the transverse periodic potential.

Bibliography

[1] David A. B. Miller. Are optical transistors the logical next step? Nature Photonics. 2010;4 35.

[2] M.F.Yanik and S.Fan and M.Soljai and J.D.Joannopoulos. All-optical transistor action with bistable switching in a photonic crystal cross-waveguide geometry. Optics Letters. 2003;28:24 2506-2508.

[3] F.Diebel and D.Leykam and M.Boguslawski and P.Rose and C.Denz and A.S.Desyatnikov. All-optical switching in optically induced nonlinear waveguide couplers. Applied Physics Letters 2014; 104:261111.

[4] D.G.Correia and K.M.V.Vila and D.N.Cavalcante and P.V.F.Pinto and F.T.C.B.Magalhes and L.P.de Moura and A.C.Ferreira and J.W.M.Menezes and G.F.Guimares. Non-linear switching based on dual-core nonlinear optical fiber couplers with XPM and Raman intrapulse applied to femtosecond pulse propagation. Journal of Modern Optics 2016; 63:5.

[5] S.Phang and A.Vukovic and H.Susanto and T.M.Benson and P.Sewell. Ultrafast optical switching using parity-time symmetric Bragg gratings. J. Opt. Soc. Am. B 2013; 30:11.

[6] S.Ding and G.P.Wang. All-optical transistors and logic gates using a parity-time-symmetric Y-junction: Design and simulation. Journal of Applied Physics. 2015;118:123104.

[7] A.Lupu and V.V.Konotop and H.Benisty. Optimal PT-symmetric switch features exceptional point. Scientific Reports. Oct 2017;7 1-8.

SUNEERA T. P. “STUDIES ON BEAM DYNAMICS IN SINGLE AND COUPLED PARITY-TIME SYMMETRIC SYSTEMS WITH KERR AND NONLOCAL NONLINEARITY”. THESIS. DEPARTMENT OF PHYSICS, UNIVERSITY OF CALICUT, 2018.

Chapter 7

Results and conclusions

$\mathcal{PT}$ symmetric systems shed light on reducing the detrimental effect of losses by proper engineering of materials. Artificial materials or structures can be fabricated by simultaneously controlling the gain and loss of the system, which is possible by designing both the real and imaginary parts of the refractive index profile. The study of beam dynamics in $\mathcal{PT}$ symmetric nonlinear systems are fascinating because of its far-reaching applications in nonlinear optics, photonic devices, and Bose-Einstein condensates.

7.1 Results

Our study has led to the following results and conclusions.

- We have studied fundamental and higher eigenmode solitons in a parabolic $\mathcal{PT}$ symmetric potential with Kerr nonlinearity. The $\mathcal{PT}$ symmetric phase transition point vary with the strength of real part of the potential and the coefficient of nonlinearity. The linear stability analysis reveals that the stable solitons are formed for low values of the coefficients of imaginary part of the potential and nonlinearity. The double-hump solitons exist for propagation constants higher than that of the single-hump solitons.

- We have further explored the higher eigenmodes of gap solitons in the pe-

riodic $\mathcal{PT}$ symmetric potential with nonlocal nonlinearity. Gap solitons are self-trapped wave packets in the linear band gap of periodic potentials. Double-hump nonlocal gap solitons exist above a threshold value of energy and spread through two neighboring channels in the $\mathcal{PT}$ symmetric region. The power carried by the imaginary component of the double-hump soliton increases with the imaginary part of the complex potential. The total power is invariant with respect to the strength of the imaginary part of the potential and the range of the nonlocality. The power of the soliton increases with the propagation constant or energy. The double-hump solitons exist in the $\mathcal{PT}$ symmetric domain whereas it dies out in the broken $\mathcal{PT}$ symmetric region. The double-hump solitons are unstable and the perturbation modes vary exponentially.

- The studies have been extended to $\mathcal{PT}$ symmetric coupled systems in transverse periodic and parabolic potentials with Kerr nonlinearity for linear and nonlinear regime. The propagation-invariant solutions of the system have been studied and it was found that the high frequency solitons reside in the minimum of the periodic and aperiodic potentials. The high strength of the periodic potential causes the soliton to be more confined in the lattice whereas high depth of the parabolic potential leads to the confinement of the soliton at minimum of the potential. The linear coupler possesses real eigenvalues when the gain/loss coefficient is less than the coupling coefficient for both periodic and aperiodic potentials. The transverse periodic potential modulates the amplitude of the beam and causes the formation of bands in the unbroken regime. In the case of nonlinear coupler with transverse periodic and aperiodic potentials, the beam get trapped in the channel with gain. The linear stability analysis reveals that the high frequency soliton is stable for both periodic and aperiodic potentials.

- We have further studied the fundamental and higher eigenmodes of the $\mathcal{PT}$ symmetric nonlocal coupler having transverse periodic potential. The

propagation-invariant solutions show that the system supports both high-frequency and low-frequency modes as far as the gain/loss coefficient is less than the coupling coefficient. The high-frequency and the low-frequency modes with single-hump, double-hump and triple-hump structures are obtained. The high-frequency multi-hump modes are observed in the first band gap. The low-frequency single-hump modes lie in the semi-infinite band gap whereas low-frequency double-hump and triple-hump modes lie in the first band gap. The single-hump modes get trapped in the minimum of the potential. The double-hump modes spread through the two consecutive lattice while triple-hump modes lie across three consecutive lattices. As the range of the nonlocal nonlinearity varies, the propagation constants corresponding to different modes also change. The linear stability analysis of the high-frequency and low-frequency modes predict that both modes are stable for weak nonlocality while unstable with oscillatory instability for strong nonlocality. The propagation dynamics reveals that when the range of the nonlocality increases, the width increases and the amplitude decrease, resulting constant intensity propagation.

- We have then focused our attention on the switching dynamics of the above described $\mathcal{PT}$ symmetric coupled system.The power oscillates between the channels for low input intensity whereas the power get trapped in the gain channel for high input intensity in the case of weak nonlocality and low strength of the transverse potentials. The power-dependent switching of the $\mathcal{PT}$ symmetric nonlocal coupler has been studied. The critical power increases with the range of the nonlocality and the strength of the transverse potential. The switching from gain channel to loss channel is possible for high input power by varying either the range of the nonlocality or the strength of the transverse periodic potential.

Multi-hump solitons act as multiple guiding modes. $\mathcal{PT}$ symmetric couplers find applications in all optical switching devices. All optical switches can act as high speed switch as well as basic building blocks of photonic circuitry, which

find applications in communication systems. Mathematical equivalence of NLSE with Gross-Petavsky equation suggests that the findings found applications in Bose-Einstein condensates and atom lasers.

7.2 Future prospective

There are so many frontiers to be explored in beam propagation and interaction in nonlinear media of $\mathcal{PT}$ symmetric systems. Fundamental modes being less complex are studied extensively whereas higher eigenmodes are less explored. The studies on coupled systems have to be extended to nonlinear $\mathcal{PT}$ symmetric potentials and nonlinear coupling. There are ample opportunities to extend the studies in Kerr and nonlocal nonlinear media to other nonlinearities like competing nonlinearity and photo-refractive nonlinearity. Similar studies can be extended to dark solitons and nematicons also.